Design and Analysis of Fingernail Sensors for Measurement of Fingertip Touch Force and Finger Posture

by

Stephen A. Mascaro

B.A. Physics
Houghton College, 1995

B.S. Mechanical Engineering
Clarkson University, 1995

M.S. Mechanical Engineering
Massachusetts Institute of Technology, 1997

Submitted to the Department of Mechanical Engineering
in Partial Fulfillment of the Requirements for the Degree of
Doctor of Philosophy in Mechanical Engineering

at the
Massachusetts Institute of Technology
February 2002

Signature of Author.....
Department of Mechanical Engineering
January 11, 2002

Certified by.....
H. Harry Asada
Ford Professor of Mechanical Engineering
Thesis Supervisor

Accepted by.....
Ain A. Sonin
Chairman, Department Committee on Graduate Students

Design and Analysis of Fingernail Sensors for Measurement of Fingertip Touch Force and Finger Posture

by

Stephen A. Mascaro

Submitted to the Department of Mechanical Engineering
on January 11, 2002 in Partial Fulfillment of the
Requirements for the Degree of Doctor of Philosophy in
Mechanical Engineering

ABSTRACT

A new type of wearable sensor for detecting fingertip touch force and finger posture is presented. Unlike traditional electronic gloves, in which sensors are embedded along the finger and on the fingerpads, this new device does not constrict finger motion and allows the fingers to directly contact the environment without obstructing the human's natural haptic senses. The fingertip touch force and finger posture are detected by measuring changes in the coloration of the fingernail; hence, the sensor is mounted on the fingernail and does not interfere with bending or touching actions. Specifically, the fingernail is instrumented with miniature light emitting diodes (LEDs) and photodetectors in order to measure changes in the reflection intensity when the fingertip is pressed against a surface or when the finger is bent. The changes in intensity are then used to determine changes in the blood volume under the fingernail, a technique termed "reflectance photoplethysmography." By arranging the LEDs and photodetectors in a spatial array, the two-dimensional pattern of blood volume can be measured and used to predict the touch force and posture.

This thesis first underscores the role of the fingernail sensor as a means of indirectly detecting fingertip touch force and finger posture by measuring the internal state of the finger. Desired functionality and principles of photoplethysmography are used to create a set of design goals and guidelines for such a sensor. A working miniaturized prototype nail sensor is designed, built, tested, and analyzed. Based on fingertip anatomy and photographic evidence, mechanical and hemodynamic models are created in order to understand the mechanism of the blood volume change at multiple locations within the fingernail bed. These models are verified through experiment and simulation. Next, data-driven, mathematical models or filters are designed to comprehensively predict normal touching forces, shear touching forces, and finger bending based on readings from the sensor. A method to experimentally calibrate the filters is designed, implemented, and validated. Using these filters, the sensors are capable of predicting forces to within 0.5 N RMS error and posture angle to within 10 degrees RMS error. Performances of the filters are analyzed, compared, and used to suggest design guidelines for the next generation of sensors. Finally, applications to human-machine interface are discussed and tested, and potential impacts of this work on the fields of virtual reality and robotics are proposed.

Thesis Supervisor: H. Harry Asada
Title: Ford Professor of Mechanical Engineering

ACKNOWLEDGMENTS

I wish to thank my wife Debbie for her incredible love, companionship, support, encouragement and trust, in addition to her invaluable contributions to this thesis as a proofreader and experimental subject. I wish to thank my parents Augie and Kathy for their continuing love, support, and pride in my accomplishments.

I wish to thank Professor Harry Asada for his guidance, financial support, and faith in my abilities. Thanks to my committee members, Professor Roger Kamm, Professor Ted Selker, and Dr. Mandayam Srinivasan, for their time, their interest in my work, and their valuable suggestions. Thanks also to Dr. Lynette Jones for her interest in my work and her positive feedback.

I wish to thank all the members of the Asada Group for cheerfully serving as my experimental subjects: Samuel Au, Melissa Barbagelata, Arin Basmajian, Kyu Jin Cho, Reggie Hutchinson, Peter Liu, Devin McCombie, Binayak Roy, Phil Shaltis, Danielle Tarraf, Eric Wade, Yi Zhang, and Dr. Taketoshi Mori. Thanks also to Dr. Joe Spano, Dr. Sokwoo Rhee, and Dr. Bei Gu for blazing the trail to graduation.

I wish to thank all the members of the MIT Graduate Christian Fellowship and the Eastgate Bible Study for their friendship, support, and prayers. Special thanks to Tim Finegan for solving my computer troubles and to Mike Neely for always telling me how cool my research is. Thanks also to Jonathan Wilmot for providing me with some well-needed diversions.

Above all, I thank God my Sustainer, who has given me the faith and patience to persevere.

Philippians 3:12-14

"Not that I have already obtained all this, or have already been made perfect, but I press on to take hold of that for which Christ Jesus took hold of me. Brothers, I do not consider myself yet to have taken hold of it. But one thing I do: Forgetting what is behind and straining toward what is ahead, I press on toward the goal to win the prize for which God has called me heavenward in Christ Jesus."

Revelation 21:6-7

"He said to me: "It is done. I am the Alpha and the Omega, the Beginning and the End. To him who is thirsty I will give to drink without cost from the spring of the water of life. He who overcomes will inherit all this, and I will be his God and he will be my son."

TABLE OF CONTENTS

FIGURES

INDEX OF TERMS

General Terms

F_x	lateral shear force
F_y	longitudinal shear force
F_z	normal touch force
J_1	angle of MP (metacarpal phalangeal joint)
J_2, θ	angle of PIP (proximal interphalangeal joint)
J_3	angle of DIP (distal interphalangeal joint)
P_1, P_2, ...P_8	photodiode outputs
ϕ_x	pitch angle relative to contact surface
ϕ_y	roll angle relative to contact surface

Terms for Lumped-Parameter Hemodynamic Model (LPHM)

A	absorption
A(x), B(x)	state-space matrices for LPHM
A_{C1}, A_{C2}	(proximal, distal) capillary wall surface areas
A_V	venous wall surface area
b_{C1}, b_{C2}	(proximal, distal) capillary wall damping
B_{ij}	components of input matrix B(x)
b_V	venous wall damping
C	concentration
D_{C1}, D_{C2}	(proximal, distal) nominal capillary diameters
D_V	nominal venous diameter
I_{in}	input light intensity
I_{out}	output light intensity
k_{C1}, k_{C2}	(proximal, distal) capillary wall stiffnesses
k_V	venous wall stiffness
L	path length
L_{C1}, L_{C2}	(proximal, distal) capillary lengths
L_V	length of veins in distal fingertip
m_{C1}, m_{C2}	(proximal, distal) capillary wall and blood inertia
m_V	venous wall and blood inertia
N_{C1}, N_{C2}	(proximal, distal) numbers of capillaries in nail bed
N_V	number of small veins in fingertip
P_{C1}, P_{C2}	(proximal, distal) capillary blood pressures (gage)
P_{F1}	external pressure at proximal palmar surface of fingertip
P_{F2}	external pressure at distal palmar surface of fingertip
P_H	upstream blood pressure (gage)
P_L	downstream blood pressure (gage)
P_V	venous blood pressure (gage)
R_{A1}, R_{A2}	(proximal, distal) lumped capillary fluidic resistances (on the arterial side)
R_{ij}	effective dynamic resistances
R_{Total}	total fluidic resistance in distal fingertip
R_V	lumped venous fluidic resistance
R_{V1}, R_{V2}	lumped venule fluidic resistances
u	inputs for LPHM
V_0, V_{0i}	photodiode bias/offset parameters
V_1, V_{1i}	photodiode scaling parameters
V_{Blood}	volume of blood in nail bed

V_{P1}, V_{P2}	(proximal, distal) photodiode outputs
V_{Tissue}	volume of tissue in nail bed
$\mathbf{x}$	state variables for LPHM
x_{C1}, x_{C2}	(proximal, distal) capillary wall displacements (effective changes in diameters)
x_V	venous wall displacement (effective change in diameter)
α	compound parameter in optical model
ε, $\varepsilon(\lambda)$	absorption coefficient
λ	wavelength
μ_{Blood}	blood viscosity
τ_1, τ_2	(proximal, distal) time constants for dynamic response of sensor

Terms for Predictor

a	constant
$\mathbf{b}_F$	3x1 vector of biases for neural network hidden layer
$\mathbf{b}_H$	Nx1 vector of biases for neural network output layer
f	percent rate of change of force
f_c	circling frequency
f_s	spiraling frequency
$\mathbf{F}$	3x1 vector of touch force predictions
$\mathbf{F}_0$	3x1 vector of force offsets
F_{min}	normal force threshold
F_r	shear force (radial component of total force, relative to z-axis)
F_z^{max}	maximum normal force
$\mathbf{J}_F$	3x8 force Jacobian
$\mathbf{J}_\theta$	1x8 bending angle Jacobian
n	number of data samples
N	number of hidden nodes
$\mathbf{P}$	8x1 vector of photodetector outputs
$\mathbf{P}_Q$	44x1 vector of photodetector outputs with quadratic terms
t	time
T	total calibration time
$\mathbf{Y}$	generic regression model output
$\mathbf{Y}_F$	output of touch force model
$\mathbf{Y}_\theta$	output of bending model
$\mathbf{W}_H$	3xN weight matrix for outputs of neural network hidden layer
$\mathbf{W}_P$	Nx8 weight matrix for outputs of neural network input layer
$\mathbf{Z}$	generic regression model input
$\mathbf{Z}_P$	regression input: n samples (columns) of $\mathbf{P}$ or $\mathbf{P}_Q$
β	generic least squares solution
ε	residual error
ε_F	touch force residual
ε_θ	bending residual
θ	bending angle prediction
θ_0	bending angle offset
θ_{Touch}	constant bending angle assumed when touching occurs
μ	coefficient of friction
τ_{max}	time constant of dominant mode

1. INTRODUCTION

1.1. Utility of Finger Force and Posture Measurement

There is an increasing need for measuring both finger posture and forces acting between human hands and the environment. Finger posture, which is usually measured by wearing electronic gloves, is increasingly used in the robotics and virtual reality communities for a variety of human-machine interactions (Sturman and Zeltzer, 1994). Applications include the pursuit of natural interfaces, interactions with virtual environments (Buss and Hashimoto, 1994), systems for understanding signed languages (Kramer and Leifer, 1989; Fels and Hinton, 1995), teleoperation and robotic control (Hong and Tan, 1989; Pao and Speeter, 1989), robotic teaching (Kang and Ikeuchi, 1994; Tung and Kak, 1995), computer-based puppetry, and musical performance.

Forces acting at the fingertip are usually measured by placing force-sensing pads at the fingertips. These pads have often been placed in electronic gloves in order to monitor human behavior during manipulation. Fingertip forces are critically important for understanding human manipulation and grasping (McCarragher, 1994; Sato, et al., 1996; Nakazawa, et al., 1996; Shimizu, et al., 1996; Peine and Howe, 1997). They are also useful for acquiring skills to train robots (Kim and Inooka, 1994), monitoring human behavior (Castro and Cliquet, 1997), and understanding human intentions for teleoperation of robots and human-machine interaction (Yun, et al., 1997; Mascaro and Asada, 1998; Nagata, et al., 1998). In addition to normal touching forces, shear forces, or sliding forces in the plane of the contacting surface, play an important role in human sensing and manipulation of objects (Han, et al., 1996; Howe and Cutkosky, 1989; Zee, et al., 1997). Several researchers have investigated the force response of the human fingerpad (Pawluk and Howe, 1999; Serina, et al., 1997; Gulati and Srinivasan, 1995). In addition to a better understanding of human manipulation and grasping, resulting analyses lead to better characterizations of the human haptic sense, ergonomic design criteria (Rempel, et al., 1994), and performance criteria for haptic feedback devices (Singh and Fearing, 1998).

1.2. Traditional Methods of Finger Force and Posture Measurement

Electronic glove devices were first introduced beginning in the late 1970's and have slowly developed into a useful and reliable means for measuring finger joint positions for a wide variety of applications. Sturman and Zeltzer (1994) give a comprehensive survey of glove technology from its conception to the most recent state-of-the-art developments. Kalawsky (1993) provides a more technical description of various glove devices and explains the physical principles behind the different types of sensors used in each glove.

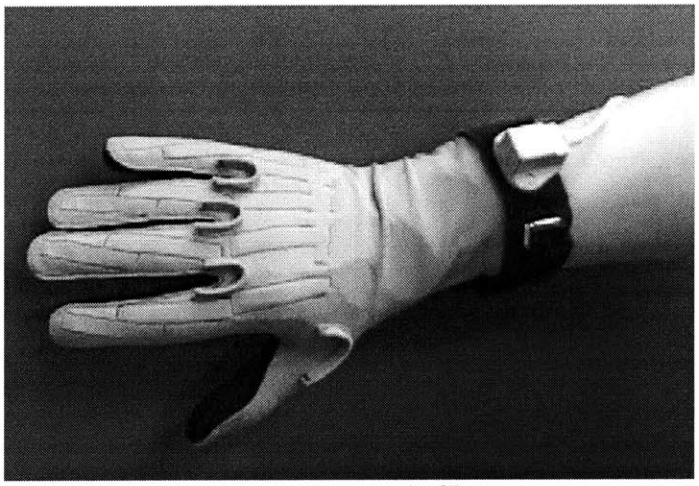

Figure 1: Electronic Glove
The glove shown here is a CyberGlove from Immersion Corporation (formerly Virtual Technologies).

One of the earliest electronic gloves was developed by DeFanti and Sandin (1977) and determined finger bend by measuring light attenuation through flexible tubes along the fingers. The MIT LED glove was developed a few years later and used cameras to track motion of LEDs embedded all over the glove (Ginsberg and Maxwell, 1983). The popular DataGlove was developed by Zimmerman (1987) and measures light attenuation through optical fibers along the fingers. The Exos Dexterous HandMaster (DHM) is an exoskeleton device worn on the fingers and hand, which uses Hall-effect sensors to measure the bending of the three joints of each finger as well as abduction of the fingers and thumb. The CyberGlove developed by Kramer (1989) and shown in Figure 1 uses thin foil strain gauges sown into the cloth to sense finger and wrist bending and abduction with up to 22 degrees of freedom. The DataGlove, DHM, and CyberGlove can all be fitted with a magnetic tracker from Polhemus or Ascension Technologies to measure 3-D position and orientation of the hand or wrist. The trackers are accurate to 0.1 inch/0.1 degrees but are distorted in the presence of ferrous metals. Optical and acoustic trackers

have also been used to provide 3-D position and orientation, however they suffer from line-of-sight limitations.

Electronic gloves are often augmented in order to measure touch forces in addition to posture. This is traditionally accomplished by embedding force-sensing pads at the fingertips (Shimizu, et al., 1996; Mascaro and Asada, 1998; Castro and Cliquet, 1997). A wide variety of such pads have been developed in the past for applications in robotics and medicine (Webster, 1988), using resistive, capacitive, piezoelectric, or optical elements to detect normal touch force. Shear forces, however, are very difficult to measure by placing sensors on the finger; thus such sensors have yet to be incorporated into electronic gloves. For robotic hands, several clever designs of shear force sensors have been presented. Howe and Cutkosky (1993) developed a superior shear force tactile sensor for detecting slip and surface texture. Novak (1989) proposed a shear force sensor design using a capacitive sensor array. Unfortunately these shear force sensors are bulky and must be placed between the fingertip and the environment in a manner that blocks the human sense of touch, and are thus unsuitable for measuring human finger forces.

A critical problem with traditional electronic gloves and force sensors in general is that they cover the fingers, blocking the natural human touch or haptic sense as well as restricting the natural bending motion of the fingers. Recently, much research has focused on reducing this problem by inventing thinner and more flexible force sensing pads (Beebe, et al., 1998; Jensen, et al., 1991; Liu, et al., 1998). However, as long as some thickness of material is placed between the finger and the environment surface, the human's haptic sense will inevitably be limited. Finger posture can be measured without restricting motion of the fingers by using video-tracking techniques; however this method of measurement is inherently limited by line-of-sight and computational requirements.

1.3. Proposal and Overview

In this thesis, a new approach to the detection of both fingertip forces and finger posture is be developed that completely eliminates any impediment to the natural haptic sense or finger motion. Namely, the forces and posture are be measured without having to cover the finger with a glove or place any sensor pad between the finger skin and the environment surface. Instead, the forces and posture are detected by measuring the response of the internal state of the finger to

force and bending stimuli. This provides the freedom to use non-collocated sensors, which are placed not on the finger surfaces where the touch forces occur or the posture is manifested, but rather on non-interfering locations such as the fingernail surface. One way to do this is to measure the coloration, or pattern of blood volume, beneath the fingernail, which changes in response to touch forces and finger bending. Miniaturized optical components and circuitry allow the sensor to be confined to the fingernail surface and disguised as a decorative fingernail covering. This allows the human to flex the fingers and touch the environment with bare fingers and perform fine, delicate tasks using the full range of haptic sense and finger motion.

First, in Chapter 2, this thesis describes a unified methodology for indirectly measuring external fingertip forces and finger posture by measuring the internal state of the fingertip. Alternative concepts for applying this methodology are proposed and narrowed down to the choice of photo-reflective plethysmograph fingernail sensors. The basic principles and construction of the sensors are then discussed. In Chapter 3, functional goals for the sensor are specified. Prototype fingernail sensors are then designed, and an experimental platform is developed in order to test their ability to measure both forces and posture. Experimental evidence using the prototype sensors is presented to demonstrate that normal forces, shear forces, and finger posture can all be detected and distinguished from each other. In Chapter 4, the relevant anatomy and physiology of the fingertip is explored and used along with experimental photographic evidence to formulate a unified model that explains the mechanism by which the internal state of the fingertip is affected by normal forces, shear forces, and change in posture. Then, a more specific, physically-based, lumped-parameter, mechanical/hemodynamic model of the fingertip is created to explain the reddening and whitening behavior of the nail bed. The model is simulated and compared to experimental static and dynamic measurements for several human subjects. In Chapter 5, a method for calibrating the sensors to individual users is developed and tested. Black-box models are created and calibrated using experimental data from the human subjects. The models are then used to estimate normal force, shear forces, and finger posture based on sensor measurements. Performances of the models are compared and analyzed. Results of the analysis are used to suggest improvements for the design of the next generation of sensors. In Chapter 6, potential applications of the sensor are discussed and tested. Finally, in Chapter 7, the contributions of this thesis are summarized and future directions for research are proposed.

2. MEASUREMENT PRINCIPLE

2.1. Direct vs. Indirect Sensing

Traditional methods of sensing finger posture and fingertip touch forces can be generally characterized by their reliance on direct measurements of the external variables of the finger. For example, electronic gloves traditionally measure the finger posture by bend sensors that directly measure the profile of the external surface of the finger. Similarly, touch forces are traditionally measured by force-sensing pads that directly measure the forces acting upon the external surface of the fingertip. In these cases, the sensors are naturally collocated with the variables of interest, as demonstrated by Figure 2. The sensor that measures external touch force is placed on the fingertip surface where this force is applied. The sensor that measures the profile of the finger is placed along the finger surface, as outlined in the figure.

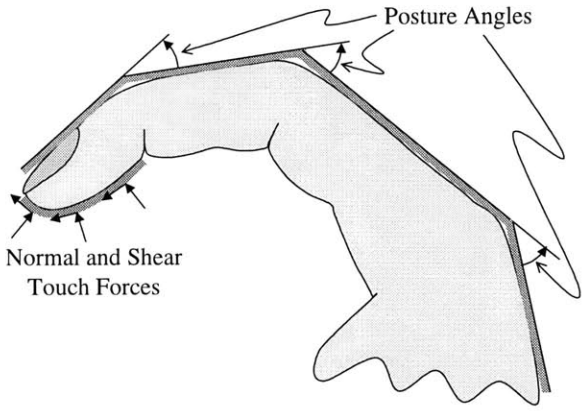

Figure 2: Finger Variables of Interest
Normal touch force, shear touch forces, and angles of the three finger joints are to be measured. Traditionally, sensors are placed along the surfaces depicted.

Although such direct sensors are an obvious solution for measuring the variables of interest, they have some inherent problems. First, the surfaces associated with the variables of interest cover a large portion of the finger as shown in Figure 2. These surfaces have sensitive nerves and covering them degrades the human's haptic sense, limiting the ability of the human to interact with the real environment. Second, these surfaces are comprised mostly of compliant skin. As a result, attaching sensors is difficult, inevitably restricts the motion of the finger, and causes discomfort.

The alternative to direct sensing is indirect sensing. In this case, the variables of interest are somehow measured by sensors that are located elsewhere from the surfaces where they occur. The indirect sensor would not need to be worn over the sensitive area of the fingertip or all along the finger profile. Thus it would have the advantage of preserving the human's natural haptic sense and the natural ease and comfort of finger motion. Therefore, the drawbacks of direct sensing could be overcome.

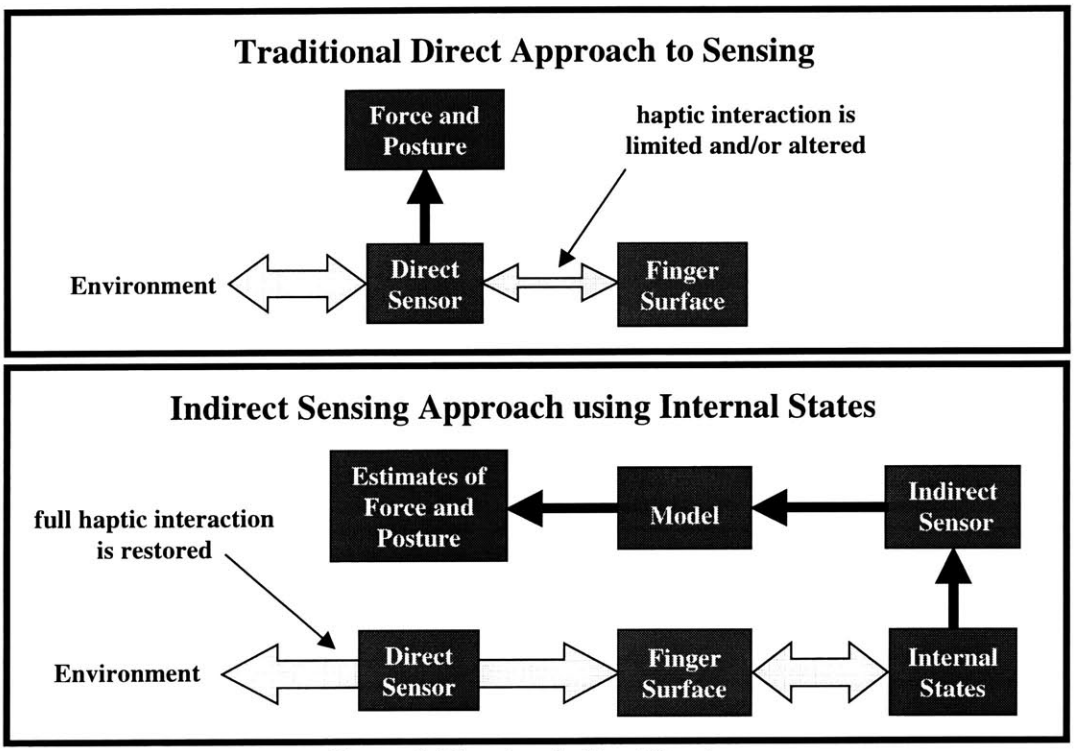

Figure 3: Direct vs. Indirect Sensing
Direct sensors interfere with the finger surfaces where the variables of interest are measured. Indirect sensors avoid interference by remotely measuring the internal states of the finger and using a model to predict the variables of interest.

In order for indirect sensing to work, the variables of interest must first be related to some internal states of the finger. Secondly, the non-collocated sensors must be capable of either measuring these internal states directly, or measuring some other external variables that are connected to the same internal states. Figure 3 demonstrates the difference between collocated and non-collocated sensors. The collocated sensors interact bi-directionally with the variables of interest and affect how those variables respond to environmental stimuli such as externally applied forces. The non-collocated sensors can be designed and placed so as to measure the internal states without affecting their dynamics or their response to environmental stimuli.

2.2. Alternatives for Indirect Sensing

The first step in designing non-collocated sensors for measurement of finger posture and fingertip force is to investigate how the internal states of the finger are affected by changes in posture and externally applied forces. When a force is applied to the fingertip, there are several relevant changes that take place within the finger. First, the mechanical strains and stresses within the fingertip tissue are affected. Second, the tension in the finger tendons changes in order to balance the external force, requiring a change in the myoelectric signals that control the muscles in the forearm which pull on the tendons. Third, the blood flow or hemodynamics of the finger is affected. Fourth, the nerve receptors in the pulp of the fingertip and the tendons are affected. All of these internal states are affected by changes in finger posture as well.

Internal State	Method of Measurement	Location of Measurement
Stress and Strain in Tissue	Strain Gage	Skin or Fingernail Surface
Tension in Finger Tendons	Myoelectric Sensors	Muscles in Forearm
Blood Volume	Plethysmograph: electrical or optical	Skin or Fingernail Surface
Nerve Response	???	

Figure 4: Sensing Alternatives
Four methods of indirect measurement are identified. The method of choice is blood volume measurement using photoplethysmograph on the fingernail.

The next step is to address how these internal states can be measured, and the feasibility thereof. Figure 4 summarizes the following possibilities:

1. **Stress/strain** within the fingertip can be measured by attaching strain gages to the surface of the finger and perhaps the fingernail as well. To date, no known efforts have been undertaken to perform such measurement.

2. Although **tendon tension** cannot be directly measured in a non-invasive manner, the myoelectric signals can be measured by affixing electrodes to the skin near the muscles in the hand and forearm. Even so, the muscles are stacked on top of each other, making it difficult to get reliable non-invasive measurements of specific muscle activity (Long, 1981).

Furthermore, the tendons from different muscles are interconnected, making it difficult to relate the forces in the muscles to the forces in the fingertip.

3. The **blood volume** in the finger can be measured either optically, by shining light through the finger, or electrically, by measuring the impedance across the finger. Both are established techniques for measuring the pulse rate, but have not until now been tried for detecting finger forces and posture.

4. There is currently no practical method for measuring the **nervous response**. The hand is richly innervated with 17,000 tactile units supplying the glabrous (hairless) skin of the hand and consisting of four principle types of mechanoreceptors, each having a different haptic response and functionality (Vallbo and Johansson, 1984). Furthermore, the receptors are all connected to the central nervous systems via a complex network of sensory paths (Rabischong, 1981). Recently, brain signals of primates relating to tactile sense and arm motion have been measured (Nicolelis, et al., 1998; Wessberg, et al., 2000), but such methods are invasive and are not appropriate for human subjects.

Although strain gages, myeolectric sensors, and optical and electrical "plethysmographs" (blood volume sensors) may all be viable approaches, it is beyond the scope of this project to study more than one. For reasons of novelty and a few key advantages, this thesis focuses on using optical blood volume or "photoplethysmograph" sensors for measurement of fingertip touch forces and finger posture. These sensors are particularly advantageous because they can be placed on the human fingernail. The rigidity and insensitivity of the fingernail make it an ideal surface for attachment of a sensor, while the transparency of the fingernail and the anatomy beneath it make it a unique window into the hemodynamics of the finger. Changes in blood volume beneath the fingernail are easily visible to the naked eye as changes in the color pattern of the fingernail.

2.3. Fingernail Color Changes

As the human fingertip is pressed down on a surface with increasing force, the blood flow through the fingertip is affected, and a sequence of color changes is observed through the

fingernail. In fact, the color change is characteristically non-uniform across the nail, resulting in distinct patterns of color change for different types of forces.

a) Normal Touch Force

Figure 5 shows the typical sequence of noticeable color changes with increasing normal force. As the touch force is first increased, the veins in the fingertip are collapsed, causing blood to pool up in the capillaries beneath the nail, resulting in the reddening effect. As the force continues to increase, the force propagates around the bone, collapsing the capillaries at the tip of the nail bed, resulting in a white zone at the tip of the nail. A variety of descriptions of the anatomy and physiology of the fingertip can be found in medical literature. In Chapter 4, the mechanism of these color changes is discussed in more detail and anatomically based models are created in order to explain the underlying changes in blood volume.

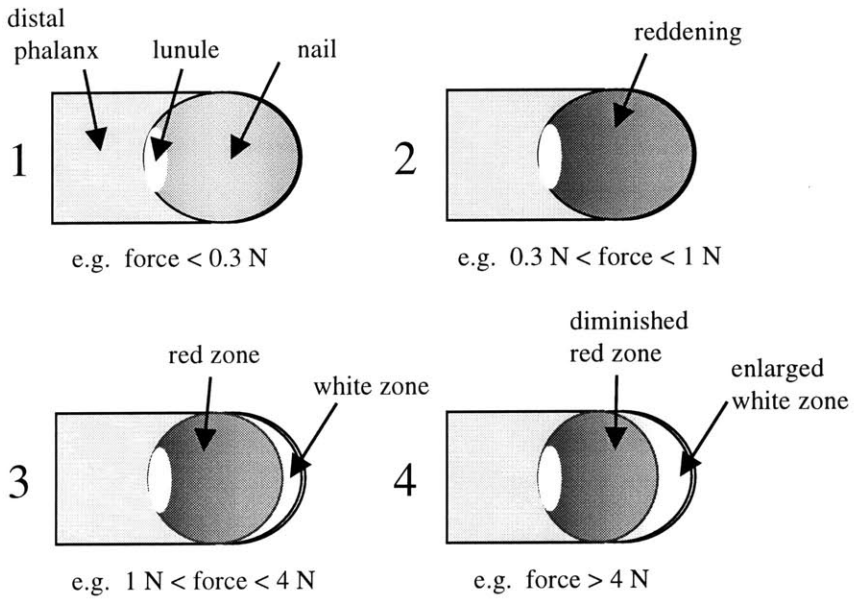

Figure 5: Fingernail Colors Due to Touching
The figure depicts a typical sequence of fingernail color changes when the fingerpad is pressed straight down against a flat surface. Red zone indicates increased blood volume while white zone indicates decreased blood volume.

b) Change in Posture

Normal touch force is not the only action that results in a change in fingernail color. Alterations in finger posture as well as application of shear force result in different color patterns than those shown in Figure 5.

When the posture of the finger is altered, i.e. the joints of the finger are bent or extended, the color of the finger changes as shown in Figure 6. When the finger is extended, a tension is set up in the tissues of the nail bed that collapses the capillaries. When the finger is bent, that tension is relieved and the capillaries fill with blood again. Creasing of the veins during bending may also contribute to blood pooling up in the capillaries. The color changes shown in Figure 6 are concentrated near the center of the nail, whereas the color changes due to normal touching occur particularly towards the tip of the nail. Therefore it should be possible to distinguish between a touching action and a change in finger posture based on observable changes in fingernail color patterns.

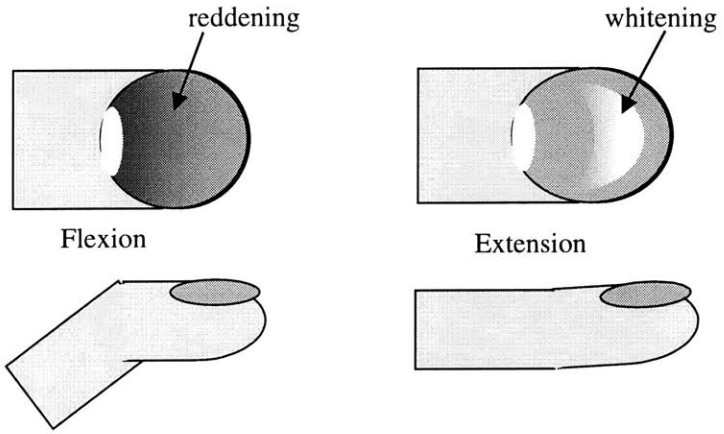

Figure 6: Fingernail Colors Due to Bending
Fingernail color patterns for flexion and extension of the finger are different than those for touching.

c) Shear Force

When shear forces are applied to the palmar surface of the fingertip, yet another set of color patterns result, as shown in Figure 7. If the shear force is applied longitudinally, a tension in the tissues of the nail bed is set up, resulting in either a broad whitening effect over the center of the nail or a white band at the tip of the nail, depending on the direction. If the shear force is applied laterally, tension in the nail bed creates whitening zones that are asymmetrical.

Since the patterns for lateral shear force are distinctly asymmetrical, it should be easy to distinguish from normal touching and bending. Longitudinal shear forces may present a greater challenge to distinguish. When the longitudinal shear is applied inward (top right of figure), the whitening zone is similar to that of bending, but extends all the way to the lateral edges of the nail. When the longitudinal shear force is applied outward (top left of figure), the whitening zone

is almost indistinguishable from that of normal touching, making this perhaps the most challenging force to measure. However, there may be subtle variations in reddening or whitening that are more visible to optoelectronic sensors than to the naked eye.

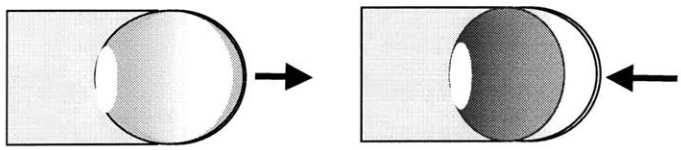

Longitudinal shear forces

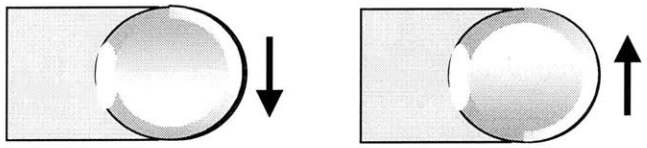

Lateral shear forces

Figure 7: Fingernail Colors Due to Shear

When the finger exerts shear forces against a flat surface by sliding the finger in the directions of the arrows, a variety of red and white zones emerge.

2.4. Measurement of Blood Volume by Photoplethysmography

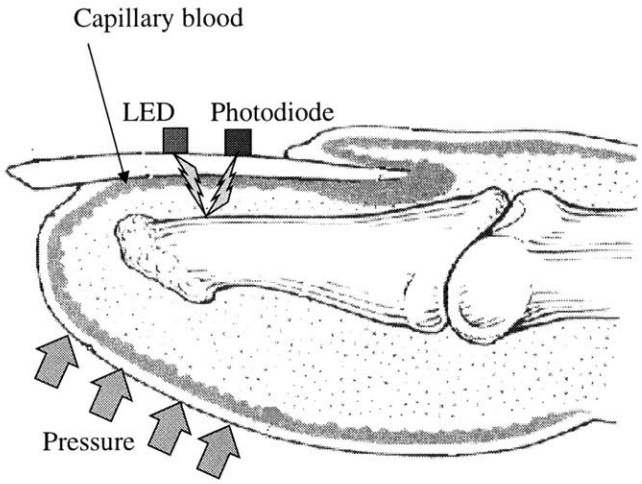

Figure 8: Sensing Principle

LED and Photodiode can be used to measure the capillary blood volume underneath the fingernail, which changes with applied pressure. Figure is adapted from Spence (1982) with permission.

The color patterns described above are directly related to the blood volume in the bed of tissue underneath the fingernail. The amount of blood in the fingernail bed can be monitored by shining light into the fingernail and measuring the intensity of reflected light, a technique termed "reflectance photoplethysmography." In the past, skin reflectance photoplethysmography has been performed to measure both blood volume (Higgins and Fronek, 1985) and oxygenation

(Mendelson and Ochs, 1988) by placing a light source and photodetector on the skin. In order to measure blood volume under the nail, arrays of light emitting diodes and photodetectors can be placed on the nail as shown in Figure 8.

Figure 9 shows a basic construction of the photoplethysmograph circuitry. An LED illuminates the nail bed with light, while a photodiode is mounted nearby and detects the reflected light from the nail bed. When the volume of blood under the fingernail increases, more light is absorbed, less light is reflected, and the output voltage of the photodiode circuit, $|V_{out}|$, decreases.

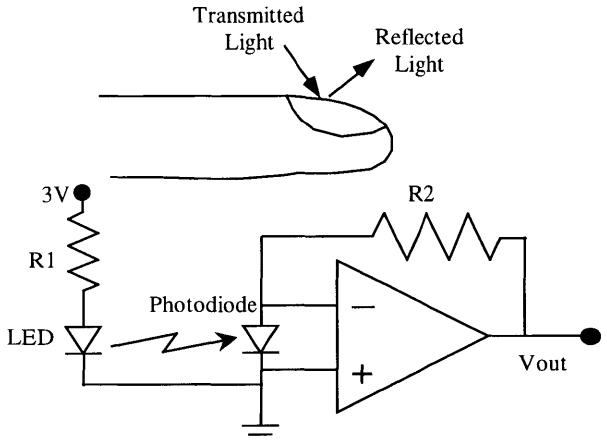

Figure 9: Photoplethysmograph Circuitry
The output voltage of the circuit, V_{out}, is proportional to the amount of light reflected from the fingernail.

For pulse oximetry applications, high pass filtering is used to remove the DC component of V_{out}, which is due to non-pulsatile arterial blood absorption, venous and capillary blood absorption, and tissue absorption (Welch, et al., 1990). However, for the fingernail sensor, it is precisely the "DC" component, which actually varies with touch pressure and posture, that is of interest. The impact of this on sensor design is be further addressed in the following chapter.

3. EXPERIMENTAL DESIGN AND IMPLEMENTATION

3.1. Design Goals

The goal of this chapter is to develop and implement a prototype design for a fingernail sensor and an experimental apparatus that can be used to investigate the response of the sensor to fingertip touch forces and changes in finger posture. Before this can take place however, it is important to define more specifically the functional requirements of the sensor. First, the variables of interest that are to be measured must be identified. Secondly, the extraneous variables whose effect must be suppressed need to be identified.

3.1.1. Variables of Interest

Figure 10 defines the variables of interest that could potentially be measured using the fingernail sensors. Assuming the contact surface is flat, an x-y-z coordinate system is defined relative to the surface as shown, where the z-axis is normal to the surface and the y-axis is aligned in the plane of bending of the finger. The variables of interest include the x-y-z components of touch force, the three joint angles of the finger, and the roll and pitch angles of the fingertip relative to the contact surface. If the contact surface is not assumed to be flat, then a countless number of additional variables of interest could be defined to describe the state of the fingertip, however that is beyond the scope of this thesis.

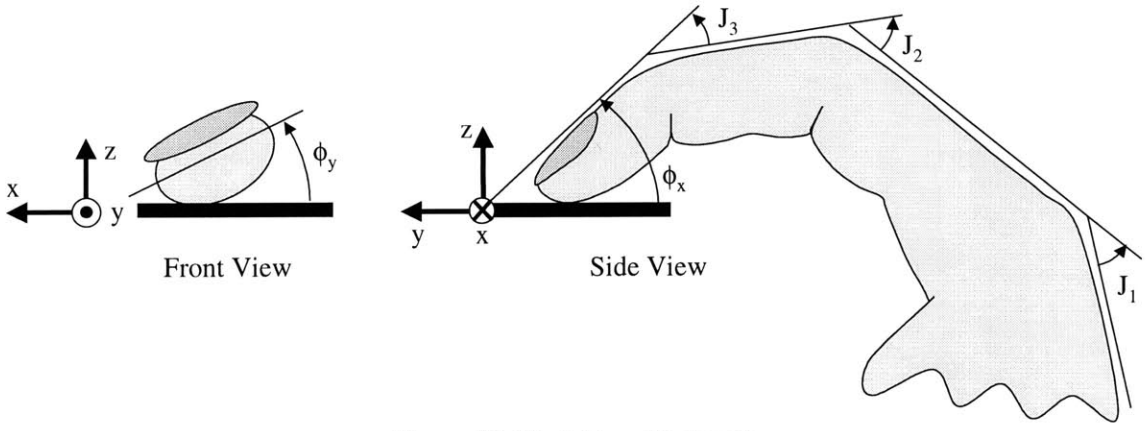

Figure 10: Variables of Interest
The x-y-z coordinate system is defined relative to the contact surface and the plane of bending of the finger. Touch forces are positive when the finger is pushed in the positive x-y-z directions. The finger posture is represented by the angle of the knuckle (MP) joint, J_1, the middle (PIP) joint, J_2, and the distal (DIP) joint, J_3. Posture angles are positive for flexion and negative for extension.

The variables of interest can thus be summarized by the following list:

- F_x lateral shear force
- F_y longitudinal shear force
- F_z normal touch force
- J_1 angle of MP (metacarpal phalangeal or knuckle) joint
- J_2 angle of PIP (proximal interphalangeal) joint
- J_3 angle of DIP (distal interphalangeal) joint
- ϕ_x pitch angle relative to contact surface
- ϕ_y roll angle relative to contact surface

The forces, F_x, F_y, and F_z, are defined here and for the rest of this thesis as the forces applied by the finger to the surface. Thus the sign convention for the forces is such that the forces are positive when the finger is pushed against or along a surface in the positive coordinate directions. By this convention, pushing the finger down against a surface results in negative F_z. Sliding the finger along a surface in the positive x and y directions results in positive shear forces, F_x and F_y. The reaction forces applied by the surface to the finger, which are equal but opposite, are be positive when pointing in the negative coordinate directions. The bending angles are defined to be positive for flexion and negative for extension.

Application	**Discrete Variables** (On/off detection)	**Continuous Variables** (Range of Values)
Virtual Switch	F_z	(F_z optional)
Wearable Mouse	F_z	F_x and F_y (J_1, J_2, or J_3 optional)
Skill Monitoring		F_x, F_y, F_z, J_1, J_2, J_3 (ϕ_x and ϕ_y optional)

Figure 11: Application Requirements
Desired subsets of the variables of interest are defined based on sensor applications described in Chapter 6.

Chapter 6 contains a detailed description of several potential applications that could be achieved by measuring these variables with the fingernail sensor. The three main applications are the virtual switch, the wearable mouse, and skill monitoring. Figure 11 lists the variables that are required/desired to be measured for each of these applications. As a bare minimum, the sensor should be capable of detecting F_z in an on/off fashion. Ideally, the fingernail sensor would be capable of simultaneously measuring a range of values for all of eight of these variables. This would require at least eight photodetectors arranged in a two dimensional array across the fingernail to capture both lateral and longitudinal color patterns. Even so, the prospect of achieving this ideal is likely to be very difficult. A suitable goal for this thesis is to achieve at least the functionality required to implement the wearable mouse application. This requires measurement of F_x, F_y, and F_z, and possibly one joint angle. If not measured, any changes due to the joint angles must at least be rejected as disturbances. Furthermore, if the contact angles are not to be measured, they too must be kept constant or their effects must be rejected.

3.1.2. Eliminating Extraneous Variables

Before the sensor is designed, the issue of eliminating extraneous variables must be addressed. An extraneous variable is defined here as any variable other than touch force or finger posture that influences sensor output. The following is a list of those that are known:

- Oxygen saturation
- LED intensity
- Ambient lighting
- Sensor position
- Hand elevation
- Temperature
- Cardiovascular status

The fingernail sensor should be designed such that the influence of these variables on sensor output should be eliminated and/or held constant to whatever extent possible.

a) Oxygen Saturation

The oxygen saturation of the blood is an extraneous variable because in general, the light absorption coefficient of blood depends on the oxygen content. Figure 12 shows the effect of oxygen concentration on the absorption coefficient for a range of wavelengths. The two primary components of blood are the oxyhemoglobin (HbO_2) and reduced hemoglobin (Hb). In general,

the absorption coefficients of these two components differ. For example, at a wavelength of 660nm (visible red light), the absorption coefficient of Hb is 10 times as large as HbO_2. Thus a typical drop in the oxygen concentration of 10% (Nitzan, et al., 2000) between the finger arteries and veins is sufficient to change the visible appearance of the blood from red to blue.

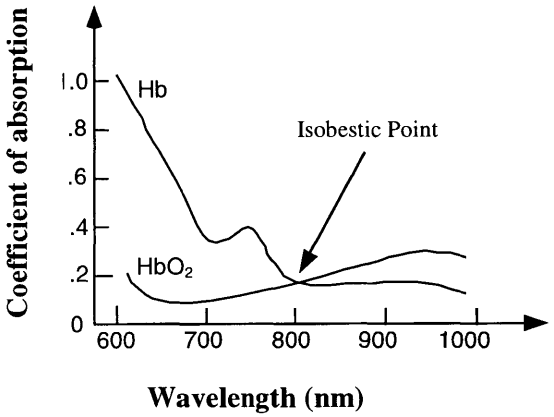

Figure 12: Effect of Oxygen Concentration
The isobestic point (~800nm) is the wavelength at which de-oxygenated and oxygenated hemoglobin have the same coefficient of absorption. This figure only shows approximate trends based on information from Tremper and Barker (1989).

In fact, by using LEDs of two wavelengths, the relative concentrations of these two components can be estimated, which is the principle behind pulse oximetry. However, for the purpose of measuring blood volume alone, it is desirable to remove the dependence of the absorption coefficient on oxygen concentration. This can be accomplished by using LEDs at the "isobestic" wavelength of 800nm, where the absorption curves of oxyhemoglobin and reduced hemoglobin intersect. At this wavelength, the absorption is independent of the relative concentration of these two components. While LEDs of 800nm can be custom-made, 770nm LEDs are more commonly available and are close to the isobestic point. Therefore LEDs of 770nm are be used for the fingernail sensor.

There are actually other isobestic wavelengths in the visible range below 600nm, however the tissue penetration depth is much smaller due to the higher absorption coefficients of melanin and proteins, which normally precludes the use of those wavelengths for photoplethysmograph applications. Likewise, at wavelengths above 900nm, the absorption coefficient of water becomes too large.

b) LED Intensity

In order to minimize any effects due to variation in LED intensity, the current through the LED should be strictly controlled, since the light intensity is directly proportional to the current. Figure 13 contains a modified version of the basic plethysmograph circuit of Figure 9. As shown in the figure, a transistor can be used to transform the input voltage (from a battery or power supply) to a proportional current through the LED.

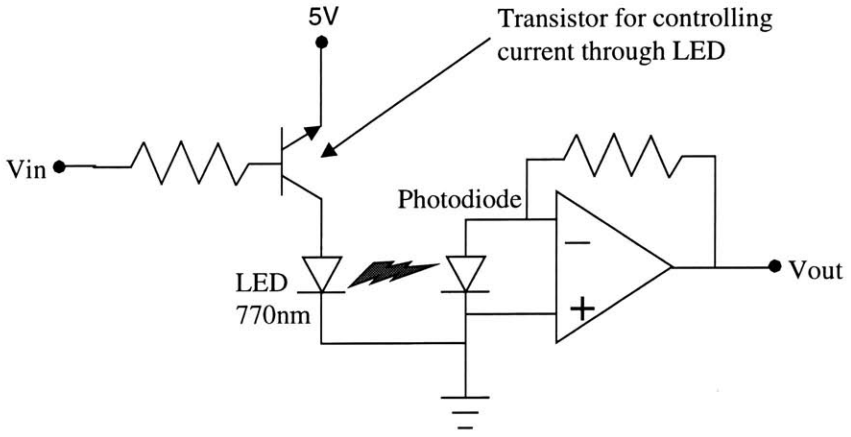

Figure 13: Nail Sensor Circuitry with Current Control
Voltage V_{in} controls the current and thus the incident light intensity, which is at the isobestic wavelength.

c) Ambient Lighting

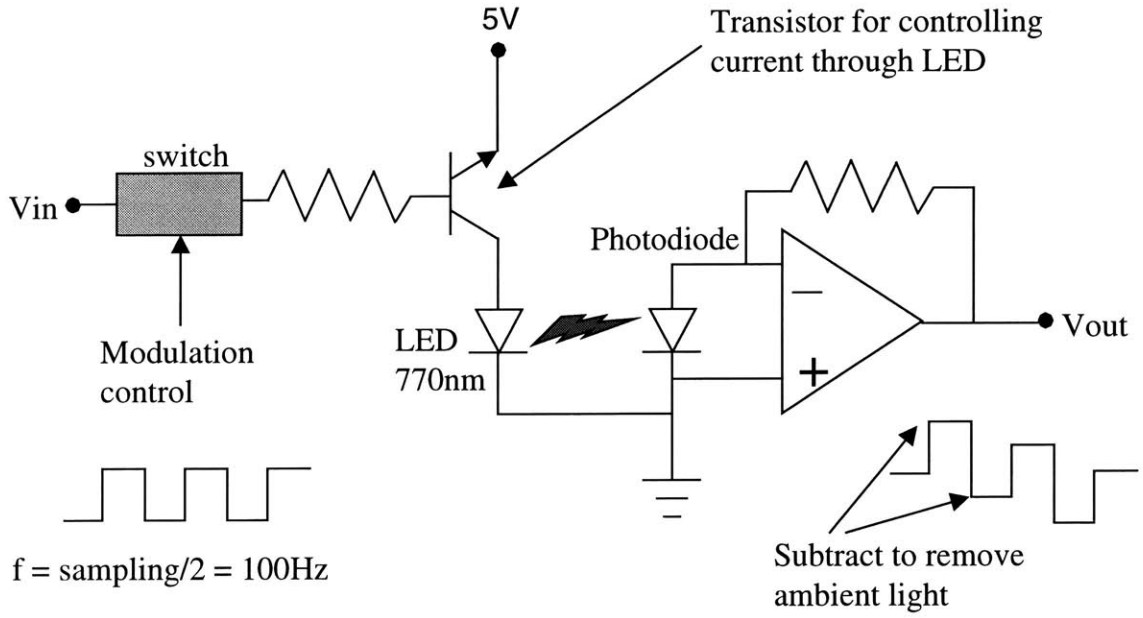

Figure 14: Nail Sensor Circuitry with Modulation
Incident light is modulated on and off in order to subtract the contribution of ambient light from V_{out}.

In order to remove the influence of ambient lighting, the sensor should be coated on top and sides with an optically opaque material. To remove the influence of any remaining ambient light (e.g. that which penetrates underneath through the skin), a modulation scheme can be used, such as shown in Figure 14. The LED is turned off and on at half the sensor sampling frequency. Thus, every other photodiode measurement is taken with the light on and then off. By subtracting two consecutive samples, the portion of the photodiode response due to ambient lighting is removed.

d) Sensor Position

Any change in the position of the sensor on the fingernail, especially a change in distance between the sensor and nail surface, will result in unwanted variation in sensor output. Therefore, the sensor must be attached as rigidly as possible to the nail surface to prevent any relative movement or rotation between the two. In order to accomplish this, the sensor should be molded to the shape of the fingernail and attached using a strong transparent adhesive. In addition, the wiring that transmits the signals from the sensor should be as thin and flexible as possible in all directions, so that movement of the hand does not cause the wiring to exert large forces or torques on the sensor.

e) Hand Elevation

The elevation of the hand relative to the heart affects the blood pressure in the hand and fingertip, thus affecting the blood volume. Unfortunately, this extraneous variable cannot be eliminated or controlled by the physical design of the sensor. Only the nature of the application can be designed with this in mind. For example, a virtual keyboard or fingertip mouse application would be good for maintaining relative elevation of the hand, while a skill monitoring application involving lots of arm movement could be problematic.

f) Temperature

The temperature of the human body is automatically regulated by controlling the amount of blood flow to the extremities, including the hand and fingers. Changes in ambient temperature and/or body temperature prompt the blood vessels in the hand and fingers to constrict or relax, altering the blood flow, and thus the blood volume. The only way to minimize the effect of this variable through sensor design is to design the sensor to operate at a low enough power level that

it does not significantly heat the fingertip. Aside from sensor design, the application can be designed such that the ambient temperatures experienced are mild and constant.

g) Cardiovascular status

Finally, a number of variables associated with the human cardiovascular status are capable of affecting the blood flow and blood volume in the fingertip. Some of these are coupled with the regulation of body temperature already mentioned. Again, all that can be done is to design the application for the sensor with this in mind—e.g. avoiding strenuous or energetic activities.

3.2. Experimental Design

3.2.1. Conceptual Design of Sensor

Up to this point, the basic plethysmograph circuitry of the sensor has been determined, as shown in Figure 14, and functional design criteria for the overall sensor have been specified and discussed. In designing a prototype of the fingernail sensor, there are a few critical issues to be addressed.

a) Size and profile

The sensors should be thin and unobtrusive. Using miniaturized optical components and circuitry, they could be disguised as a decorative fingernail such as those commonly worn on the natural fingernail.

b) Means of attachment

To minimize sensor noise from motion artifact, the sensors should be attached rigidly to the fingernail. However, the interface must be optically transparent to maximize the sensitivity of the sensor.

c) Shielding of ambient light

To reduce sensor noise from ambient lighting, the photodiodes should be optically shielded from above. They should also be shielded from the side to prevent direct illumination from the LEDs, which would result in a large unwanted DC voltage.

d) Signal processing and transmission

The op amp stage shown in Figure 14 should be located close to the photodiodes so that the sensor signals are amplified before being transmitted over a long distance. However, to minimize the size and complexity of the sensor, all other signal processing can be done after transmitting the signals away from the fingernail.

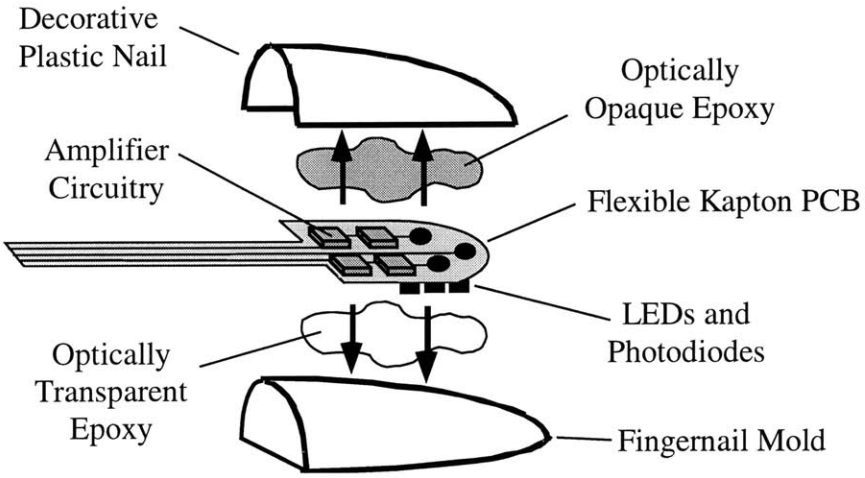

Figure 15: Nail Sensor Conceptual Design
Optical components are mounted on a flexible printed circuit board with layers of epoxy above and below for the purposes of blocking ambient light and molding to the shape of the fingernail.

Figure 15 shows a conceptual design that aims to meet the aforementioned requirements. In order to minimize size and profile, miniaturized die-form optical and electrical components are mounted using wire bonding to a thin flexible Kapton printed circuit board. The optical components (LEDs and photodiodes) are placed on the bottom and covered with a protective layer of optically transparent epoxy, which is molded to the shape of the wearer's fingernail. A barrier of optically opaque epoxy is placed between the photodetectors and LEDs to prevent direct illumination. The amplifier components are placed on top, and then the entire top surface is coated with optically opaque epoxy for shielding of ambient light, and finally a decorative plastic nail is placed on top for aesthetic purposes. After amplification, the signals travel through the thin flexible Kapton strip to the wearer's wrist, where they can be transmitted wirelessly to the computer. The sensor can be attached to the wearer's fingernail using a double-sided transparent adhesive.

3.2.2. Sensor Implementation

In realizing the conceptual design of the sensor, the experimental scope of this thesis justifies two significant deviations from the ideal conceptual design. First, the wireless transmission of the signals from the wrist is unnecessary for experimentation. Instead, a tethered cable connection at the wrist is used. Second, the flexible Kapton PCB complicates the wire-bonding process since the flexible PCB absorbs the ultrasonic energy of the bonder. Instead, the sensors will be constructed from a rigid PCB, which is thicker but suitable for experimentation. Ultra-thin single-stranded wires will be used to transmit the signals from the PCB on the nail to the tether on the wrist.

As discussed earlier, a two-dimensional array of at least eight photodetectors should be used in order to measure and distinguish between the variables of interest. A single op-amp die contains two operational amplifiers. Therefore, four op-amp chips (and eight resistors) are required for eight photodetectors. Each photodetector should have an LED nearby to measure the local blood volume. By placing LEDs between the photodiodes, less than eight LEDs are necessary. Miniature die-form photodiodes, LEDs, op-amps, and resistors are all commercially available in the following sizes:

- LEDs: 0.25 mm x 0.25 mm
- Photodiodes: 1 mm x 1 mm
- Op-Amps: 1.25 mm x 1.75 mm
- Resistors: 0.5 mm x 1 mm

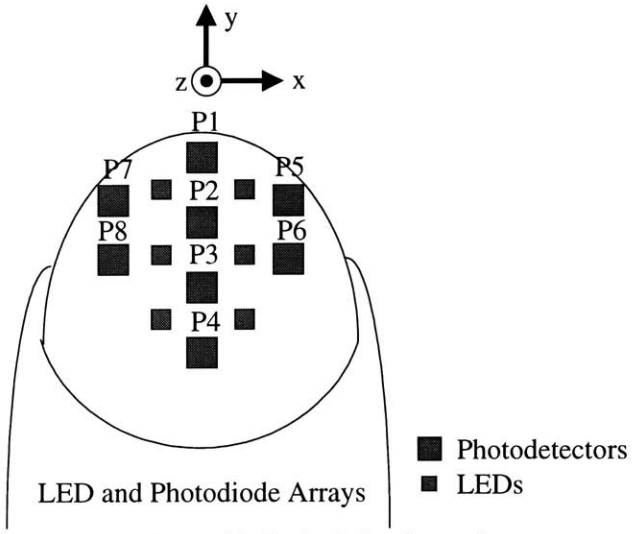

Figure 16: Optical Configuration
Two-dimensional arrays of photodetectors and LEDs are placed across the fingernail surface as shown from above.

Using these components, eight photodetectors can be arranged over the touch-sensitive part of the fingernail in a laterally symmetric configuration, as shown in Figure 16. The six LEDs placed between the photodiodes ensure that each photodiode has at least one adjacent LED. Figure 17 shows the implementation of the fingernail sensor prototype using a rigid PCB. The image on the left shows the bottom side with the array of photodiodes and LEDs. The image on the left shows the top side with the op-amp chips and a 14-pin connector for transmitting the signals to the wrist.

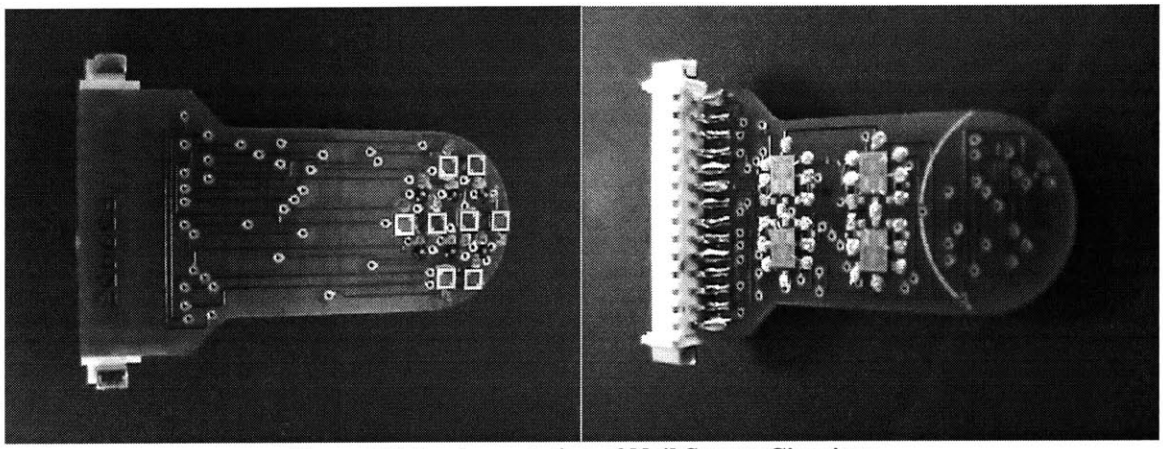

Figure 17: Implementation of Nail Sensor Circuitry
A functional sensor is assembled using a rigid PCB. In the left picture, the eight photodiode chips on the bottom side of the sensor are visible. In the right picture, the op-amp chips and connector are visible on the top side.

After the optical and electrical components are in place as shown in Figure 17, they are coated with protective epoxy and the bottom of the sensor is molded to the shape of the user's fingernail. First a wax cast is taken of the finger. The wax cast is then used to create a polyurethane rubber mold that replicates the fingernail surface. The sensor is then molded to this surface using transparent epoxy. Appendix A contains a complete description of the manufacturing process including the wire-bonding and molding processes. The completed experimental fingernail sensor is shown in Figure 18. In order to attach the sensor to the fingernail, a strong transparent adhesive is needed, preferably removable. Such an adhesive is easily available in most drug stores in the form of the double-sided transparent adhesive tabs that are commonly used to attach artificial cosmetic fingernails. These tabs come in a variety of sizes in the shape of the fingernail, are easily applied, and can be removed with a strong but not excessive force.

Figure 18: Experimental Implementation
A fully assembled sensor is mounted on the fingernail using transparent double-sided adhesive.

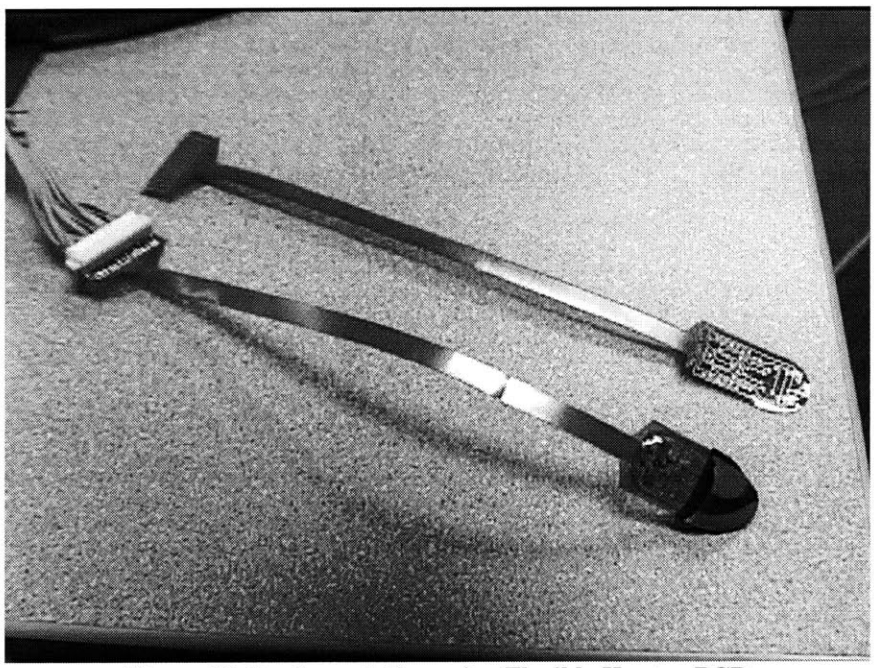

Figure 19: Implementation using Flexible Kapton PCB
Using a flexible PCB, the sensor can be made thinner and less obtrusive.

Figure 19 shows an implementation of the fingernail sensor using a flexible Kapton printed circuit board. The image shows a completed sensor beneath the bare PCB. Figure 20 depicts a "finger-free" electronic glove using multiple fingernail sensors. The magnetic tracker

mounted on the wrist measures 6-D position and orientation of the hand while the fingernail sensors measure the finger posture and forces at the fingertips.

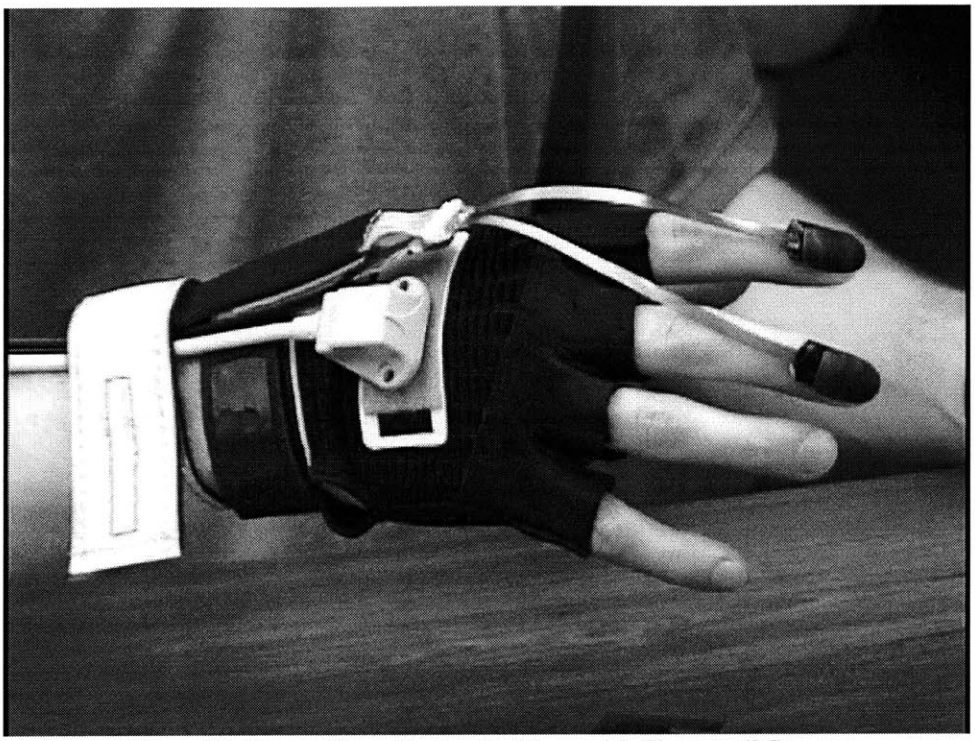

Figure 20: Finger-Free Electronic Glove with Fingernail Sensors
Multiple fingernail sensors can be combined with other sensors such as the magnetic tracker shown here to form a fingerless glove.

3.2.3. Experimental Platform

Appendix B shows a diagram of the experimental hardware used to collect data from the fingernail sensor. A triple output power supply powers the LEDs and op-amps while a multifunction data acquisition board is used to modulate the power to the LEDs and perform 16 bit A/D conversion. A Pentium III 450 MHz computer running a custom Java graphic user interface is capable of sampling all eight photodiode signals at a rate of 25 Hz.

In order to experiment with touch forces, it is necessary to be able to measure the shear forces that are applied to the finger along both the x-axis and y-axis as well as the normal touching force along the z-axis. Figure 21 shows a picture of the force measurement system that is used. A Nano17 6-axis force/torque transducer from ATI Automation is used in order to measure forces in the x, y, and z directions. The shear forces F_x and F_y have a sensing range of $\pm$ 12 N and a resolution of 0.8×10^{-3} N. F_z has a range of $\pm$ 17 N and a resolution of 1.6×10^{-3} N. A rubber pad is placed between the finger and the sensor in order to maximize the coefficient of

friction and thus decrease the dependence of the shear force on the normal force. Data from this force platform is also sampled at 25 Hz by the Java GUI.

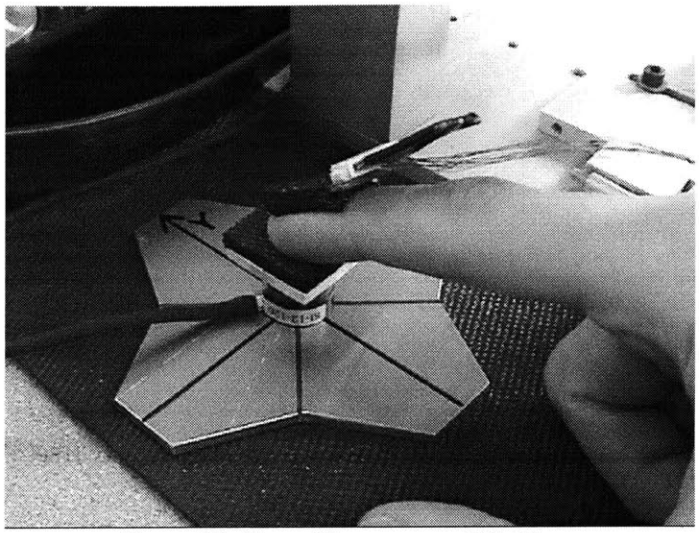

Figure 21: Force Measurement Platform
A Nano17 force/torque transducer from ATI Automation is mounted underneath to measure three axes of touch force. A rubber pad on top facilitates application of shear forces.

Ideally, the experiments would be designed so that the finger joints would be held in place while an automated apparatus applies precise normal and shear forces. Unfortunately, a device that would hold the finger in place would put pressure on the finger and affect the blood flow, thus affecting the nail color. Therefore, the human must be relied upon instead to apply the forces as precisely as possible. A visual feedback system consisting of gauges on a computer monitor is used to display to the human in real-time the forces that are applied as the finger is pressed on the platform. In addition, as long as the contact angles are not measured, the human must be relied upon to keep the contact angles constant. This is easiest if the contact angles are maintained at zero degrees by pressing the fingerpad against the platform with the bone parallel to the surface, such that the contact area is maximized and the contact is most stable.

In order to experiment with finger posture, it is necessary to be able to measure the angles of the joints of the finger while measurements are simultaneously taken from the fingernail sensor. The easiest method would be to wear an electronic glove; unfortunately such gloves constrict the fingers and interfere with the adhesion of the sensor to the nail. Therefore the fingers are left free and a video tracking system is used instead, as shown in Figure 22. A pair of colored markers is placed on each joint of the finger and video is taken continuously during the

experiment. An image-processing algorithm is then used off-line to track the centroids of the markers and compute the angle of each joint for each time index. The clock on the computer monitor is used to synchronize the time index of the joint angle measurements to that of the photodetector measurements.

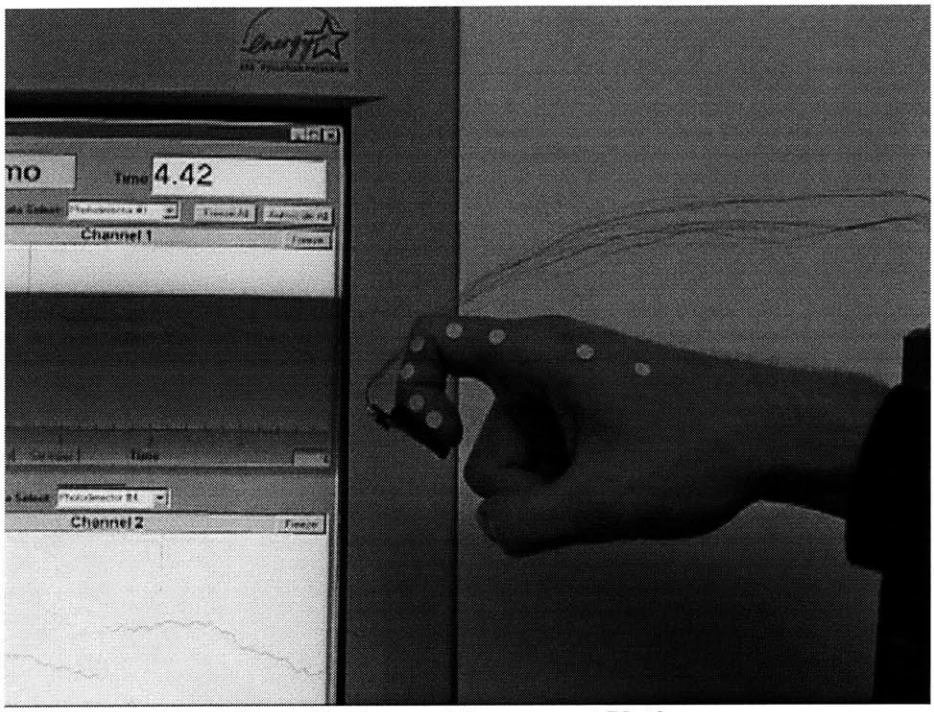

Figure 22: Posture Measurement Platform
Colored markers on the finger joints are used for offline tracking of the finger posture. The time index on the screen is used for synchronization of the data.

3.3. Preliminary Experiments

3.3.1. Purpose

In this section, preliminary experiments are performed in order to investigate the response of the prototype sensor for different types of forces and changes in posture. The purpose of these preliminary experiments can be summarized as the following:

1. To check whether the sensor responses are consistent with observable color changes
2. To gauge how distinguishable the responses to different forces/posture are
3. To identify the range of sensitivity in terms of force and posture

These items will serve as a platform for explaining the physical mechanism of the color changes in Chapter 4 and for designing calibration experiments for a force/posture estimator in Chapter 5.

3.3.2. Normal Force

For the first experiment, a human subject is instructed to apply only normal force to the fingerpad in order to investigate the sensor response. The subject is also instructed to maintain the joint angles of the finger and the contact angles at the surface all equal to zero degrees by extending the finger straight out (parallel to the platform) and pressing the fingerpad down against the force measurement platform, maximizing the contact area. The results are shown in Figure 23, Figure 24, and Figure 25.

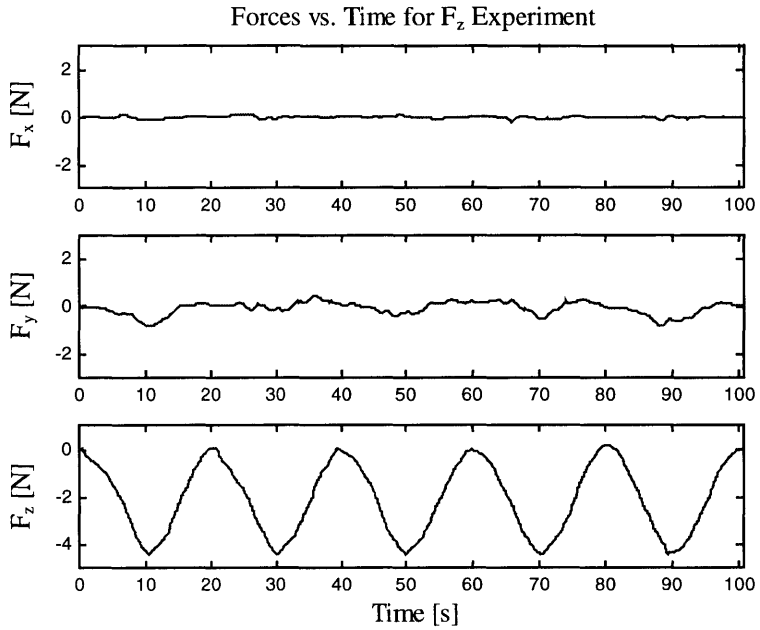

Figure 23: Application of Normal Force
A human subject presses down against the force measurement platform. The normal force, F_z is slowly cycled up and down while the shear forces are maintained at zero. Posture angles and contact angles are also maintained at zero.

The finger is slowly pressed down on the measurement platform with increasing force and then slowly lifted up again for five cycles at a rate of 0.05 Hz. The subject uses visual feedback in the form of gauges in order to keep the two shear forces at zero while cycling the normal force, F_z, between zero and –4 N. The force values from the 6-axis force sensor are plotted in Figure 23. The responses of the eight photodetectors are plotted vs. time in Figure 24.

As a visual aid, the plots are arranged in a configuration corresponding to the locations of the respective photodetectors on the fingernail. Furthermore, the scaling on the vertical axes is uniform over all eight photodetectors, allowing for a meaningful comparison of photodetector sensitivities.

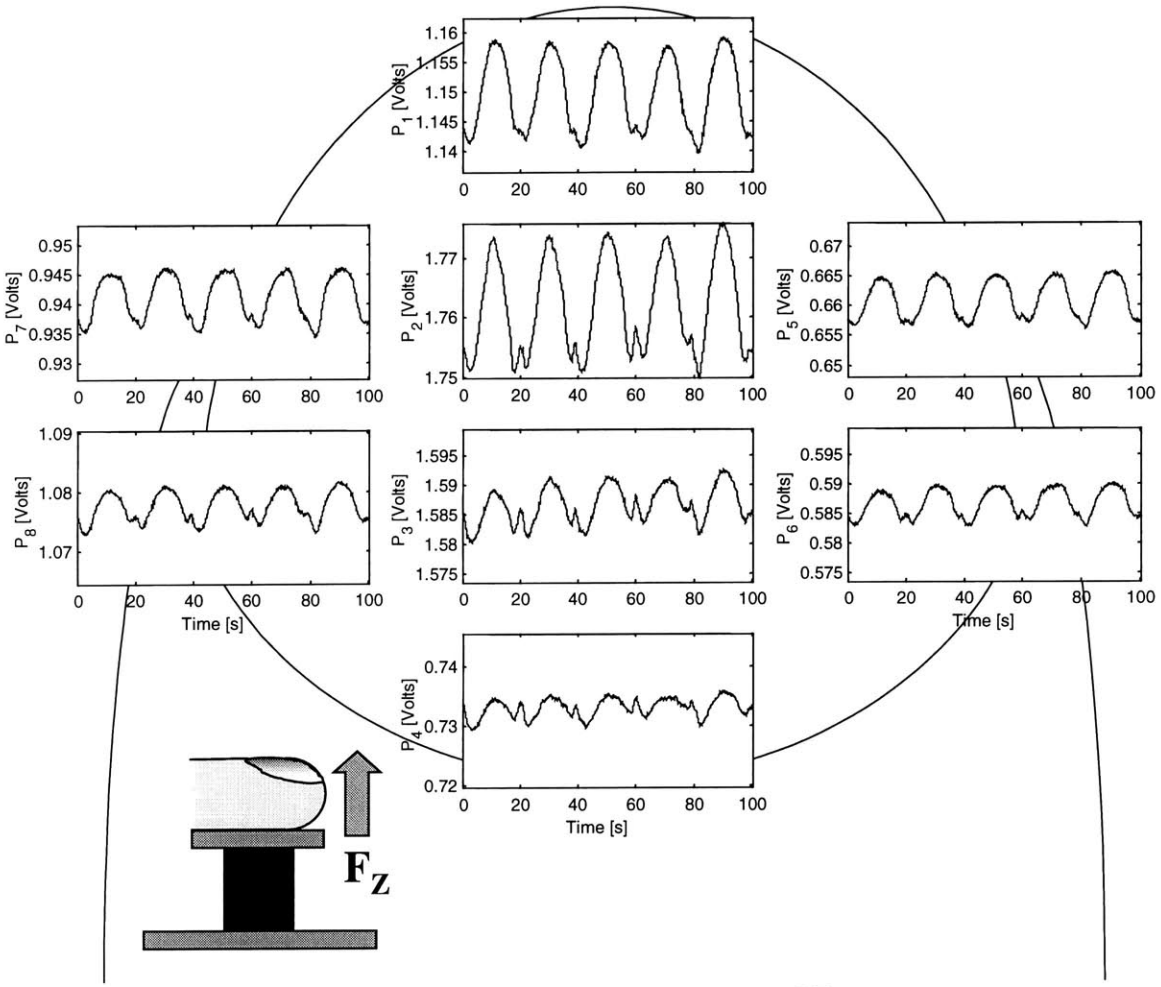

Figure 24: Sensor Output vs. Time for Normal Force
The outputs of the eight photodiodes are plotted vs. time. The plots are arranged according to the positions of the respective photodiodes on the fingernail surface.

In Figure 25, the photodetector outputs are averaged over the five cycles and plotted as functions of F_z, showing a characteristic pattern of sensor outputs for normal force. While some small amount of hysteresis is evident between increasing and decreasing force, the relationship is very repeatable across the five cycles, as shown by the small error bars representing the standard deviation. The results are also consistent with the color patterns described in Figure 5 in Chapter 2. The outputs of photodetectors 1 and 2, which are located toward the distal end of the nail,

increase with larger force, due to greater reflection from the whitening zone. Photodetectors 3 and 4, which are located toward the proximal end of the nail, display an initial voltage decrease with larger force due to less reflection from the reddening zone, followed by a slight increase due to more reflection from the encroaching whitening zone.

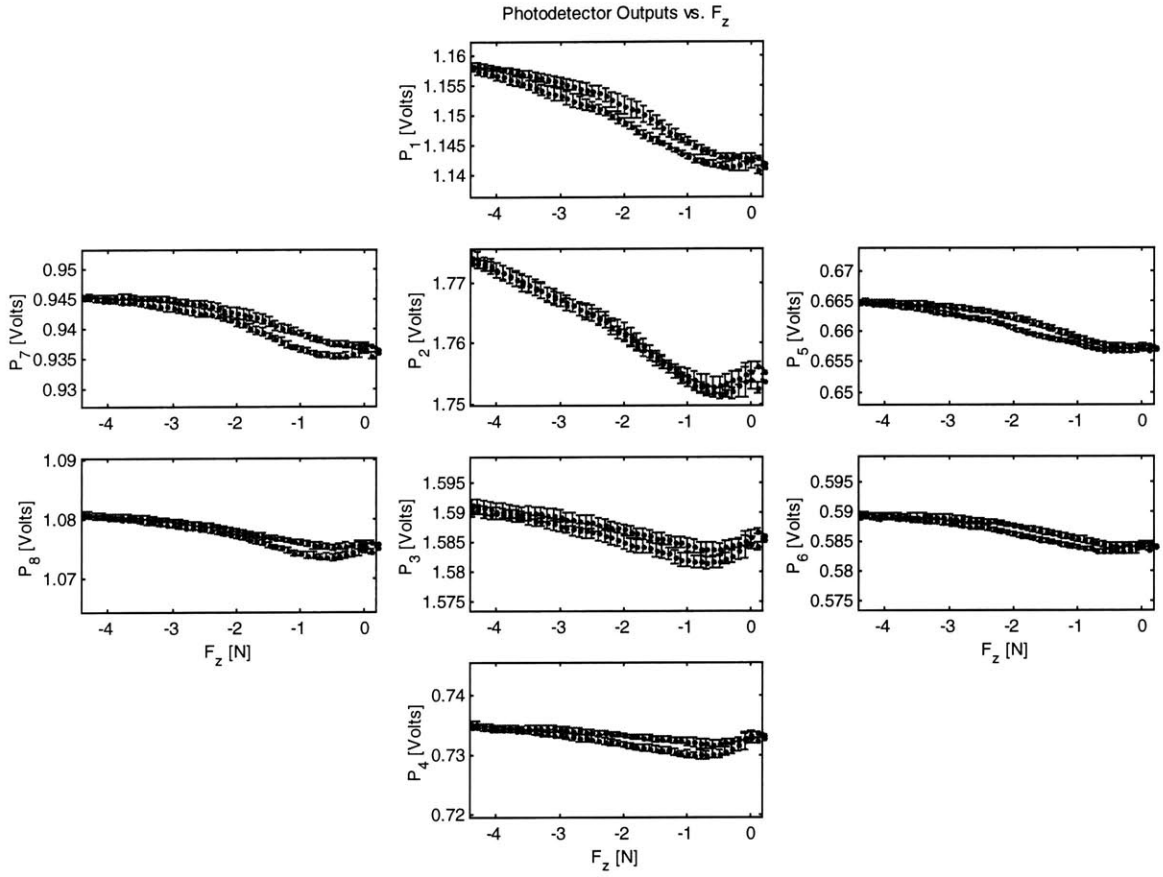

Figure 25: Sensor Output vs. Normal Force

The average outputs of the eight photodiodes over several cycles are plotted vs. the normal force with error bars corresponding to the standard deviations. The plots are again arranged according to the relative positions of the photodiodes. Some hysteresis is evident between the increasing and decreasing of the applied normal force.

3.3.3. Lateral Shear Force

Next, a human subject is instructed to apply lateral shear force, F_x, by pushing as if to drag the finger sideways along the rubber surface of the platform, while maintaining a constant normal force. The posture and contact angles are maintained at zero degrees as before. The results are shown in Figure 26, Figure 27 and Figure 28.

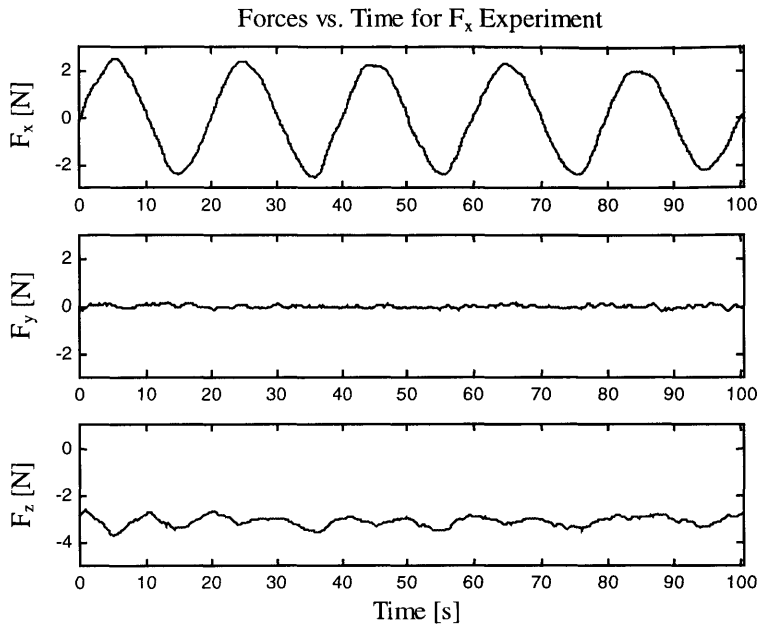

Figure 26: Application of Lateral Shear Force
A human subject presses down against the force measurement platform with constant 3 N of normal force and exerts a varying shear force in the x direction. The lateral shear force, F_x is slowly cycled back and forth while the longitudinal shear force is maintained at zero. Posture angles and contact angles are also maintained at zero. The normal force is difficult to maintain perfectly constant.

In this case, the subject is instructed to maintain a constant normal force of –3 N while slowly cycling the lateral shear force between positive and negative 2 N at 0.05 Hz. The force measurements are plotted in Figure 26 and the responses of the photodetectors are shown in Figure 27. For lateral shear force, unlike the case of normal force, the photodetectors do not all respond in phase. Photodetector 7 on the left side of the nail reacts in phase with the shear force while photodetector 5 on the right side of the nail reacts 180 degrees out of phase with the shear force. In Figure 28, the photodetector outputs are averaged over five cycles and plotted as functions of the applied lateral shear force, F_x, showing a characteristic pattern of sensor outputs for lateral shear. The opposite slopes for photodetectors 5 and 7 make this pattern easily distinguishable from the pattern for normal force. The results are repeatable as shown by the error bars, but do show significant hysteresis; however it is likely that at least some of this hysteresis is due to the inability of the human subject to maintain a constant normal force while cycling the shear force. As evidenced in Figure 26, the subject tends to apply normal force with a small but consistent oscillation with twice the frequency of the applied shear force.

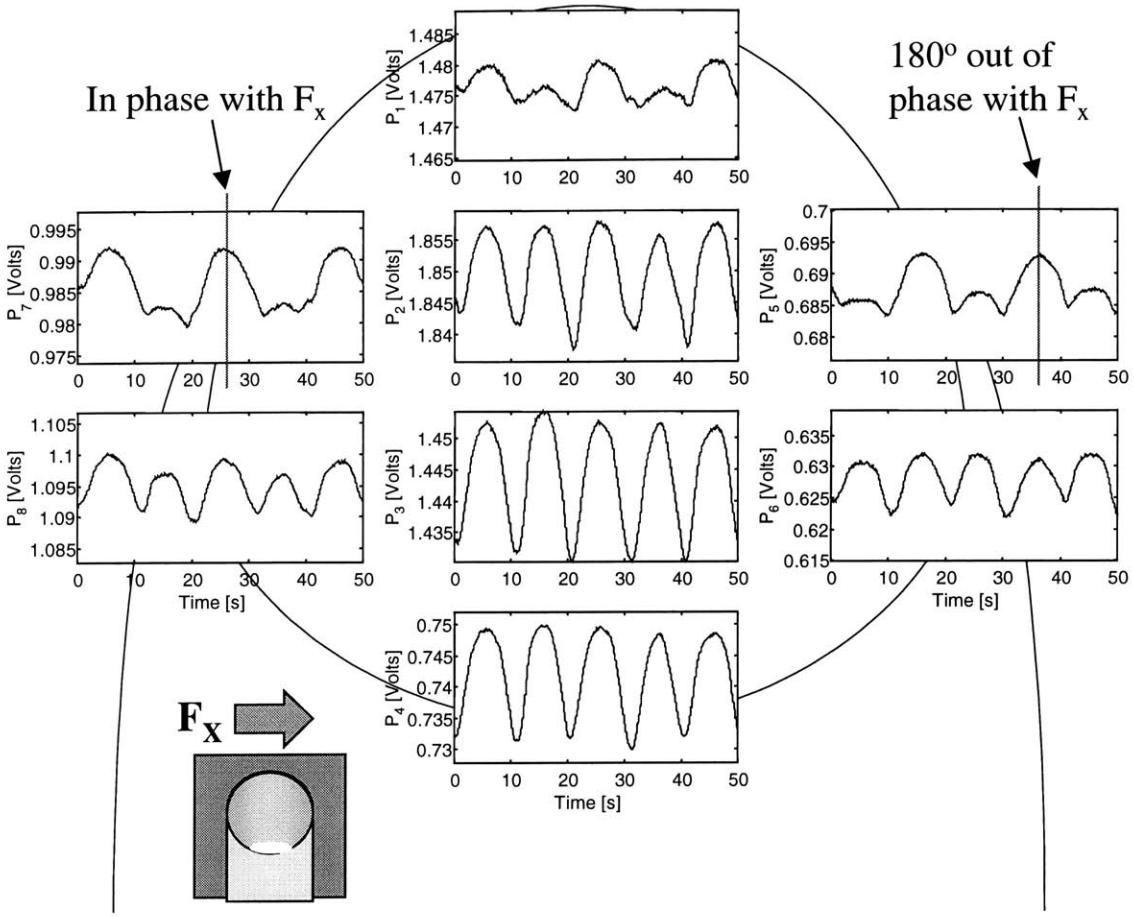

Figure 27: Sensor Output vs. Time for Lateral Shear Force
Photodiode outputs are again arranged according to photodiode location. For lateral shear force, photodiodes on the left side of the fingernail are in phase with the shear force while photodiodes on the right side of the fingernail are out of phase with the shear force.

The results in this case are also consistent with the color patterns depicted in Figure 7 in Chapter 2. As shown in Figure 28, the outputs of photodetectors 5 and 7 both increase when the finger pushes away from their respective sides of the fingernail, corresponding to the distal whitening and reddening patterns in Figure 7. Photodetector 1 stays relatively constant, since it is always over a white region. Photodetectors 2, 3, and 4 are symmetrical about F_x=0, increasing with shear force in either direction due to the central whitening/reddening patterns in Figure 7.

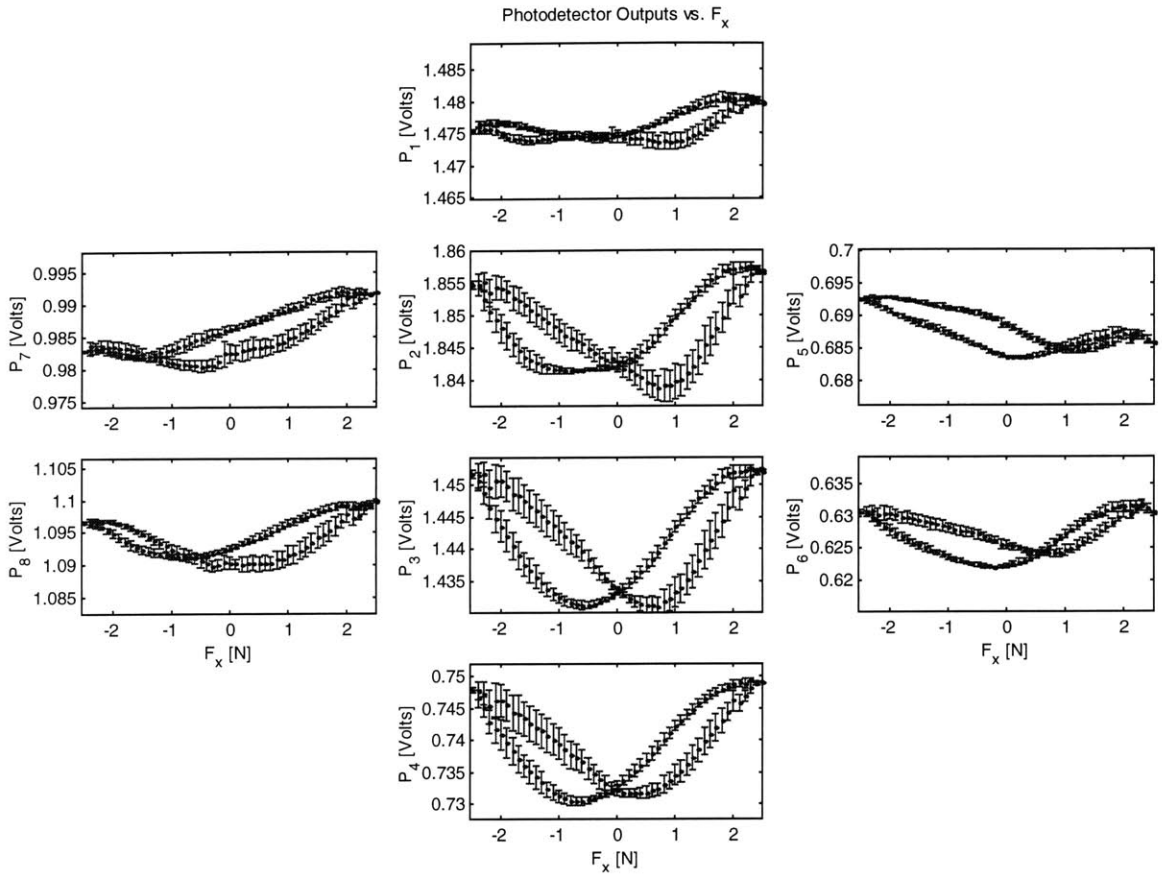

Figure 28: Sensor Output vs. Lateral Shear Force
The average outputs of the eight photodiodes over several cycles are plotted vs. the lateral shear force with error bars corresponding to the standard deviations. The patterns here are significantly different than for normal force. Hysteresis is again evident.

3.3.4. Longitudinal Shear Force

Next, a human subject is instructed to apply lateral shear force, F_y, while maintaining a constant normal force. The results are shown in Figure 29, Figure 30, and Figure 31. In this case, the subject is instructed to maintain a constant normal force of –3 N while slowly cycling the longitudinal shear force between positive and negative 2 N at 0.05 Hz. The force measurements are plotted in Figure 29 and the responses of the photodetectors are shown in Figure 30. Unlike lateral shear, the responses for longitudinal shear all seem to be in phase, but their sensitivities are very different for negative shear compared to positive shear. This is more evident in Figure 31, where the photodetector outputs are again averaged over five cycles and plotted as functions of the applied longitudinal force, F_y, showing a characteristic pattern of sensor outputs for longitudinal shear.

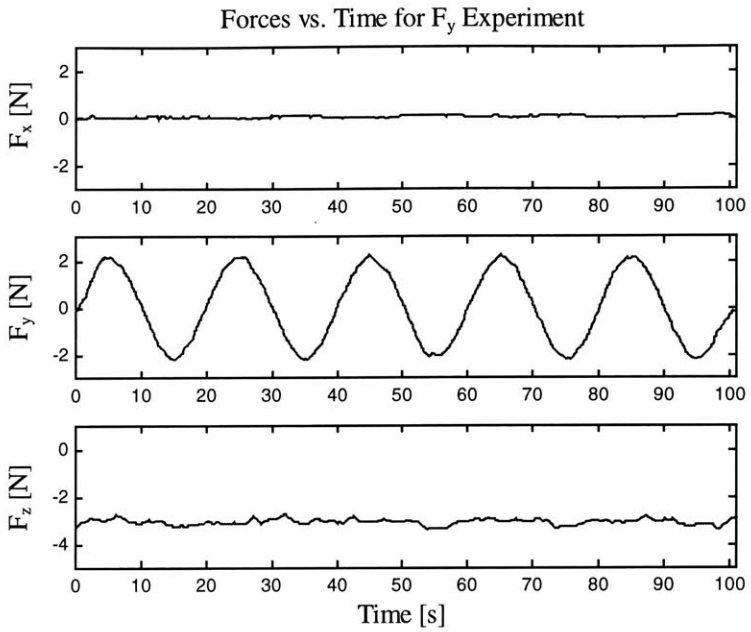

Figure 29: Applied Longitudinal Shear Force
The longitudinal shear force, F_y is slowly cycled back and forth with zero F_x.

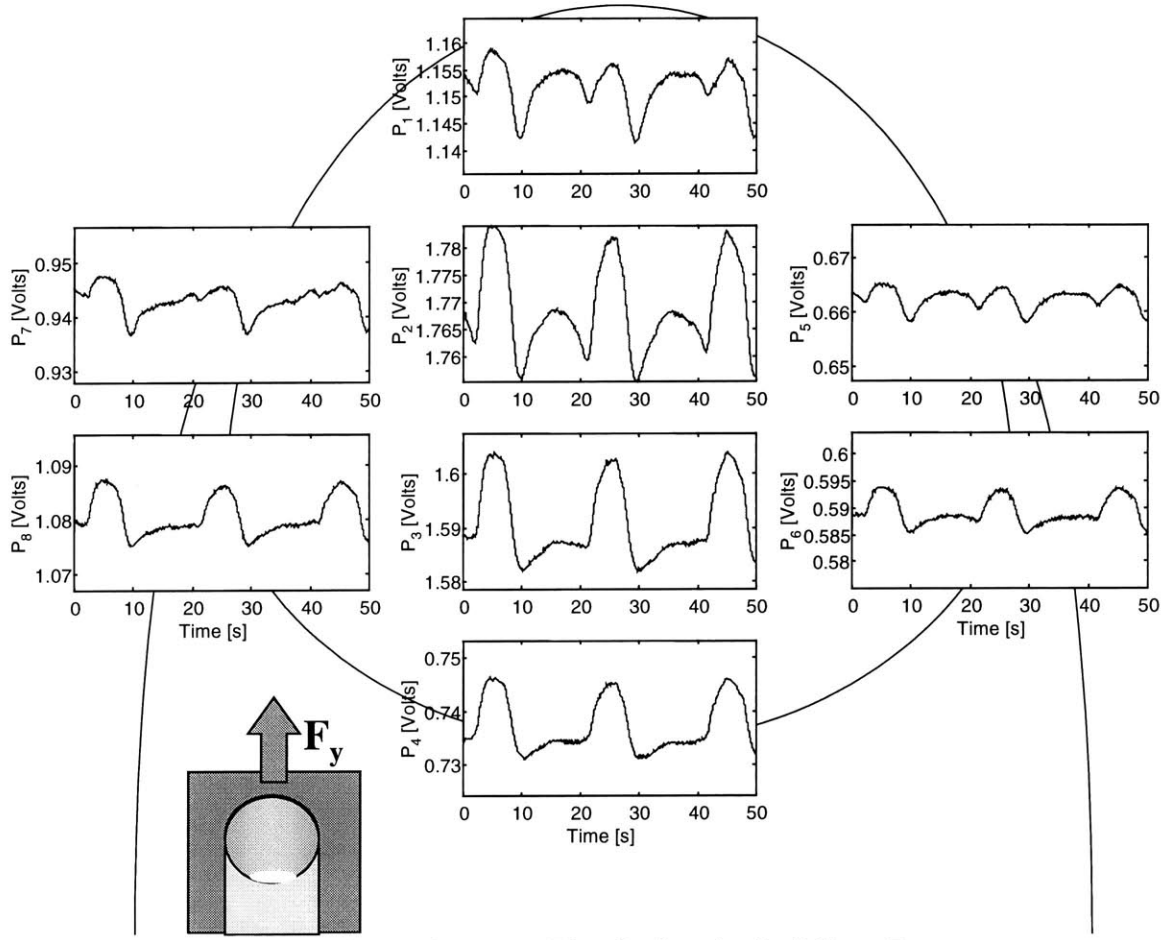

Figure 30: Sensor Output vs. Time for Longitudinal Shear Force
For longitudinal shear force, photodiodes are all in phase with each other.

Like the first two cases, the results in Figure 31 are very repeatable across the five cycles as evidenced by the relatively small error bars, but do show significant hysteresis, especially for photodetectors 1 and 2 toward the distal end of the nail. As shown in Figure 29, the subject is more successful at maintaining a constant normal force than in the previous case. Therefore, the hysteresis is likely due to some asymmetry in the mechanics of the fingerpad during the cycling. Unlike lateral shear, most of the photodetector outputs appear to be more sensitive to positive F_y than negative F_y. This is not surprising, since the color pattern for negative F_y described in Figure 7 does not appear to be significantly different from the color pattern for normal force alone. Photodetectors 1 and 2 do show some increase for negative F_y, corresponding to the distal whitening zone in Figure 7. The behavior for positive F_y is also consistent with Figure 7, since photodetectors 2, 3, and 4 all increase due to the central whitening zone.

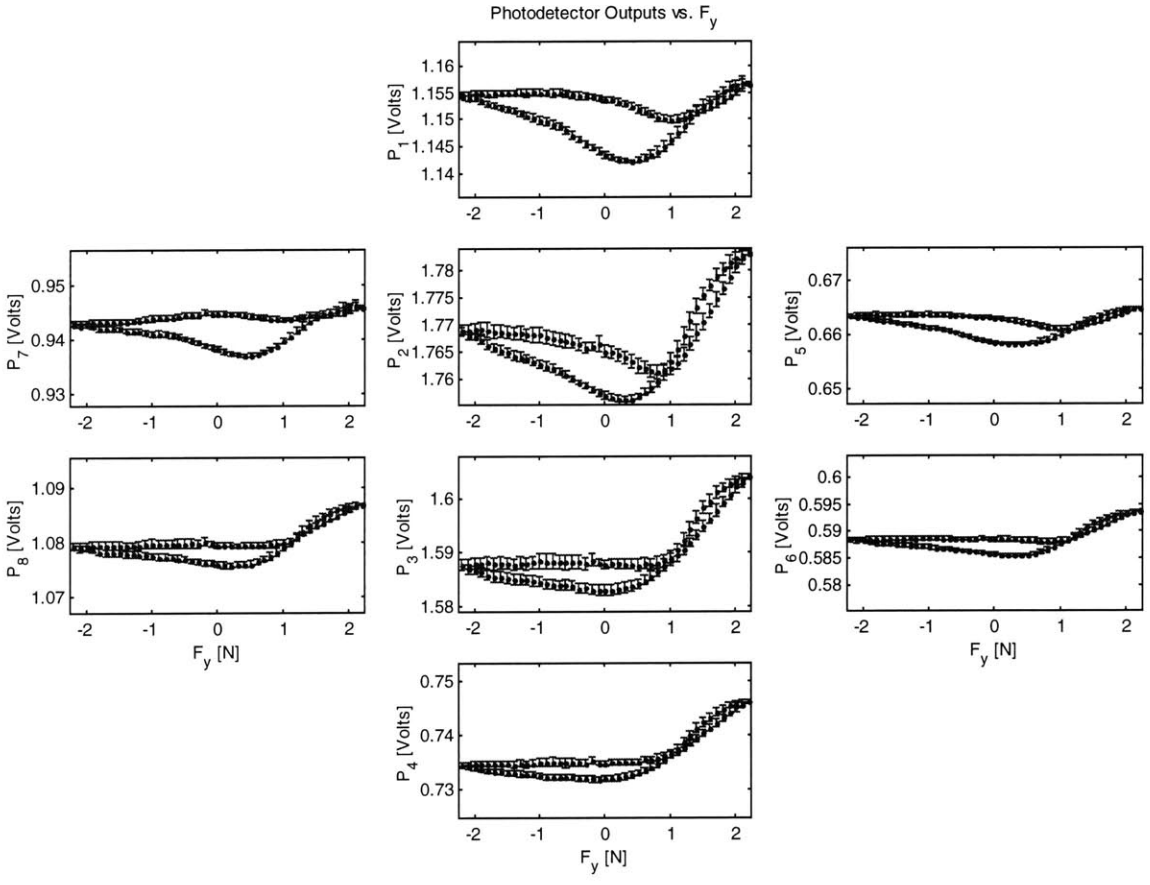

Figure 31: Sensor Output vs. Longitudinal Shear Force
The average outputs of the eight photodiodes over several cycles are plotted vs. the longitudinal shear force with error bars corresponding to the standard deviations. The patterns here are significantly different than both normal force and lateral shear force.

3.3.5. Bending

Finally, the response of the sensor to changes in finger posture is investigated. Figure 32, Figure 33, and Figure 34 show the results of experiments for finger posture measurement. Starting from a fully flexed position, a human subject fully extends the finger and then fully flexes once again. This action is repeated for six cycles at a rate of 0.1 Hz. The responses of each of the eight photodetectors are shown in Figure 32 for a single cycle. As shown by the data, the photodetector outputs all respond in phase with the bending with varying sensitivities.

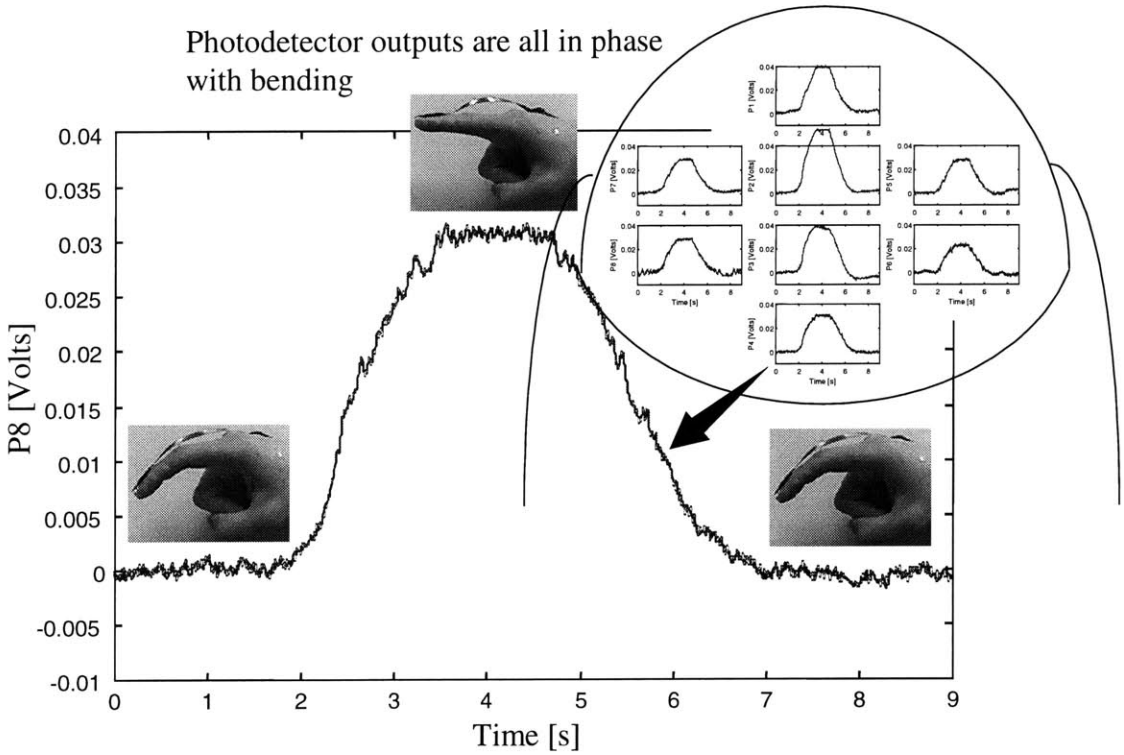

Figure 32: Sensor Output vs. Time for Finger Bending
A human subject alternately extends and flexes the finger. The photodiode outputs all behave in phase with each other.

Using the video tracking system shown in Figure 22, the joint angles were computed from video frames spanning the bending range of the finger. The finger consists of three joints, not all of which can be flexed independently. Figure 33 shows the correlation between the joints using data from the experiment. Since the knuckle joint can be flexed independently of the other two and does not appear to influence the photodetector outputs, the knuckle angle J_1 is held constant for this experiment. The proximal and distal interphalangeal joints, J_2 and J_3, cannot be flexed independently and have a roughly linear dependence, as shown in Figure 33. Therefore,

the photodetector outputs can be treated simply as a function of J_2 (hereafter referred to simply as θ), and are plotted as such in Figure 34, showing a characteristic pattern of sensor outputs for bending.

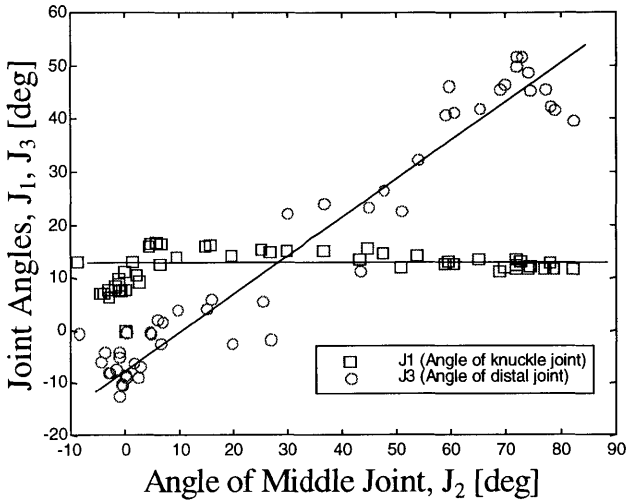

Figure 33: Correlation of Joint Angles

During free bending, the angles of the middle and distal joints are coupled to each other. The angle of the knuckle joint can be controlled independently, but does not influence the fingernail coloration. Therefore J_2 will be used to represent the posture of the finger.

For bending, the pattern of photodetector responses show very little hysteresis compared with touching, however the responses are not as repeatable over the six cycles as evidenced by the larger error bars compared to the plots for touching. The responses are most sensitive between the fully extended position (-10 degrees) and a one-third flexed position (25 degrees). Beyond 25 or 30 degrees of flexion, there is virtually no change in the photodetector responses.

The results are consistent with the color patterns due to bending described in Figure 6 in Chapter 2. The photodetector outputs all increase with extension and decrease with flexion, corresponding to the broad central whitening zone. Photodetectors 2 and 3, located most directly above the whitening zone, show the greatest sensitivities.

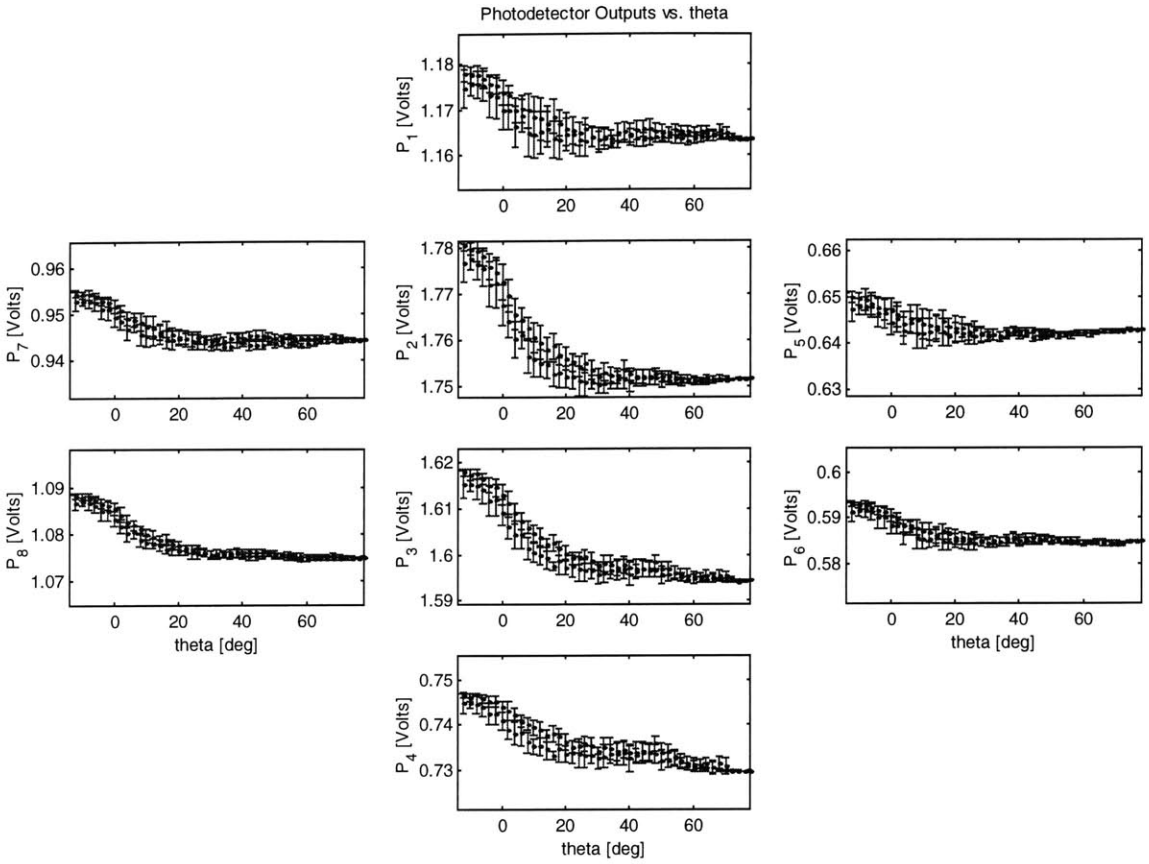

Figure 34: Sensor Output vs. Bend Angle

The average outputs of the eight photodiodes over several bending cycles are plotted vs. the angle of the middle joint, θ or J_2. The patterns here are different than those for touching. Relatively little hysteresis is evident compared to touching.

4. UNDERSTANDING OF THE MECHANISM

4.1. Anatomy and Physiology of the Fingertip

4.1.1. Structure and Function of the Fingertip and Fingernail

The goal of Chapter 4 is to develop a comprehensive understanding of the mechanism by which fingertip forces and finger extension/flexion change the coloration of the fingernail, or more accurately, the measurable blood volume beneath the fingernail. In order to explain this mechanism, it is necessary to thoroughly understand the relevant anatomy and physiology of the fingertip. First, the anatomical structure and function of the fingertip and fingernail is investigated. Secondly, the blood flow in the fingertip and fingernail bed is investigated. Based on these investigations and experimental photographic evidence, a generalized qualitative model for understanding the mechanism of color changes is then developed. Finally, a quantitative lumped-parameter hemodynamic model is created to simulate the static and dynamic behavior of the whitening and reddening phenomena.

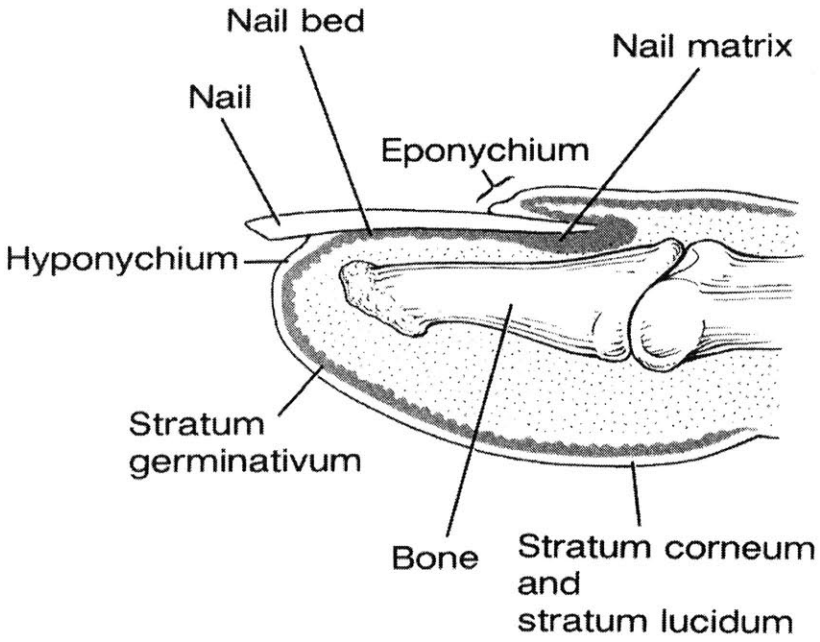

Figure 35: Structure of the Distal Human Fingertip
A sagittal cross-section of the fingertip shows the relative positions of the bone, fingernail, and surrounding tissue. Adapted from Spence (1982) with permission.

Details of the anatomical structure and function of the fingertip can be found in several references such as Spence (1992), Tubiana (1981, 1), Scher and Daniel (1997), Baran and Dawber (1994), Krstic (1991), and Zook, et al. (1980). Figure 35 shows a sagittal cross-section of the fingertip. The bones of the distal and middle phalanx meet at the distal interphalangeal joint (DIP). The bone of the distal phalanx is surrounded beneath by the soft deformable tissue of the pulp and above by the nail unit.

Movement of the finger and forces at the fingertip are effected by means of a network of flexor and extensor tendons, as shown in Figure 36 (Tubiana, 1981, 2; Simmons and Caffiniere, 1981; Valentin, 1981). The extensor tendons pull the finger up into an extended position, while the flexor tendons pull the finger down into a bent or flexed position. Some of the tendons are actuated by extrinsic muscles, located in the forearm, and are primarily responsible for power gripping. Others are actuated by the intrinsic muscles, located in the hand, and are primarily responsible for fine motions. At the DIP joint, the terminal extensor tendon and the deep flexor tendon are attached to the proximal end of the distal phalanx, exerting torques on the bone. Ligaments also connect the distal phalanx to the middle phalanx, preventing the DIP joint from separating and hyperextending (Duousset, 1981).

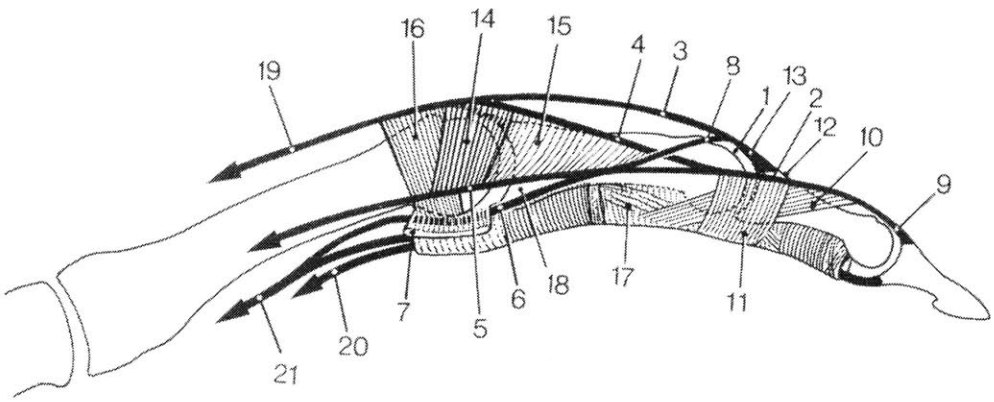

Figure 4–43. Diagrammatic view of the profile of a finger showing the insertions of the intrinsic and extrinsic muscles and the retinacular ligaments. There is a certain symmetry between the fibrous formations at the level of the metacarpophalangeal joint and the proximal interphalangeal joint. *1*, Central or middle extensor tendon. *2*, Lateral extensor tendon. *3*, Central band of the long extensor. *4*, Lateral band of the long extensor. *5*, Interosseous tendon. *6*, Lumbrical tendon. *7*, Deep transverse intermetacarpal ligament (or interglenoid). *8*, Central band of the interosseous. *9*, Terminal extensor tendon. *10*, Oblique retinacular ligament. *11*, Transverse retinacular ligament. *12*, Triangular ligament. *13*, Insertion of the extensor digitorum into the second phalanx. *14*, Transverse fibers of the interosseous hoods. *15*, Oblique fibers of the interosseous hoods. *16*, Sagittal bands. *17*, Fibrous sheath of the flexor tendons. *18*, Insertion of the interosseous on the base of P_1. *19*, Tendon of the extensor digitorum. *20*, Superficial flexor tendon. *21*, Deep flexor tendon.

Figure 36: Kinematics of the Human Finger
The distal joint is actuated by a network of flexor and extensor tendons, which are attached at the base of the distal phalanx (from Tubiana, 1981, 2, with permission).

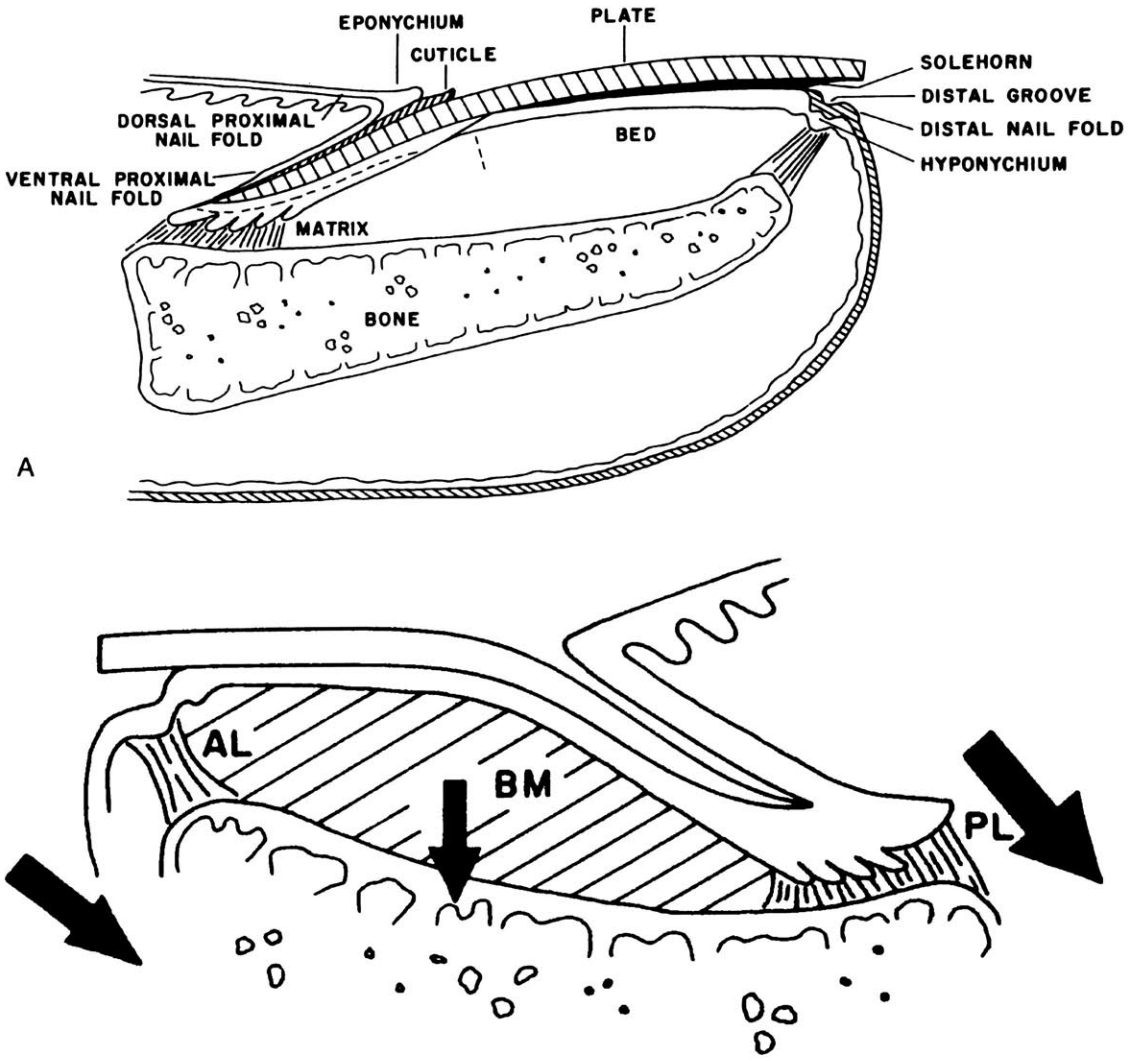

Figure 37: Nail to Bone Connection
The fingernail is attached to the bone via matrices of strong fibers or ligaments (from Gonzalez-Serva, 1997, with permission).

Figure 37 and Figure 38 show a more detailed anatomy of the fingernail and its relation to the bone. The nail plate itself is attached to the bone by the anterior ligament (AL), the posterior ligament (PL), and the bed mesenchyme (BM), the latter having an almost ligamentary or tendon-like character (Gonzalez-Serva, 1997). This anchoring serves to maintain the positional relationships and distances between the matrix, bed, hyponychium, and bone, which are critical for nail health and functionality. The nail plate is generated by the matrix, grows up and emerges out from under the proximal nail fold at the eponychium, curves over the nail bed, and separates from the fingertip at the hyponychium. The nail plate is approximately 0.5-0.6 mm

thick and has an average growth rate of 0.1 mm/day (3 mm/month), thus growing out completely in about 6 months (Fleckman, 1997).

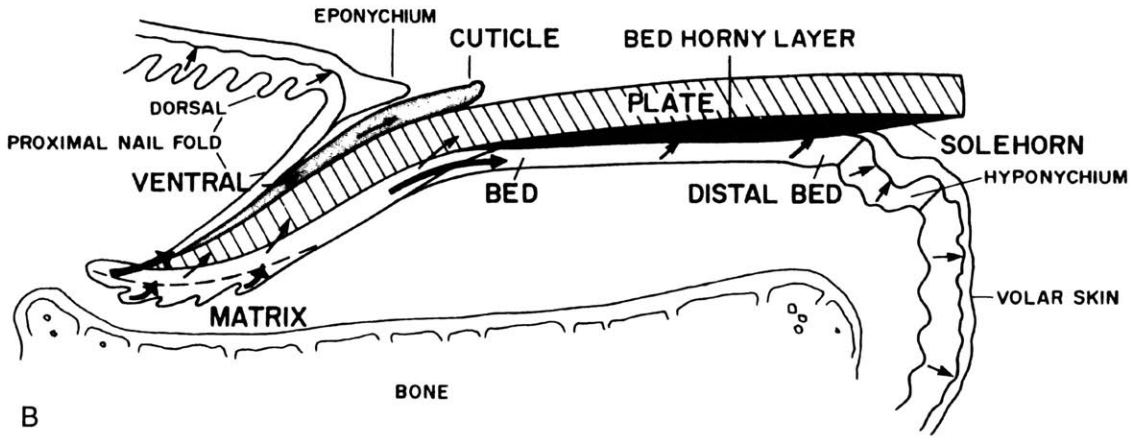

Figure 38: Nail Growth
The nail plate grows up out of the matrix, emerges at the eponychium, and separates at the hyponychium (from Gonzalez-Serva, 1997, with permission).

The nail unit has four known functions:

1. Protection of the phalanges and fingertips from traumatic impact
2. Enhancement of fine touch and fine digital movements
3. Scratching and grooming
4. Aesthetic and cosmetic organ

The second of these functions is very important to the field of haptics. As stated in Gonazalez-Serva (1997), "the nail plates act as buttresses that appose the fingertips, increasing the discriminatory ability of the acral pulp and skin whenever an object is grasped between two fingers: A half or a full pincer is provided by rigid peripheral nail plates. Such a pincer grip is even more efficient than the blunt support that would be provided solely by a pair of interphalangeal bones. The intensified sensory discrimination provided by the nail-enhanced pincer grip also permits additional dexterity when handling minute objects because it improves the capability for fine digital movements."

Figure 39 shows a dorsal view of the nail unit, which shows the various structures that influence the visible color of the fingernail. At the proximal end of the nail plate lies the cuticle, the visible portion of which is a webbed rim of material protruding from the eponychium. The lunula, which appears as a grayish-white zone, is the visible portion of the nail matrix. The

onychodermal band is the external expression of the solehorn, the distal part of the bed preceding the detachment of the nail, and has a glassy-grayish color. The nail bed is the area between the distal edge of the lunula and onychodermal band. According to Gonzalez-Serva, "After application of pressure to the pulp, this middle bed turns pinker while the distal bed that precedes the onychodermal band becomes whiter. This response to pressure, in the presence of the only gradually thickening nail plate and of a relatively uniform bed epithelium, supports the role of the bed vasculature as the main source of the pink color of the bed." This role will be discussed in detail in the following section. The nail plate itself is transparent and colorless, acting as a window into the nail bed. The distal edge of the plate where it is detached from the bed appears opaque due to increased refraction at the solid-gas interface.

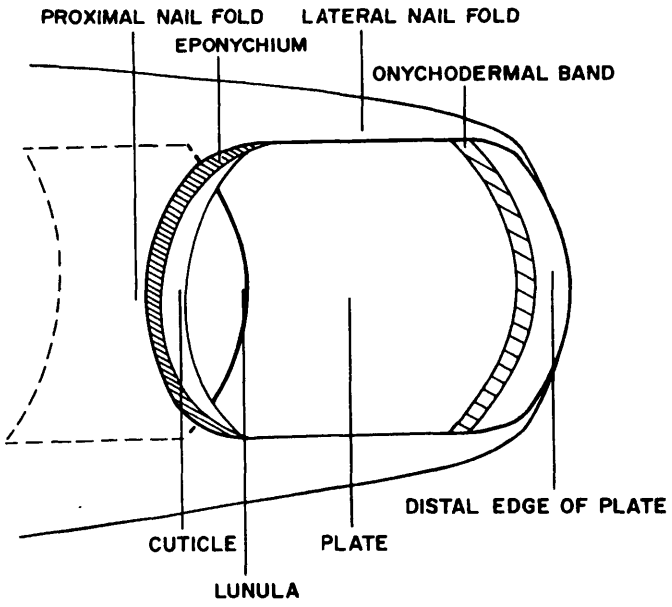

Figure 39: Dorsal View of the Nail Unit
A dorsal view shows the factor affecting nail coloration. The nail itself is transparent. The lunula is the visible portion of the matrix and the onychodermal band is the visible portion of the solehorn (from Gonzalez-Serva, 1997, with permission).

4.1.2. Blood Supply of the Fingertip and Nail Bed

A variety of details on the vascular anatomy of the fingertip can be found in several sources such as Tubiana (1981, 1), Fleckman and Allen (2001), Scher and Daniel (1997), Krstic (1991), Wolfram-Gabel and Sick (1995), Flint (1956), Zook et al. (1980), and Smith et al. (1991, 1 and 2). The nail bed is richly vascularized with blood flowing from the digital arteries into a network of arterioles, through capillary loops just under the surface, and back out through the

venules to the digital veins. Figure 40 shows each of the subdivisions of the vascular network and their accompanying blood pressure.

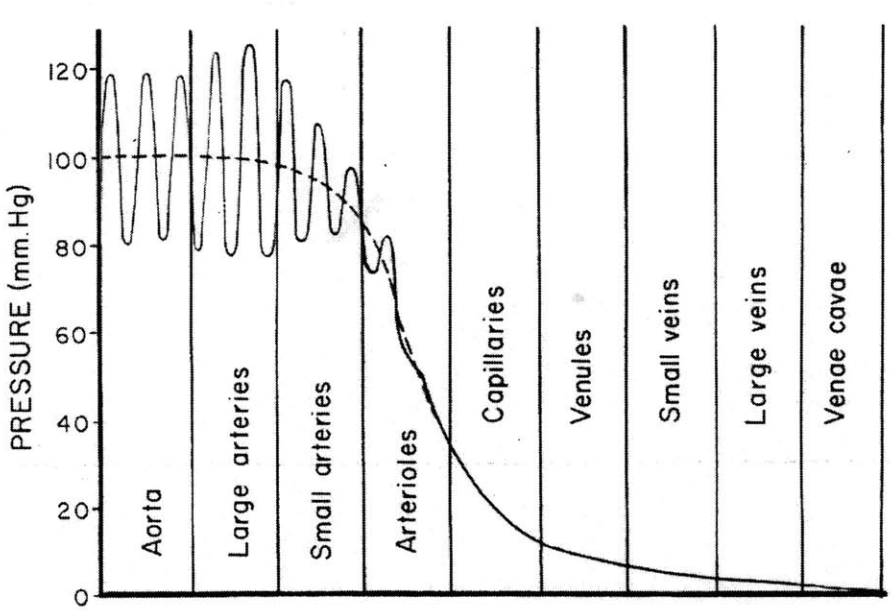

Figure 40: Blood Pressure in the Vascular System
The pulse is visible in the arteries but is damped in the capillaries and veins (from Guyton, 1981, with permission).

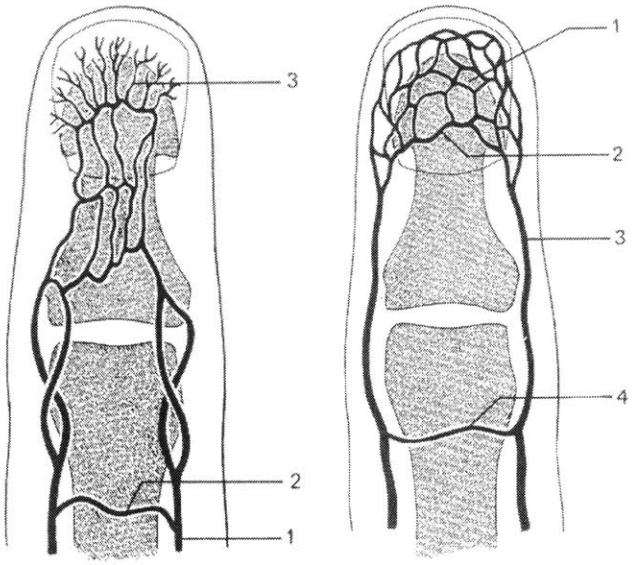

Figure 41: Dorsal View of Arteries and Veins
The arteries are located principally above the bone, while the veins are located principally to the sides of the bone and are more susceptible to collapse (from Pallardy, et al., 1981, with permission).

Figure 41 shows the anatomy of the digital arteries and veins. The main digital arteries divide into a network of smaller arteries that run principally above the bone, which is connected to the fingernail via a strong matrix of collagen and elastic fibers, as described in the previous section. As reiterated by Krstic (1991), the nails are effectively "immobile over the distal phalange." As a result, the arteries underneath the nail are protected from touch pressure, allowing uninterrupted supply of blood to the capillaries under the nail. However, the flow of blood out of the fingertip relies largely on the lateral ramifications of the digital veins shown in the figures (Smith et al., 1991, 2). In addition, the veins are generally larger and more compliant than the arteries, and have a smaller internal blood pressure than arteries, as shown in Figure 40, leaving them more susceptible to collapse by touch pressure (Guyton, 1981). As a result, when touch pressure is applied to the fingertip, the veins are collapsed, causing blood to pool up in the capillaries underneath the nail.

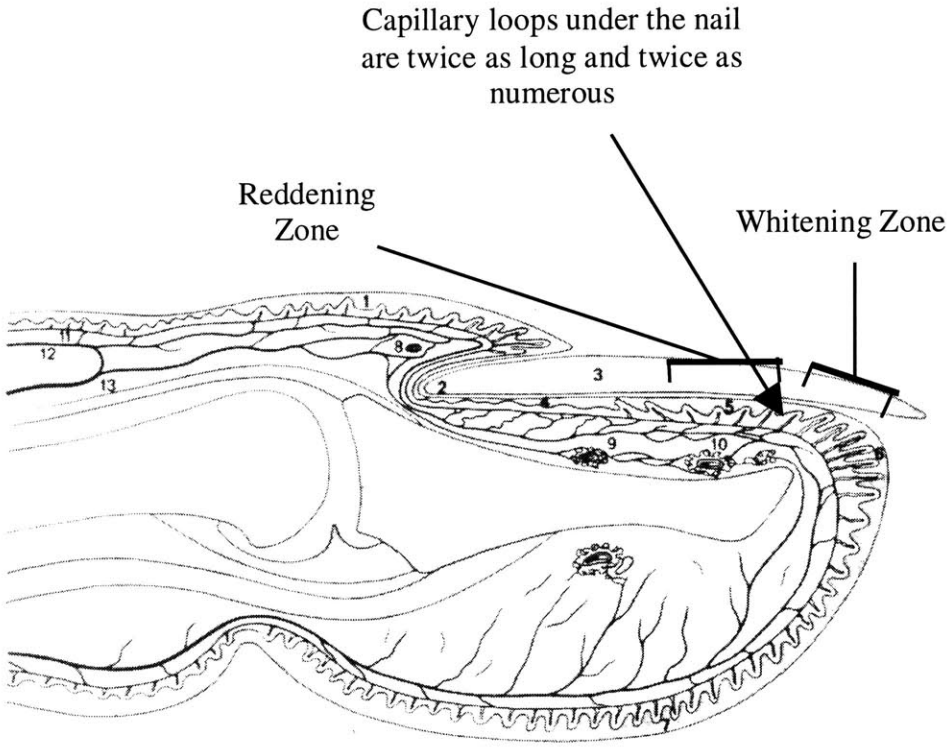

Figure 42: Capillaries of the Fingertip
Capillary loops under the fingernail are twice as long and twice as numerous as elsewhere in the skin (from Wolfram-Gabel and Sick, 1995, with permission).

The capillaries run longitudinally under the nail bed and are twice as long and twice as numerous as those in the pulp on the palmar side of the fingertip, as shown in Figure 42

(Wolfram-Gabel and Sick, 1995). Directionally the capillaries are vertical into the dermal papillae under the nail matrix, but longitudinal under the nail bed (Krstic, 1991). Thus the blood that pools up in the capillaries of the nail bed is highly visible and is responsible for the reddening effect described in Chapter 2. According to Guyton (1981), under normal conditions, the blood in the capillaries is rich in oxygen and therefore red. Figure 42 also shows that the capillaries under the nail at the tip of the finger are not protected by the bone. Thus touch pressure can propagate around the tip of the bone, causing these capillaries to collapse and pushing all of the blood out of them. This results in the whitening effect described in Chapter 2. As stated in Guyton (1981), "Thus, in conditions in which the cutaneous vessels become greatly constricted, the skin has an ashen white pallor," which is the color of the subcutaneous connective tissue, composed principally of collagen fibers.

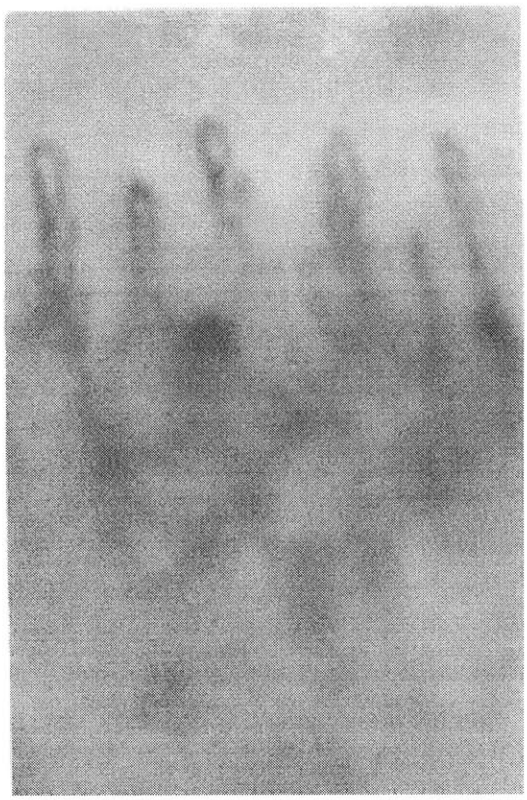

Figure 43: Capillaries of the Nail Bed
The capillary loops are visible as they extend upward (from Baran and Dawber, 1994, with permission).

Figure 43 shows a microscopic image of the capillary loops in the nail bed. Figure 44 illustrates how the capillary loops branch off the arteries and veins of the superficial plexus that parallels and connects to the deep plexus. The arteries and veins are also connected by arteriovenous shunts, which allow blood to bypass the capillaries. These shunts are constricted

and relaxed in order to control the blood flow and regulate body temperature. It is estimated that 90% of the blood flow to the hand occurs for the purpose of temperature regulation, while only 10% is required for nutrition (Montagna and Fellis, 1961; Tubiana, 1981, 2). According to Guyton (1981), when the skin is cold and the blood is flowing extremely slowly, most of the oxygen is consumed before the blood can leave the capillaries, and the deoxygenated blood gives the skin a bluish hue. Thus, the effect of temperature, while ignored in the subsequent models, will play an important role in sensor performance.

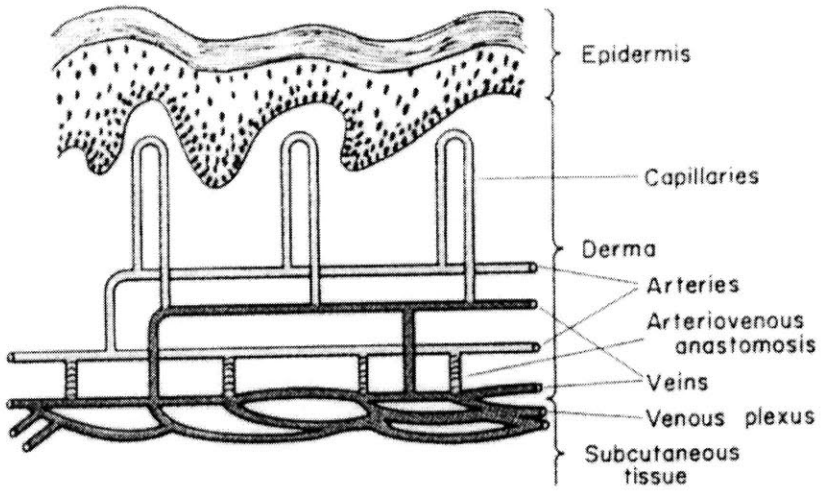

Figure 44: Anatomy of Microcirculation
The capillaries branch off in parallel from the arteries to the veins. Arteriovenous anastomoses also act as shunts between arteries and veins (from Guyton, 1981, with permission).

4.2. Bone-Nail Interaction

4.2.1. Basic Mechanism

Figure 45 shows a basic model of the nail-bone interaction that explains the mechanism behind the observable patterns of color or blood volume beneath the fingernail. As described earlier, the fingernail is connected to the bone of the distal phalanx by a matrix of strong fibers, especially around the perimeter of the nail, which prevent the nail from detaching from the bone, even under very high tension. However these fibers do not prevent the nail from being compressed against the bone. Touch forces and posture are maintained through tension in the flexor and extensor tendons, which are attached at the proximal end of the bone. The tendons are thus able to exert torque on the bone but do not directly affect tension in the tissue of the fingertip.

The bone itself has a distinctive arrowhead shape with protuberances at both ends where the fibers are attached. The bone does not extend all the way to the hyponychium where the nail detaches from the skin. This geometry is important in determining the regions of the nail bed that are affected by various forces within the fingertip.

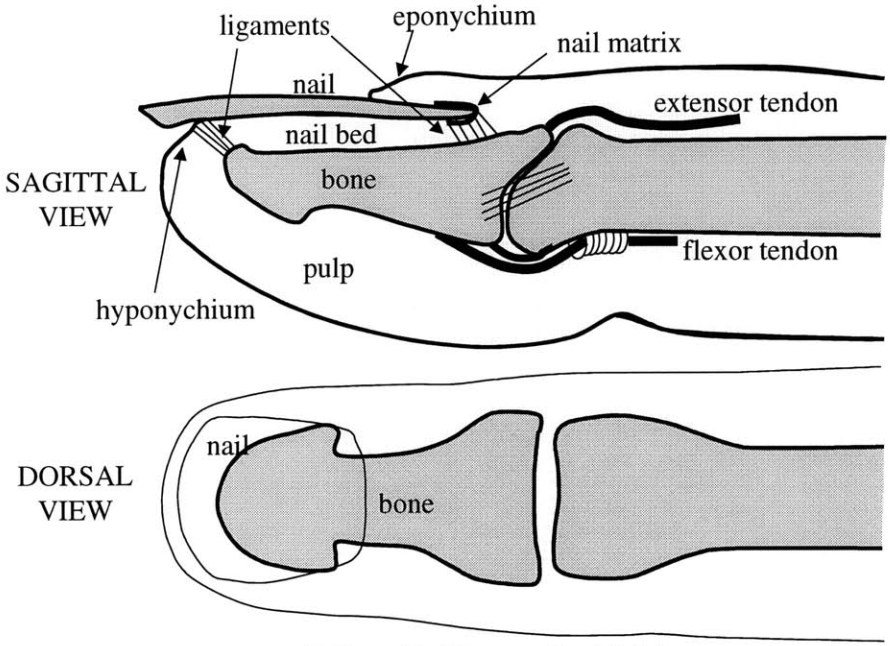

Figure 45: Bone-Nail Interaction Model
This model highlights the relative positions and connections between the fingernail and bone of the distal phalanx.

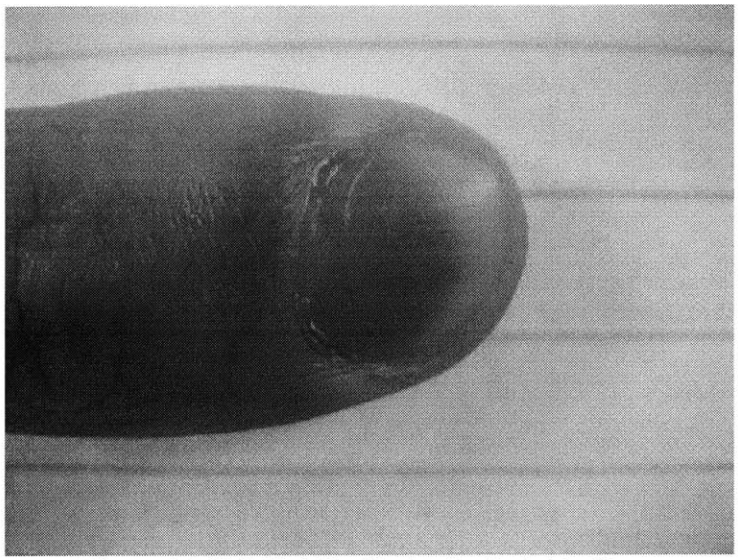

Figure 46: Nail-Bed Capillaries Protected by Bone
When the fingertip is pressed flat against a surface, the capillaries above the bone are protected, while the capillaries around the bone are collapsed.

The shape and position of the bone and its effect on the nail bed capillaries is evidenced in Figure 46 and Figure 47. In Figure 46, the finger is pressed down against a flat surface. The profile of the bone is visible as the region of red where the capillaries are protected from collapsing due to the pressure. In Figure 47, the nail is pressed against a transparent surface. In this case the profile of the bone is visible as the region of white where the capillaries between the nail and bone are compressed and collapsed, which also confirms the inability of the nail fibers to support compression.

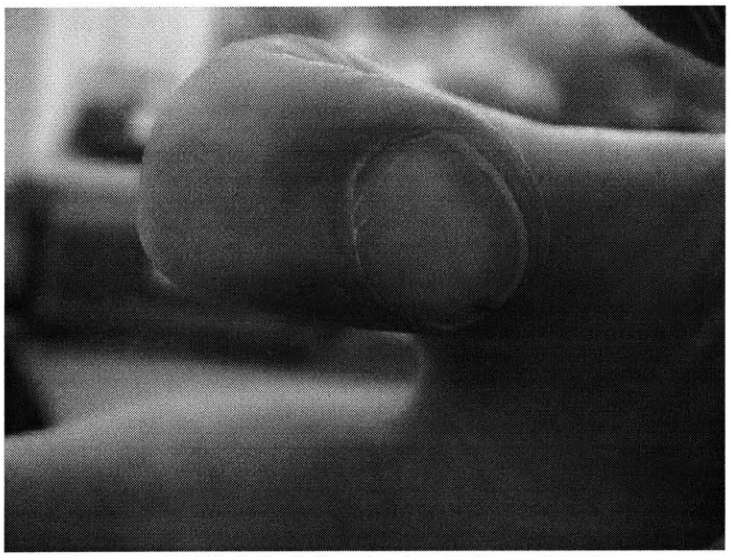

Figure 47: Nail-Bed Capillaries Collapsed by Bone
When the fingernail is pressed against a clear pane of glass, the capillaries above the bone are collapsed, while the capillaries around the bone remain filled with blood.

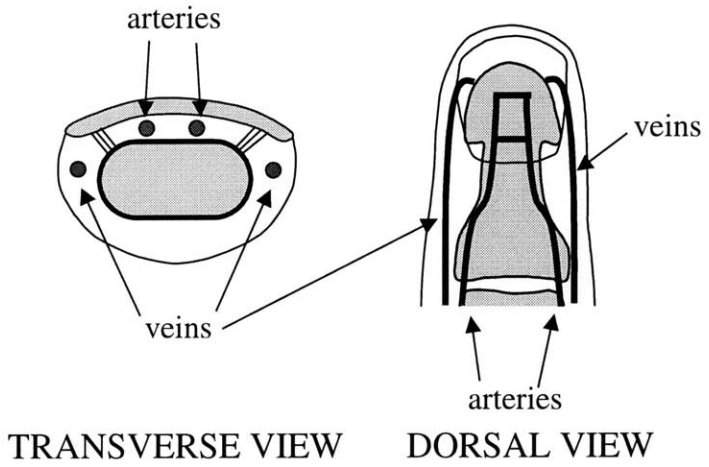

Figure 48: Arterial vs. Venous Positioning
The relative positions of the arteries and veins are highlighted. The arteries are principally above the bone, while the veins are to the side of the bone.

It is also important to reiterate the positions of the main digital arteries and veins relative to the bone. Figure 48 illustrates how the arteries run mainly above the bone, while the veins run mainly beside the bone, where they are exposed to pressure from below. When the veins are collapsed, blood pools upstream in the capillaries, resulting in a reddening effect.

The important characteristics of the basic bone-nail interaction model can be summarized by the following principles:

- The bone (distal phalanx) has a distinctive arrowhead shape with protuberances at both ends
- The fiber matrices between nail and bone support tension but not compression
- Tension in the tissue allows capillary blood volume to increase while compression causes capillary blood volume to decrease
- Compression of the veins causes blood to pool up in the capillaries

This basic model is now ready to be applied to explain the mechanism behind the fingernail coloration that results from each of the various types of touch force and posture. For each type of force or posture, photographic evidence of the nail coloration will be used to identify regions of tension and compression and infer the mechanisms by which the nail and bone interact to create these tensions and compressions.

4.2.2. Photographic Evidence

In Chapter 2, the different patterns of fingernail coloration were briefly illustrated. However, in order to accurately apply the basic bone-nail interaction model, photographic evidence of the various patterns of coloration (due to changes in blood volume) should be collected for a number of human subjects. In this study, digital images were collected for 16 different subjects: 11 male and 5 female. For purposes of categorizing skin color, 7 subjects were white, 7 were Asian, and 2 were black. In order to uniformly photograph the subjects, an apparatus was designed as shown in Figure 49. The 3-axis force-sensing platform described in Chapter 3 is placed within an enclosed chamber to block ambient lighting. A 1.0 MegaPixel CCD digital camera with 10x optical zoom is mounted above the force-sensing platform in order to image the fingernail as the finger is pressed against the platform with various forces. Using an

attached close-up lens, the camera is able to maintain focus while zoomed in such that the fingernail fills the entire 640x480 frame.

The two key features of the apparatus are the lighting and the filtering. The lighting is extremely important, because the fingernail surface itself is highly reflective. If the light shines from anywhere in front or beside the fingernail, the downward-curving fingernail surface will directly reflect light back up into the lens, resulting in a glare that washes out the coloration beneath the nail. However, if the light is placed directly behind the fingernail, over the hand, as shown the figure, the curvature of the nail will reflect the light out away from the lens. In this situation, the only light that reaches the lens is the light that penetrates the nail bed and is diffusely reflected back out. The configuration in Figure 49 is also fine for photographing finger extension, as long as the hand is titled forward so that the nail surface remains level with respect to the lens. However, in order to photograph the nail during finger flexion, the hand must be turned upside down to position the nail level with respect to the lens, as shown in Figure 50. In this case, the hand must be inserted from the opposite side of the chamber to prevent glare from the light source.

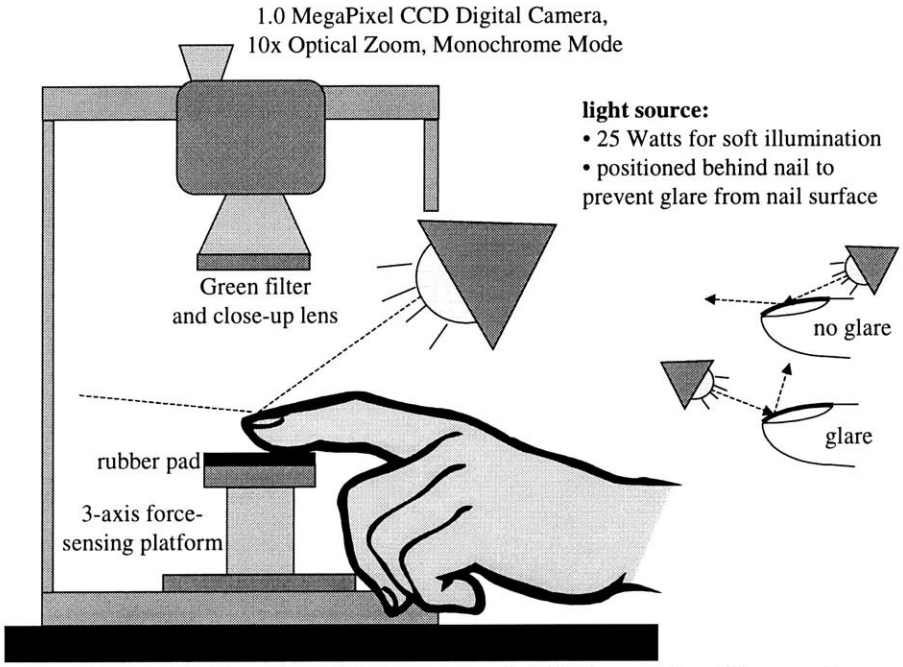

Figure 49: Experimental Apparatus for Photographing Fingernail
CCD camera images the fingernail coloration while the finger is pressed against the force platform with specified force. The angle of light source is critical to prevent direct glare from the nail surface, so that color patterns are mainly representative of light scattered back from the nail bed.

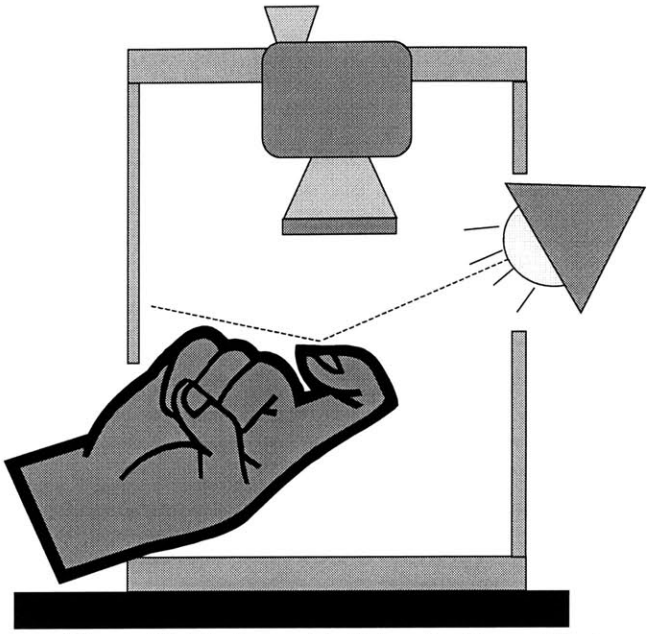

Figure 50: Photographic Setup for Finger Flexion
A similar setup allows for imaging color patterns due to posture changes.

The second key feature of the apparatus is the filtering. In order to maximize the contrast between red and white areas of the fingernail, color filtering can be applied. When sample images are broken down into their RGB (red-green-blue) components, results show that the "red" and "white" areas of the fingernail differ mainly in their green component, while the red and blue components are almost identical. Therefore, the green component should be isolated and used to generate a monochrome (or grayscale) intensity image. The most flexible solution is to digitally filter the image by software once it has been downloaded to the computer. However, the process of acquiring useful images involves feedback between the subject, camera, and photographer. Without monitoring a well-contrasted image on the LCD screen, the subject and/or photographer cannot judge the quality of the image and are often unaware that the finger is not properly illuminated or level with the lens or that the shear force is being incorrectly generated by rolling the finger rather than dragging it. Therefore, the filtering is placed in the feedback loop by attaching a green filter to the camera lens and operating the camera in monochrome mode. Once the grayscale image has been downloaded to the computer, the contrast can be further enhanced by scaling the intensity values, or by applying thresholds or other filters.

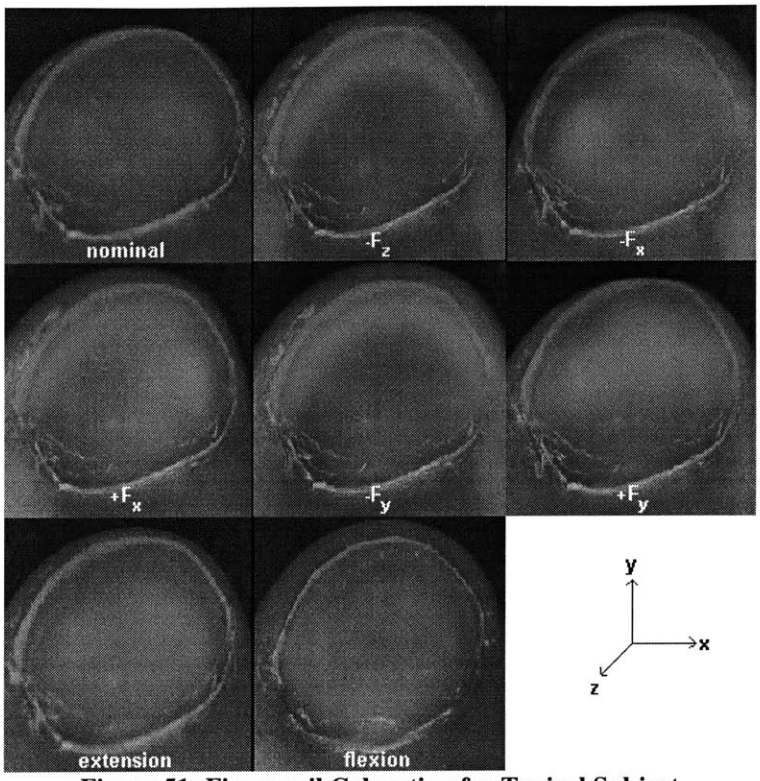

Figure 51: Fingernail Coloration for Typical Subject
Each image corresponds to a particular force or posture pose as subtitled.

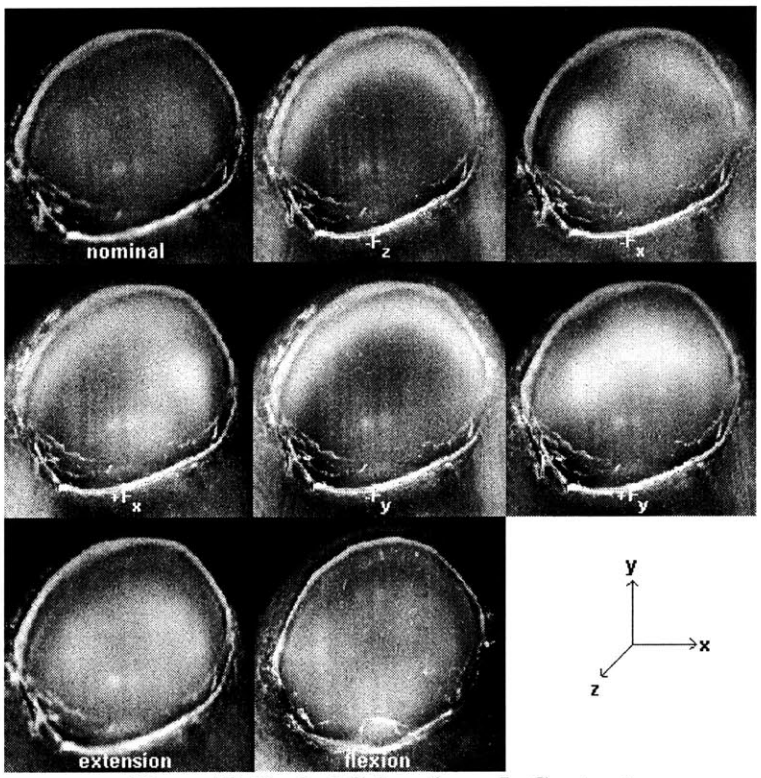

Figure 52: Typical Coloration – 5x Contrast
The images from Figure 51 are presented here with the intensities scaled by a factor of five to enhance contrast between white zones and red (dark) zones.

Figure 51 shows a sequence of images taken for a typical subject. The first image is the nominal coloration of the fingernail when no force is applied and the finger is held straight out. For the second image, a normal force of -3 N is applied. Then lateral and longitudinal shear forces of negative and positive 2 N are applied. Finally, images are taken of the finger fully extended and fully flexed. Figure 52 shows the same sequence of images after the contrast is enhanced by scaling the intensities up by 5 and renormalizing. More specifically, the intensities in the 30-50% range were linearly mapped to the entire intensity range (0-100%, or 0-255). As a result, the contrast between red (dark) and white areas of the fingernail is highly visible.

All 16 subjects were photographed in the same eight poses. In order to compile the images for all 16 subjects into meaningful results for any particular pose, the intensity values were averaged across all the subjects, resulting in an "average" fingernail image, depicting the average pattern of coloration. First, the sizes of the images were all normalized according to the length and width of the fingernail. The length was defined as the maximum distance in the y-direction from the eponychium (where the nail emerges from the proximal nail fold) to the hyponychium (where the nail separates from the distal bed), and the width was defined as the maximum distance in the x-direction between the lateral nail folds. Then the images were all uniformly cropped about the center of the nail to 125% of the normalized nail size, leaving a small area visible around the nail. The resulting images were all 400x400 pixels, with a 320x320 pixel fingernail in the center. Finally, the intensity value for each pixel was averaged across the 16 subjects. The results are shown in Figure 53.

In Figure 54, the contrast is enhanced using a 30-50% linear mapping as before. As evidenced in the figure, the poses result in significantly different average patterns of coloration with well-defined dark and white zones, corresponding to the reddening and whitening zones, respectively. The zones stand out even further when a threshold filter is applied as shown in Figure 55. In this case, all the pixels with intensity greater than 105 are mapped to 255, and all other pixels are mapped to zero.

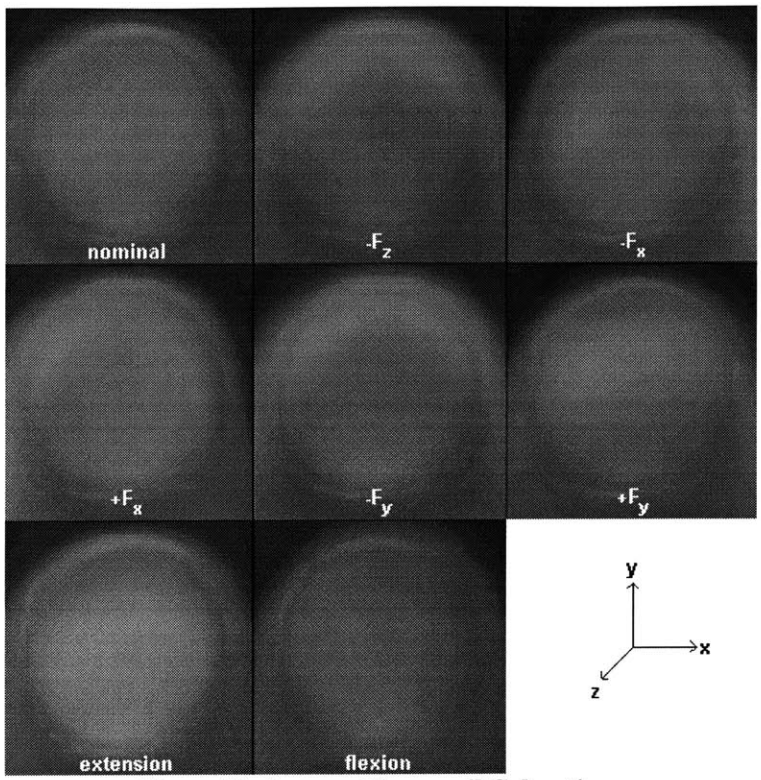

Figure 53: Average Fingernail Colorations

The same eight force/posture poses are averaged for 16 human subjects. Images from the subjects were normalized to the same size and averaged pixel by pixel.

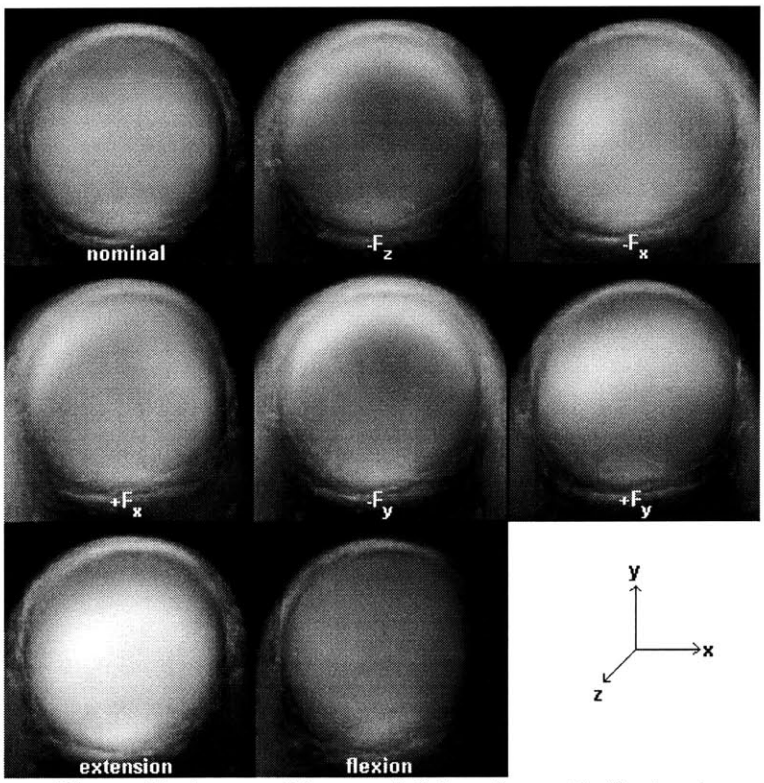

Figure 54: Average Fingernail Colorations – 5x Contrast

The images from Figure 53 are scaled five times in intensity to enhance contrast.

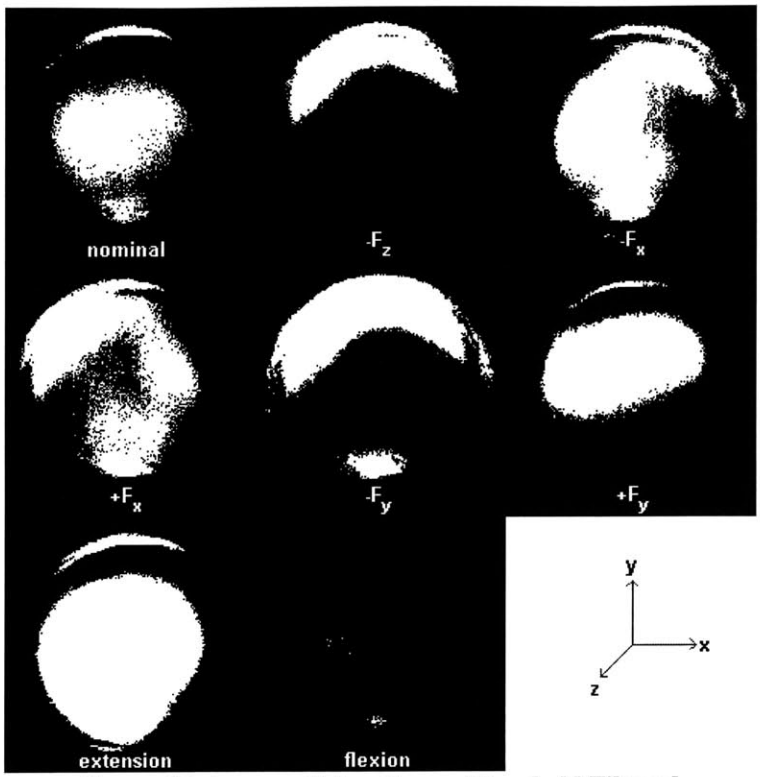

Figure 55: Average Colorations – Threshold Filtered
A threshold filter further enhances contrast between red and white zones.

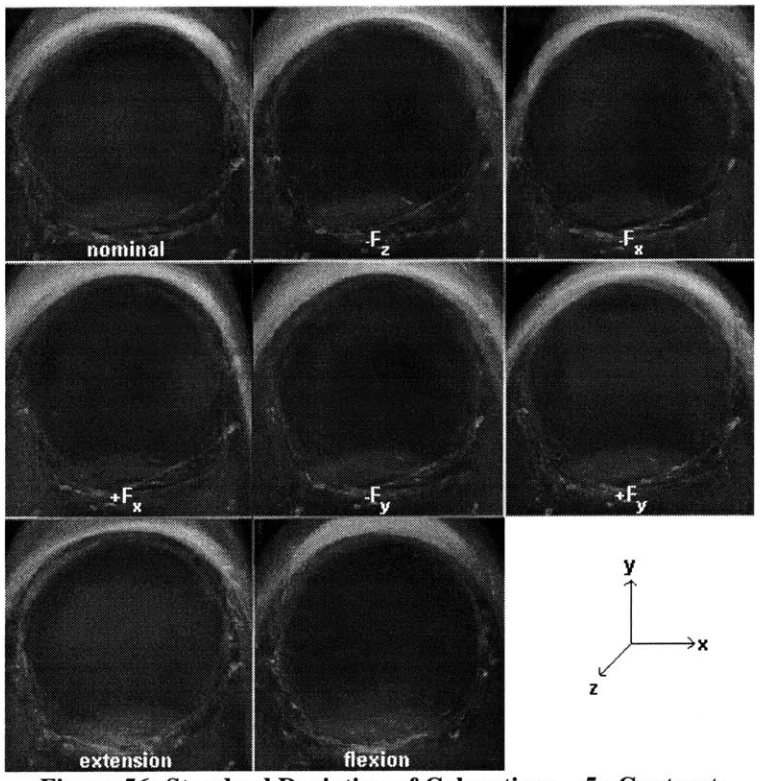

Figure 56: Standard Deviation of Colorations – 5x Contrast
Standard deviation across 16 subjects is computed pixel by pixel. The dark areas represent areas of low standard deviation between subjects.

Finally, Figure 56 shows the images that result from the standard deviation of the pixel intensities across all 16 subjects with the contrast scale up by 5, using a 0-20% linear mapping. The standard deviations are relatively high (white regions) all around the perimeter of the nail due to differing lengths of trimming, shapes of the nail folds, and visibility of the lunula. However, the standard deviations are relatively low (dark regions) and uniform across the nail bed, indicating that the subjects all react with similar color patterns for each pose. Therefore, it is justifiable to create a qualitative model of the color change mechanism that is applicable to people of various skin colors and fingernail sizes.

4.2.3. Normal Force

Figure 57 and Figure 58 depict the average visible effect of normal touch force on the fingernail, using the photographic evidence from the previous section. The average nominal coloration in Figure 57 shows a slightly white area over the bone. When normal force is applied, as shown in Figure 58, the area around the bone is whitened, while the area above the bone is reddened.

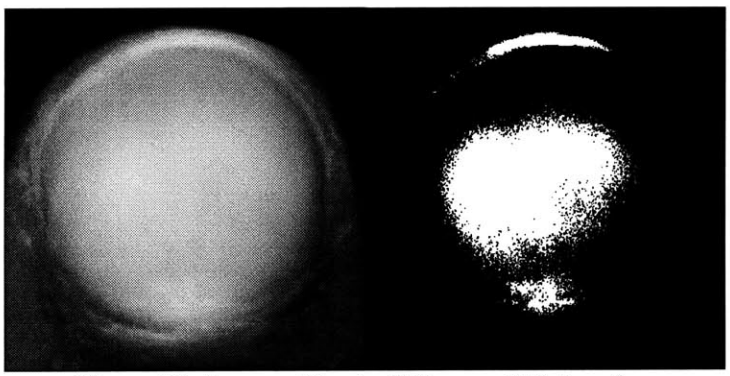

Figure 57: Average Nominal Fingernail Coloration
The average nominal coloration from Figure 54 and Figure 55 is here enlarged.

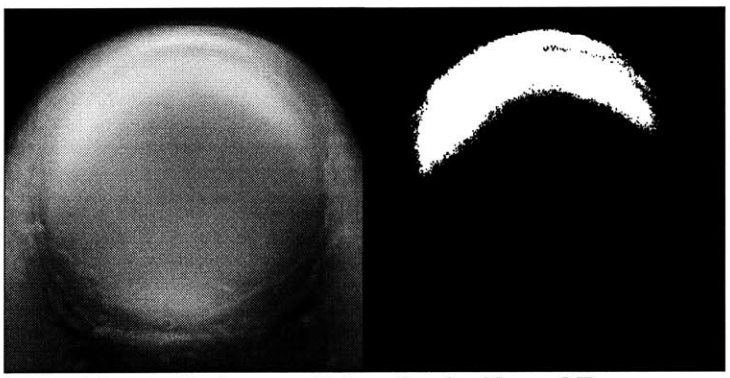

Figure 58: Average Coloration for Normal Force
Normal force causes the formation of a distal white zone and proximal red zone.

Figure 59 illustrates the mechanism behind this effect. The top diagrams depict the nominal state of the fingertip when no force is applied. The tissue is colored light gray to indicate it is neither in tension nor compression. The transverse and dorsal views also depict the primary arteries (over the bone) and veins (beside the bone). The bottom diagrams show a negative z-force exerted beneath the fingertip and its corresponding reaction force exerted by the bone, which is achieved by tension in the flexor tendon. These forces compress the tissue of the pulp between the bone and the surface, as depicted by the area in white. Note that the compression extends to the area around the bone as well as beneath it. This is because the nail bed fibers are in tension and pull the nail down with the bone, compressing all the tissue that is around the bone but beneath the nail. This includes the lateral aspects of the finger where the primary veins lie. Thus the veins are collapsed, causing blood to pool up in the protected capillaries between the nail and the bone, as depicted by the area shaded in dark gray.

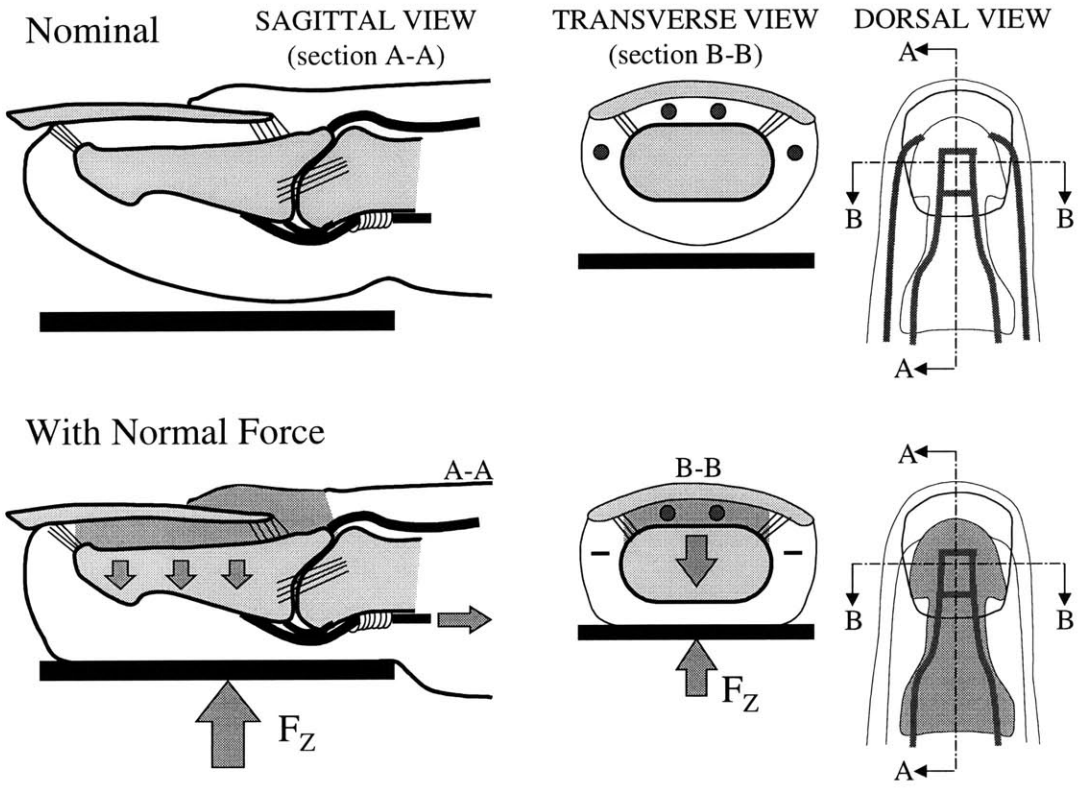

Figure 59: Normal Touch Mechanism
As the flexor tendon pulls the bone down to generate normal force, the tissue beneath the bone is compressed. The bone-nail connection causes the nail to be pulled down also, compressing tissue at the fingertip, resulting in a distal white zone. The lateral veins also collapse, causing blood to pool above the bone.

4.2.4. Extension/Flexion

Figure 60 and Figure 61 depict the average visible effects of finger extension and flexion on the fingernail. When the finger is extended, whitening occurs between the bone and the fingernail, especially at the distal end of the bone. When the finger is flexed, the whitening disappears and the entire nail reddens.

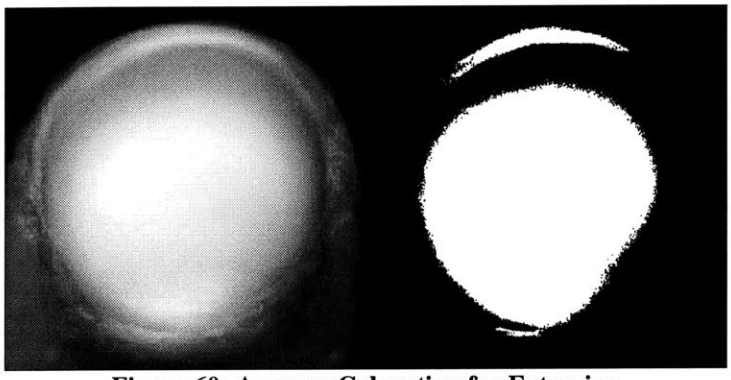

Figure 60: Average Coloration for Extension
Extension causes the formation of a proximal white zone and distal red zone.

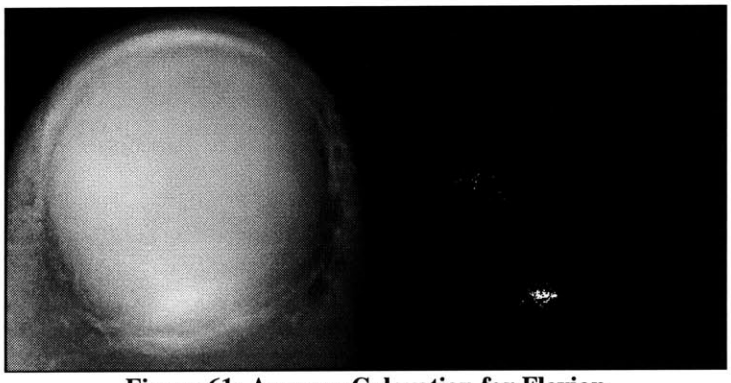

Figure 61: Average Coloration for Flexion
Flexion causes the disappearance of white zones and an overall reddening effect.

Figure 62 illustrates the mechanism behind this effect. During extension, the extensor tendon pulls the bone upward against the fingernail, which is held in place by a reaction force from the proximal nail fold. Since the fibers of the nail bed do not support compression, the capillaries are collapsed between the bone and the nail, especially above the bony protuberance at the distal end of the bone.

When the finger is flexed, the flexor tendon pulls the bone down away from the nail, relieving the compression between the nail and bone. Since the nail bed fibers are now in tension, the fingernail maintains a normal position relative to the bone. However, additional

reddening occurs throughout the fingertip since flexion of the finger kinks the veins, causing blood to pool up in the capillaries throughout the fingertip. Figure 63 shows how the arteries (unlike the veins) are tortuous so that blood can enter the fingertip even though it cannot exit.

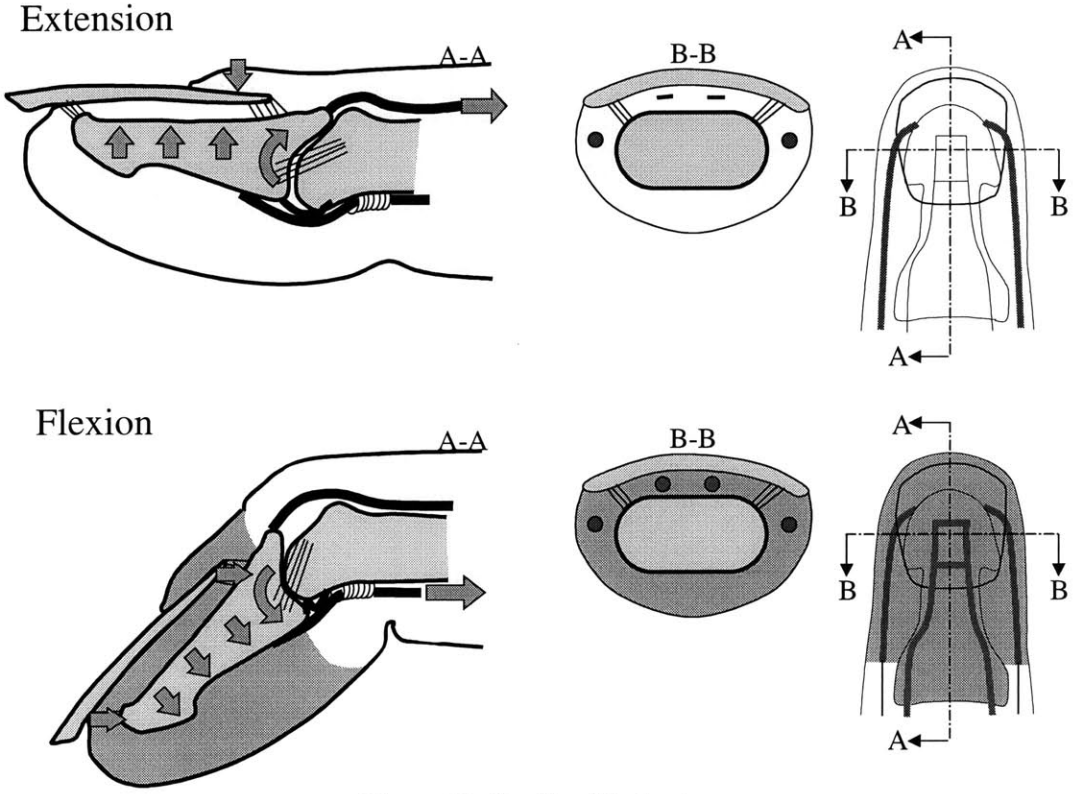

Figure 62: Bending Mechanism
As the extensor tendon pulls the bone upward to extend the finger, the tissue between the nail and bone is compressed.

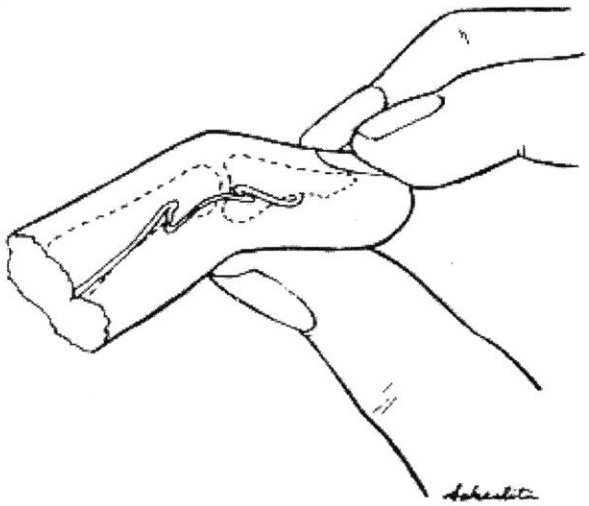

Figure 63: Arterial Tortuosity
The arteries are tortuous or coiled (unlike the veins), which prevents them from collapsing during flexion (from Smith, et al., 1991, 1, with permission).

4.2.5. Lateral Shear Force

Figure 64 and Figure 65 depict the average visible effects of lateral shear force on the fingernail. In Figure 64, a negative lateral shear force is applied (finger sliding to subject's left), while in Figure 65, a positive lateral shear force is applied (finger sliding to subject's right). In both cases, the fingernail whitens around the bone on the far side of the nail (opposite direction of sliding), as well as over the bone toward the near side (in direction of sliding).

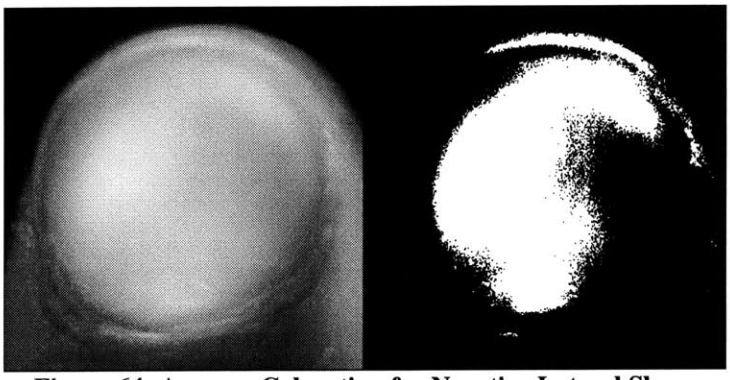

Figure 64: Average Coloration for Negative Lateral Shear
Lateral shear force causes a more complex pattern of red and white zones.

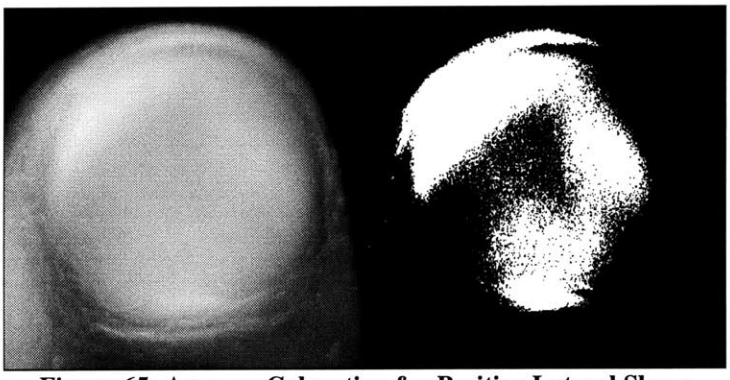

Figure 65: Average Coloration for Positive Lateral Shear
The pattern is almost mirrored when the direction of lateral shear is reversed.

In this case, the mechanism is more complex, as illustrated in Figure 66. In order to apply shear, a normal force must be simultaneously exerted in order to allow for friction. It has already been established that when normal force is applied, the area around the bone is compressed and whitened. When lateral force is exerted in addition to normal force, a lateral reaction force is maintained in the bone by the ligaments of the joint, and the tissue of the pulp between the bone and surface experiences a shear force that pulls the tissue toward the far side of the nail. Thus the tissue at the far side becomes bunched up around the nail due to shear and whitened due to compression by the normal force. However, on the near side of the nail, the tissue is pulled away

from the nail by the shear force. The tension of this pulling action prevents compression of the tissue at the near side, resulting in reddening. Furthermore, the tension at the near side pulls the nail down on top of the bone there resulting in whitening.

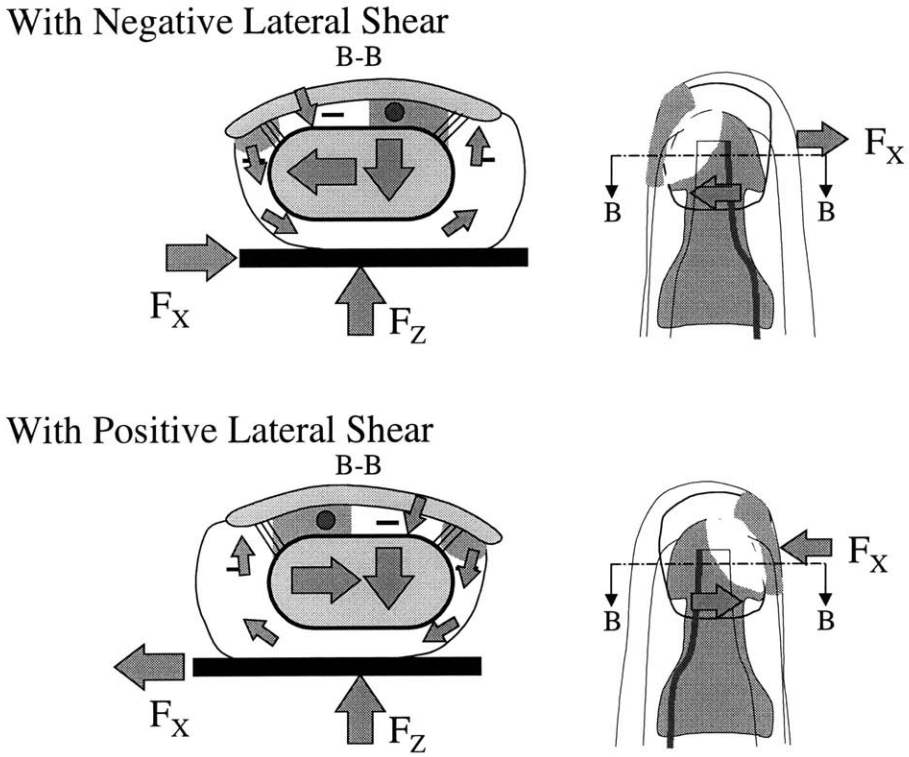

Figure 66: Lateral Shear Mechanism

When lateral shear is applied, the tissue is pulled from one side of the bone to the other resulting in compression on one side and tension on the other. The nail is also pulled down onto one side of the bone and away on the other, causing secondary white and red zones above the bone.

4.2.6. Longitudinal Shear Force

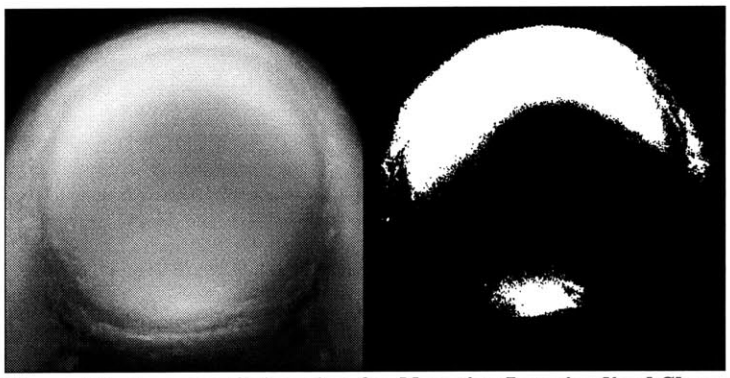

Figure 67: Average Coloration for Negative Longitudinal Shear

Negative longitudinal shear results in a proximal red zone and a distal white zone that is similar to the case of normal force alone but slightly larger.

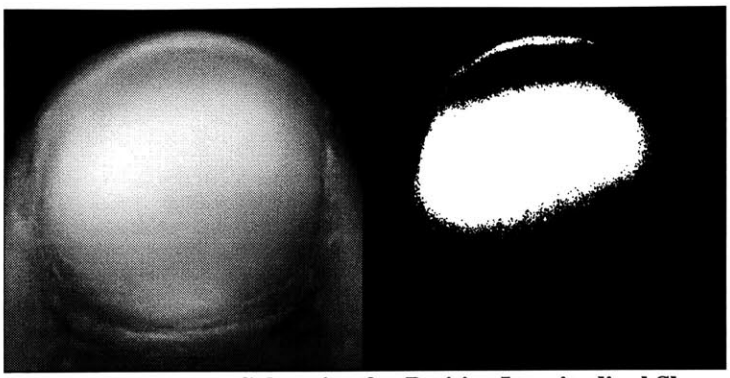

Figure 68: Average Coloration for Positive Longitudinal Shear
Positive longitudinal shear results in a distal red zone and a proximal white zone that is similar to the case of extension but has a different shape.

Finally, Figure 67 and Figure 68 depict the average visible effects of longitudinal shear force. Figure 67 depicts negative longitudinal shear applied to the finger (finger pulling backward). In this case, we see whitening around the bone, not significantly different from normal force alone. Figure 68 depicts a positive longitudinal shear applied to the finger (finger pushing forward). In this case we see whitening over the bone, but reddening at the tip.

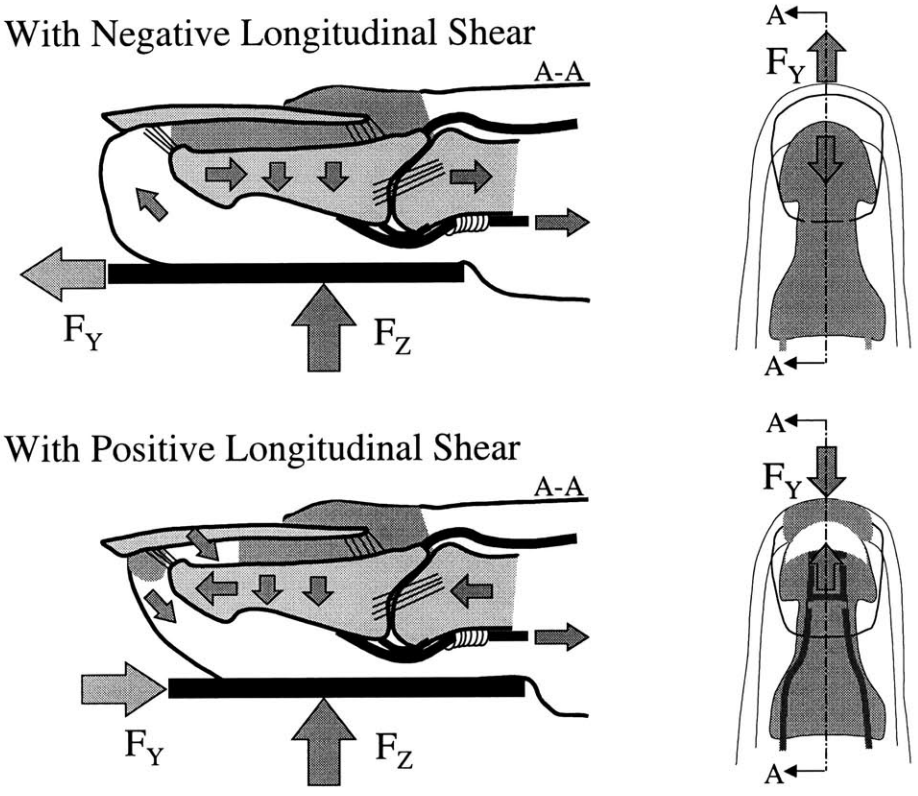

Figure 69: Longitudinal Shear Mechanism
When longitudinal shear is applied, the tissue is either pulled from or pushed to the fingertip, causing tension or compression at the tip. Also, the nail is either pushed toward or pulled away from the bone, causing proximal effects.

Unlike lateral shear force, the mechanism of longitudinal shear force is different for positive and negative forces, as illustrated in Figure 69. When force is applied in the positive direction, as shown in the bottom diagrams, the mechanism is similar to lateral shear. Applied shear and reaction force in the bone pulls the tissue proximally. At the distal end of the nail, the tissue is pulled away, generating tension and preventing the capillaries from collapsing, resulting in reddening. However the tension pulls the nail down on top of the bone, generating a whitening zone between the nail and bone. When force is applied in the negative direction, as shown in the top diagrams, the tissue is bunched up at the distal end of the nail due to the shear and compressed due to normal force.

4.3. Lumped-Parameter Dynamic Model

4.3.1. Hemodynamic Model

The bone-nail interaction model in the previous section explains in a qualitative manner the mechanism by which fingertip forces and posture affect the coloration or blood volume under the fingernail. While the mechanism varies for different types of forces and postures, the common denominators are the principles of reddening and whitening. In this section, the goal is to quantitatively model and simulate the dynamics of the reddening and whitening phenomena.

Based on the anatomical behavior described earlier, a lumped-parameter, hemodynamic model that captures both reddening and whitening phenomena will be formed in this section. Three major components are needed for elucidating the hemodynamic behavior: *a)* capillaries where the visible blood volume changes occur, *b)* arterial supply and venous return, and *c)* a mechanism that varies fluidic resistance and capacitance in response to pressures applied at the fingertip.

a) Capillaries

There are two distinct zones of capillaries: the proximal reddening zone capillaries that are protected by the nail-bone structure, and the distal whitening zone capillaries that are susceptible to collapse by applied pressure. The capillary network must be lumped to create two separate capacitive elements in the model, corresponding to these two zones. Figure 70 shows

the schematic of the lumped-parameter model containing two capacitances representing the lumped capillaries of the reddening and whitening zones.

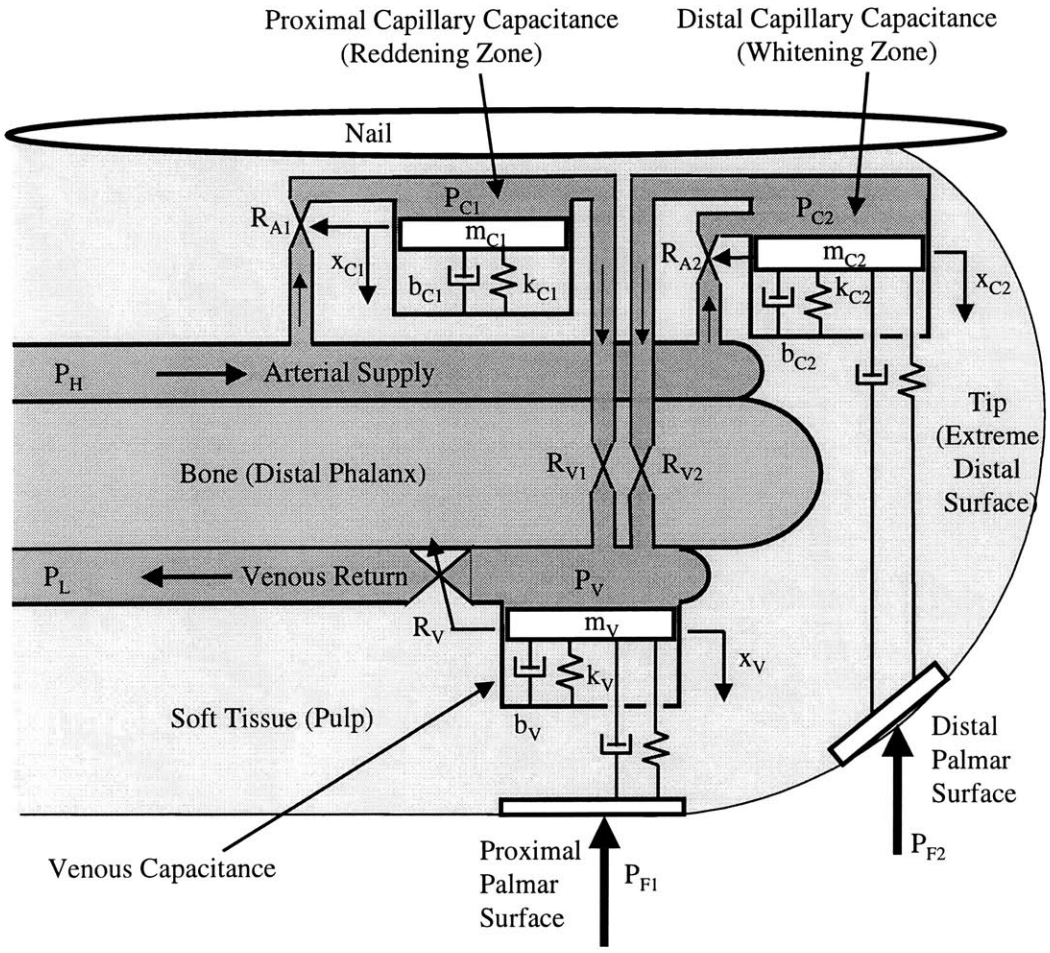

Figure 70: Hemodynamic Model of the Fingertip

Blood flows from a lumped arterial supply, through parallel lumped capillary elements, and out through a lumped venous return. Forces applied to the fingerpad will compress the venous element or the distal capillary element, modulating the fluidic resistances, which further alters the pressures and flows.

b) Arterial Supply and Venous Return

It is known that the fluidic resistance of the capillaries is an order of magnitude higher than that of the digital arteries and veins (Guyton, 1981). Therefore, the pressure drop along the arterial supply and venous return is negligible, and hence all the arteries and veins can be lumped into single flows from which the capillaries branch out in parallel, as shown in Figure 70. Unlike the arteries, the veins are not protected by the bone, so the venous return is modeled with a capacitive element while the arterial supply is not.

c) Variation of Fluidic Resistance and Capacitance

The fluidic resistances and capacitances of the capillaries and veins vary in response to the pressures applied to the finger. As shown in Figure 70, the venous wall is modeled as a mass-spring-damper system with parameters m_V, k_V, and b_V, respectively. Likewise, the capillary walls are modeled as mass-spring-damper systems with parameters m_{C1}, m_{C2}, k_{C1}, k_{C2}, b_{C1}, and b_{C2}. The walls deviate from their effective nominal diameters D_V, D_{C1}, and D_{C2} by the displacements x_V, x_{C1}, and x_{C2}. When pressure P_{F1} acts on the proximal palmar surface of the fingertip, the wall displacement, x_V, becomes increasingly negative. As the effective venous diameter, D_V+x_V, is thus reduced, the fluidic resistance of the venous return, R_V, increases. This causes the pressures in the capillary elements, P_{C1} and P_{C2}, to increase, which then increases the displacements of the capillary walls, x_{C1} and x_{C2}, as shown in Figure 71. As the effective diameters $D_{C1}+x_{C1}$ and $D_{C2}+x_{C2}$ thus increase, more blood is stored in the capillaries, resulting in the reddening effect. Changes in x_{C1} and x_{C2} also modulate the fluidic resistances in the capillary elements, R_{A1} and R_{A2}, which further magnifies the reddening effect.

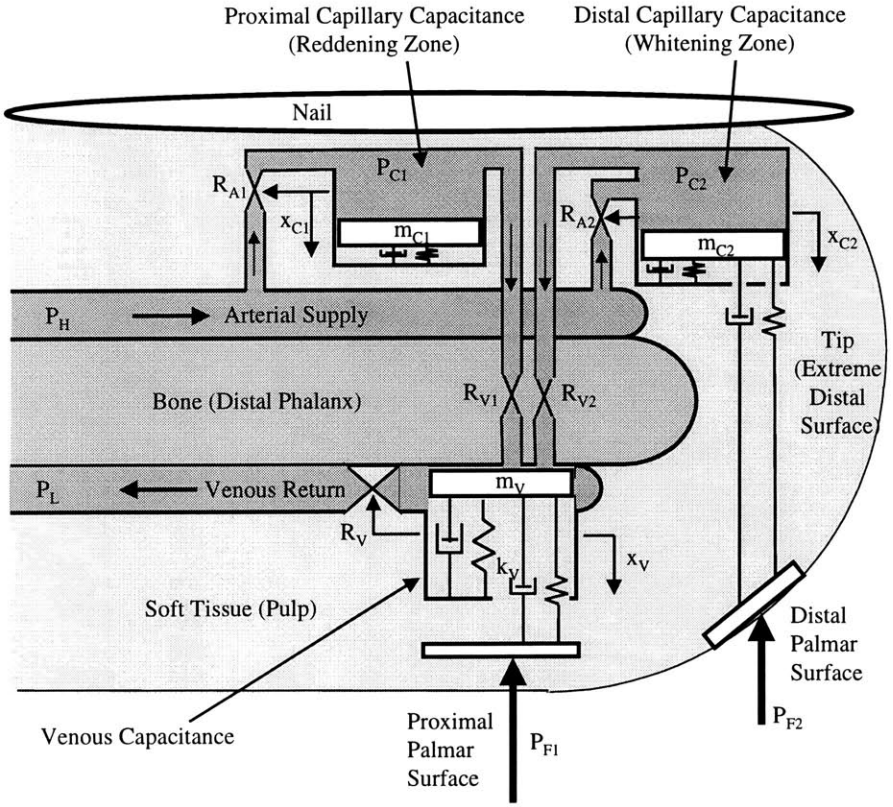

Figure 71: Hemodynamic Model with Proximal Pressure
Force applied at the proximal palmar surface causes the venous element to collapse. Pressure increases in the capillary elements, causing them to swell.

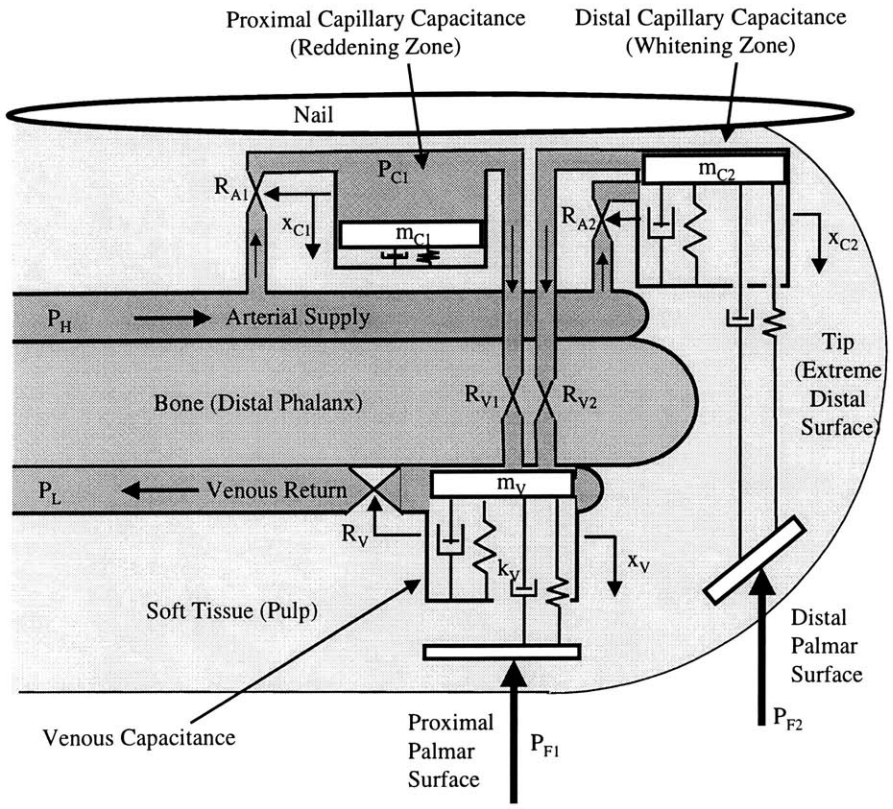

Figure 72: Hemodynamic Model with Proximal and Distal Pressure
Force applied to the distal palmar surface directly collapses the distal capillary element.

Behavior of the distal capillary capacitance at the whitening zone, however, differs from the proximal one when pressure P_{F2} acts on the distal palmar surface of the fingertip. Since the bone does not extend all the way to the tip of the finger, pressure P_{F2} directly propagates through the tissue at the fingertip, resulting in a decrease in the displacement of the distal capillary wall, x_{C2}, as shown in Figure 72. In consequence, the effective diameter $D_{C2}+x_{C2}$ is reduced and blood is removed from the distal capillary capacitance, causing the whitening effect.

At this stage a few assumptions underpinning the above hemodynamic model will be made:

1. The soft tissue (pulp) of the finger can be treated as a virtually fluidic medium to the extent that external pressure on the fingertip is propagated directly to the veins and to the capillaries at the front of the nail. Such "waterbed" models have been used in the past to model the fingertip (Srinivasan, 1989).

2. The bone and nail bed matrix effectively shield the arterial supply and capillaries under the rear portion of the nail from the direct influence of touch forces (see Figure 41 and Figure 42).

3. The effects of shear forces and finger bending are neglected.

The model can eventually be expanded to include more than two capillary units, depending on the hemodynamic behavior of interest and the number of photodetectors that are to be placed on the nail. The number of locations where input forces are applied can also be expanded, given a more thorough treatment of the tissue mechanics.

Figure 73 shows a block diagram representation of the fingernail and sensor system that highlights the inputs and outputs, and the interactions between the hemodynamics and vessel wall dynamics. They not only interact through the fluidic pressures and flows at the capillary and venous walls, but also through the modulation of the fluidic resistances by the capillary and venous diameters, as shown by the feedback loop in the figure. It is this nonlinear effect of the modulation that is responsible for the reddening phenomenon. The primary inputs to the system are touch pressures, P_{F1} and P_{F2}, while the outputs are the light intensities detected by the photodetectors. Blood pressures P_H and P_L act on the system as secondary inputs or disturbances.

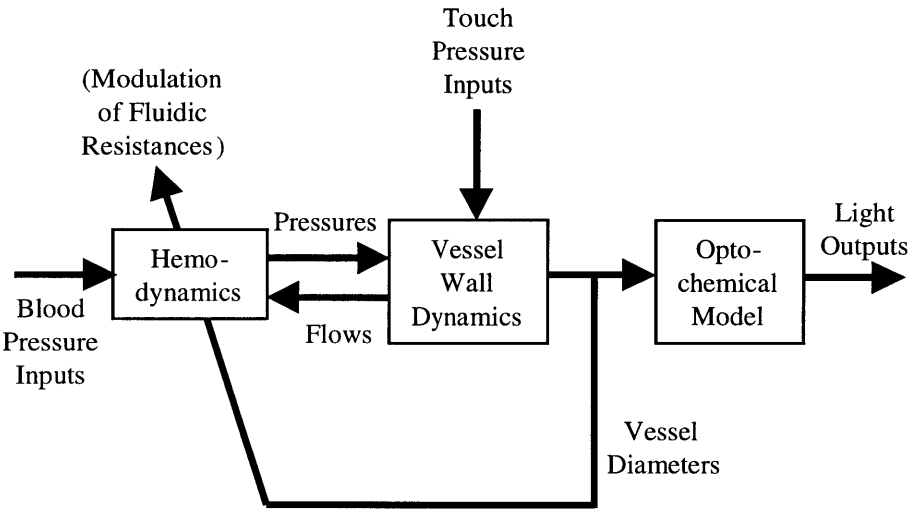

Figure 73: Model Interactions
The hemodynamics and wall dynamics of the blood vessels interact dynamically, sharing pressures and flows while the vessel diameters modulate the fluidic resistances.

Figure 74 shows a Bond Graph representation (Karnopp, et al., 2000) of the hemodynamic model, which also highlights the subsystems of the model and their interactions. There are direct power bonds between each vessel wall subsystem and the blood flow subsystem. The dotted lines show that in addition, the resistances in the blood flow subsystem are modulated

by the displacements in the vessel wall subsystems. State equations for the system can be efficiently derived from this bond graph model once the constitutive relations for resistances and capacitances are derived.

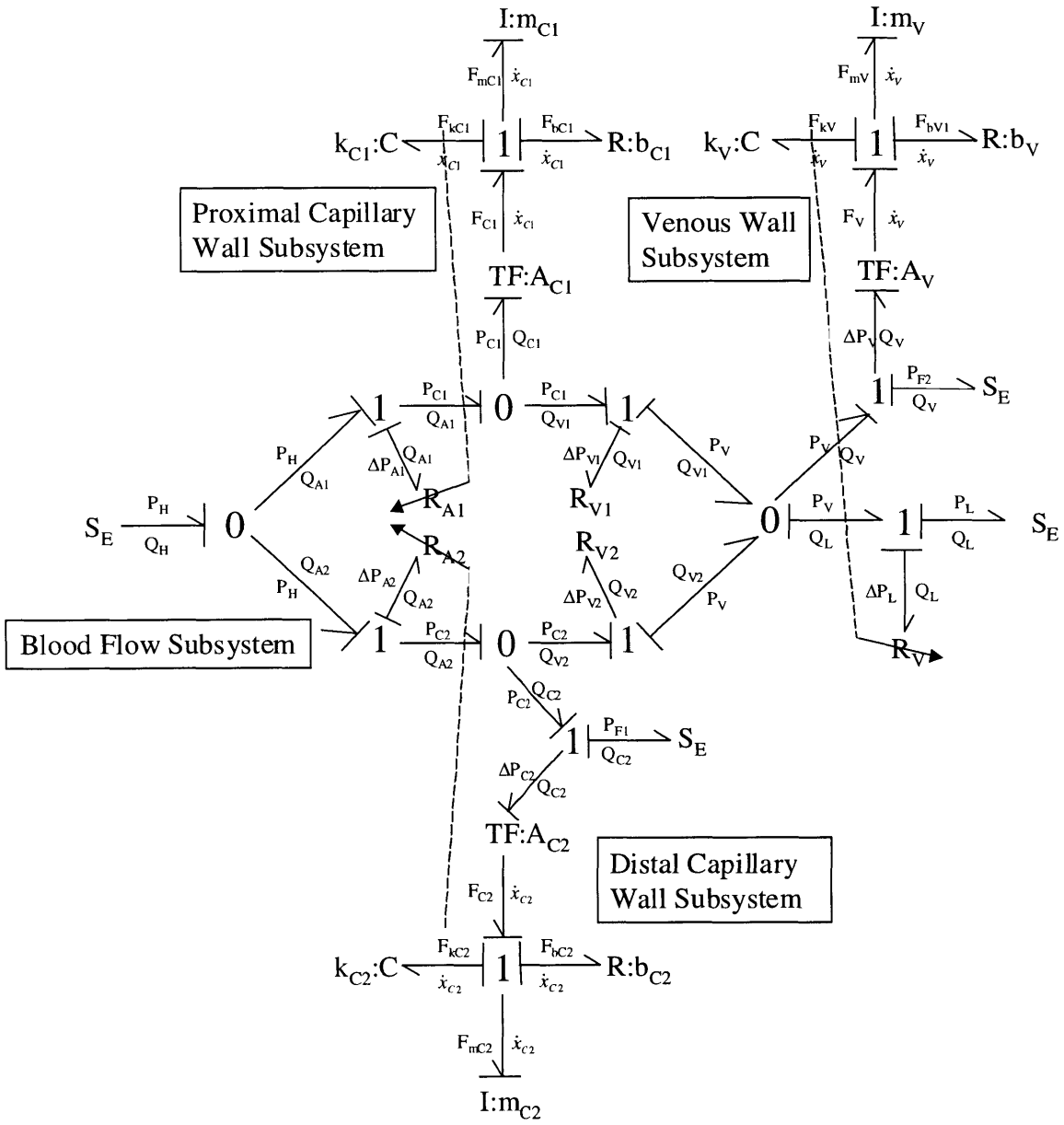

Figure 74: Bond Graph of Hemodynamic Model

The bond graph model highlights the interactions between the blood flow and vessel wall subsystems, including power exchange via pressures and flows as well as the nonlinear effects of the modulation of the fluidic resistances.

4.3.2. State Equations and Output Function

In this section, dynamic state equations and output function will be derived for the hemodynamic network model obtained above. Simple constitutive laws will be assumed for the

elements involved in the lumped-parameter model. The system contains six elements that store energy independently; these are the blood vessel capacitances, k_{C1}, k_{C2}, and k_V, and the masses of the blood vessel walls and blood, m_{C1}, m_{C2}, and m_V. The state variables that are used for locating the dynamic state of the system are the effective displacements of the capillary and venous walls, x_{C1}, x_{C2}, and x_V, and their time rates of change. Therefore a total of six state variables are needed:

$$\mathbf{x} = \begin{bmatrix} x_{C1} & x_{C2} & x_V & \dot{x}_{C1} & \dot{x}_{C2} & \dot{x}_V \end{bmatrix}^T$$

As shown in Figure 73, the inputs to the system consist of the upstream and downstream blood and the external touch pressures applied to the fingertip:

$$\mathbf{u} = \begin{bmatrix} P_H & P_L & P_{F1} & P_{F2} \end{bmatrix}^T$$

The flow in the fingertip is of low Reynold's number. Therefore the fluidic resistances can be modeled using laminar pipe flow (Guyton, 1981). The lumped capillary and venous resistances are given by:

$$R_{A1}(\mathbf{x}) = \frac{128 L_{C1} \mu_{Blood}}{N_{C1} \pi (D_{C1} + x_{C1})^4}, \quad R_{A2}(\mathbf{x}) = \frac{128 L_{C2} \mu_{Blood}}{N_{C2} \pi (D_{C2} + x_{C2})^4}$$

$$R_V(\mathbf{x}) = \frac{128 L_V \mu_{Blood}}{N_V \pi (D_V + x_V)^4} \tag{1}$$

Note that the resistances are functions of the state variables, x_{C1}, x_{C2}, and x_V, and are hence modulated by the blood vessel diameters. These are prominent nonlinearities characteristic to the fingernail sensor system. Furthermore, the stiffness and damping characteristics of blood vessels are generally nonlinear. To analyze pulsation of hemodynamic behavior, this nonlinearity must be taken into account. The nail sensor dynamics, however, are not heavily dependent on the pulsatile dynamics, since the DC components of the photodetector outputs are used rather than the AC components. Therefore, in this work, linear compliance and damping are used for the blood vessels.

In reality, blood flow in the capillaries is characteristically intermittent due to a phenomenon called vasomotion (Guyton, 1981), which refers to the intermittent contraction of the metarterioles and precapillary sphincters that occurs approximately 5-10 times/minute. However, so many capillaries are present in the tissues that their overall function becomes

averaged. The average pressure of the capillaries depends on the arteriolar constriction, the venous pressure, position of the hand, and temperature (Thomine, 1981). It might be more appropriate to model each capillary as an on/off switch, with the percentage of capillaries open at any given time as a function of the pressure. However, the nature of this function (most likely nonlinear) would be unknown. Equation 1 could even be equivalent to such a model where the percentage of capillaries open is given by a fourth order function of the pressure. In fact, even when the percentage of capillaries open is replaced by a first order function of the pressure, the simulation results that follow are not significantly different.

The state equations are therefore given by:

$$\dot{\mathbf{x}} = \mathbf{A}(\mathbf{x})\,\mathbf{x} + \mathbf{B}(\mathbf{x})\,\mathbf{u} \tag{2}$$

where:

$$\mathbf{A}(\mathbf{x}) = \begin{bmatrix} 0 & 0 & 0 & 1 & 0 & 0 \\ 0 & 0 & 0 & 0 & 1 & 0 \\ 0 & 0 & 0 & 0 & 0 & 1 \\ -\frac{k_{C1}}{m_{C1}} & 0 & 0 & -\frac{R_{11}(\mathbf{x})}{m_{C1}} & -\frac{R_{12}(\mathbf{x})}{m_{C1}} & -\frac{R_{13}(\mathbf{x})}{m_{C1}} \\ 0 & -\frac{k_{C2}}{m_{C2}} & 0 & -\frac{R_{12}(\mathbf{x})}{m_{C2}} & -\frac{R_{22}(\mathbf{x})}{m_{C2}} & -\frac{R_{23}(\mathbf{x})}{m_{C2}} \\ 0 & 0 & -\frac{k_V}{m_V} & -\frac{R_{13}(\mathbf{x})}{m_V} & -\frac{R_{23}(\mathbf{x})}{m_V} & -\frac{R_{33}(\mathbf{x})}{m_V} \end{bmatrix}$$

$$\mathbf{B}(\mathbf{x}) = \begin{bmatrix} 0 & 0 & 0 & 0 \\ 0 & 0 & 0 & 0 \\ 0 & 0 & 0 & 0 \\ B_{41}(\mathbf{x}) & B_{42}(\mathbf{x}) & 0 & 0 \\ B_{51}(\mathbf{x}) & B_{52}(\mathbf{x}) & 0 & -\frac{A_{C2}}{m_{C2}} \\ B_{61}(\mathbf{x}) & B_{62}(\mathbf{x}) & -\frac{A_V}{m_V} & 0 \end{bmatrix}$$

$$R_{11}(\mathbf{x}) = b_{C1} + A_{C1}^2 R_{A1}(\mathbf{x})\left(1 - \frac{R_{A1}(\mathbf{x})[R_{A2}(\mathbf{x}) + R_{V2} + R_V(\mathbf{x})]}{R_V(\mathbf{x})\,R_{Total}(\mathbf{x})}\right)$$

$$R_{22}(\mathbf{x}) = b_{C2} + A_{C2}^2 R_{A2}(\mathbf{x})\left(1 - \frac{R_{A2}(\mathbf{x})[R_{A1}(\mathbf{x}) + R_{V1} + R_V(\mathbf{x})]}{R_V(\mathbf{x})R_{Total}(\mathbf{x})}\right)$$

$$R_{33}(\mathbf{x}) = b_V + \frac{A_V^2[R_{A1}(\mathbf{x}) + R_{V1}][R_{A2}(\mathbf{x}) + R_{V2}]}{R_{Total}(\mathbf{x})}$$

$$R_{12}(\mathbf{x}) = \frac{A_{C1}A_{C2}R_{A1}(\mathbf{x})R_{A2}(\mathbf{x})}{R_{Total}(\mathbf{x})}$$

$$R_{13}(\mathbf{x}) = \frac{A_{C1} A_V R_{A1}(\mathbf{x})[R_{A2}(\mathbf{x}) + R_{V2}]}{R_{Total}(\mathbf{x})}$$

$$R_{23}(\mathbf{x}) = \frac{A_{C2} A_V R_{A2}(\mathbf{x})[R_{A1}(\mathbf{x}) + R_{V1}]}{R_{Total}(\mathbf{x})}$$

$$B_{41}(\mathbf{x}) = \frac{A_{C1}}{m_{C1}}\left(1 - \frac{R_{A1}(\mathbf{x})[R_{A2}(\mathbf{x}) + R_{V2}]}{R_V(\mathbf{x}) R_{Total}(\mathbf{x})}\right)$$

$$B_{42}(\mathbf{x}) = \frac{A_{C1} R_{A1}(\mathbf{x})[R_{A2}(\mathbf{x}) + R_{V2}]}{m_{C1} R_V(\mathbf{x}) R_{Total}(\mathbf{x})}$$

$$B_{51}(\mathbf{x}) = \frac{A_{C2}}{m_{C2}}\left(1 - \frac{R_{A2}(\mathbf{x})[R_{A1}(\mathbf{x}) + R_{V1}]}{R_V(\mathbf{x}) R_{Total}(\mathbf{x})}\right)$$

$$B_{52}(\mathbf{x}) = \frac{A_{C2} R_{A2}(\mathbf{x})[R_{A1}(\mathbf{x}) + R_{V1}]}{m_{C2} R_V(\mathbf{x}) R_{Total}(\mathbf{x})}$$

$$B_{61}(\mathbf{x}) = \frac{A_V(\mathbf{x})[R_{A1}(\mathbf{x}) + R_{A2}(\mathbf{x}) + R_{V1} + R_{V2}]}{m_V R_{Total}(\mathbf{x})}$$

$$B_{62}(\mathbf{x}) = \frac{A_V(\mathbf{x})[R_{A1}(\mathbf{x}) + R_{V1}][R_{A2}(\mathbf{x}) + R_{V2}]}{m_V R_V(\mathbf{x}) R_{Total}(\mathbf{x})}$$

$$R_{Total}(\mathbf{x}) = R_{A1}(\mathbf{x}) + R_{A2}(\mathbf{x}) + R_{V1} + R_{V2} + \frac{[R_{A1}(\mathbf{x}) + R_{V1}][R_{A2}(\mathbf{x}) + R_{V2}]}{R_V(\mathbf{x})}$$

All of the model parameters are listed below and their values are estimated to order of magnitude based on physiology literature (Baran and Dawber, 1994; Smith et al., 1991, 1 and 2; Guyton, 1981; Bollinger, et al., 1974; Coffman and Cohen, 1971; Foucher, 1991; Maricq, 1963; Richardson, 1982) and on observable behavior.

- $K_{C1} = K_{C2}$ = capillary wall stiffness ~ 10^5 N/m
- K_V = venous wall stiffness ~ 10^3 N/m
- $m_{C1} = m_{C2}$ = capillary wall and blood inertia ~ 10^{-3} kg
- m_V = venous wall and blood inertia ~ 10^{-3} kg
- $b_{C1} = b_{C2}$ = capillary wall damping ~ 10^4 N-s/m
- b_V = venous wall damping ~ 10^2 N-s/m
- $A_{C1} = A_{C2}$ = capillary surface area ~ 10^{-4} m^2
- A_V = venous surface area ~ 10^{-4} m^2
- $D_{C1} = D_{C2}$ = nominal capillary diameter ~ 10^{-5} m
- D_V = nominal venous diameter ~ 10^{-4} m
- $L_{C1} = L_{C2}$ = capillary length ~ 10^{-3} m
- L_V = venous length ~ 10^{-2} m
- $N_{C1} = N_{C2}$ = number of capillaries ~ 10^5
- N_V = number of small veins ~ 10^2
- μ_{Blood} = blood viscosity ~ 3×10^{-3} Pa-s
- $R_{V1} = R_{V2}$ = lumped venule resistance ~ 10^{11} Pa-s/m^3

- P_H = upstream blood pressure ~ 10^4 Pa (gage)
- P_L = downstream blood pressure = 0 Pa (gage)

Finally, the optical portion of the model should be included as an output function relating the diameters of the capillary elements to the output of the photodetectors. For transmission of light through a solution, the Beer-Lambert Law can be applied, as shown by equation (3):

$$I_{out} = I_{in} e^{-A}$$
$$A = LC\varepsilon \tag{3}$$

where:

I_{out} = output light intensity
I_{in} = input light intensity
A = absorption
L = path length
C = concentration of absorbing substance
ε = absorption coefficient = $\varepsilon(\lambda)$, where λ = wavelength

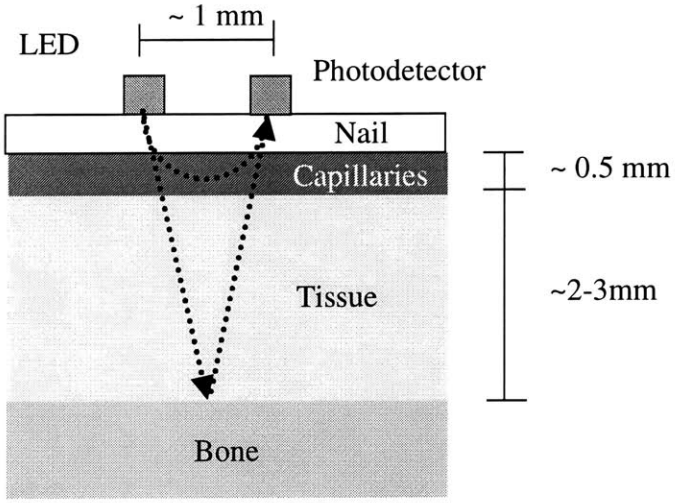

Figure 75: Optical Model
This rough model can be used to estimate an upper bound on the path length of the light through the capillaries. At most, the path length, L, through the capillary region is ~ 1 mm.

In the case of blood, corrections are often made for scattering effects (Steinke and Shepherd, 1986). However, in the case of capillaries, scattering is negligible, since the number of layers of blood cells is few in each capillary (Guyton, 1981). Furthermore, it can be assumed that the capillaries are small and evenly distributed, such that the nail bed can be treated as a continuum having a uniform blood concentration (Van Gemert, et al. 1989), as shown in Figure

75. These conditions allow us to apply the simple Beer-Lambert law to the fingernail. Since the output voltage of the photodiode circuit shown in Figure 14 is directly proportional to the incident light intensity, equation (3) can be rewritten as:

$$V_P = V_0 + V_1 e^{-LC\varepsilon} \tag{4}$$

where V_P is the photodetector output, V_0 is a bias voltage and V_1 is a proportionality constant. V_0 is due to the light directly reflected back to the photodiode from the surface of the nail without passing through the capillaries of the nail bed, and V_1 depends on the photodiode sensitivity, LED brightness, tissue absorbance, and various optical losses. The blood concentration C in the above equation can be expressed as the ratio of the blood volume in the capillaries to the tissue volume:

$$C = \frac{V_{Blood}}{V_{Tissue}} = \frac{N_C L_C \pi (D_C + x_C)^2}{4V_{Tissue}} \tag{5}$$

Applying the above to each of the reddening and whitening zones and substituting it into equation (4) yields the output voltage of each photodiode:

$$V_{Pi} = V_{0i} + V_{1i} e^{-\alpha_i (D_{Ci} + x_{Ci})^2}, \quad i = 1,2 \tag{6}$$

$$\alpha_i = \frac{\pi \varepsilon L_i N_{Ci} L_{Ci}}{4V_{Tissue,i}} \tag{7}$$

By estimating the values of the constants in α to order of magnitude, it is possible to further simplify the optical model. N_C and L_C, the number and length of capillaries, are already estimated above from medical literature. The volume of capillary tissue can be estimated as $V_{Tissue} \sim (10^{-2}\ m)(10^{-2}\ m)(10^{-3}\ m) = 10^{-7}\ m^3$. The absorption coefficient is $\varepsilon = 460 m^{-1}$ from the literature (Takatani and Graham, 1987) for the isobestic wavelength. As shown by Figure 75, we can estimate the path length L to be ~ 1 mm, irrespective of the exact trajectory that the reflected light takes. Thus, the product of α and $(D_C + x_C)^2$ is on the order of 10^{-2}. Taking the first two terms of the Taylor expansion of the exponential, equation (6) reduces to:

$$V_{Pi} = V'_{0i} - V'_{1i} (D_{Ci} + x_{Ci})^2 \tag{8}$$

Thus the output voltage of each photodetector is proportional to the square of the effective diameter of the capillary capacitance beneath it. The output function given by equation (8) can be applied to the states in equation (2) in order to simulate the photodetector response to

various touch inputs. The simulations can then be compared to experimental data to empirically determine V_0' and V_1' for each photodetector.

4.3.3. Simulation

The hemodynamic and optical models derived above are now simulated using the parameter values given in the previous section. First, a step pressure P_{Fl} is applied only at the proximal palmar surface as shown in Figure 70. The responses of the hemodynamic and optical models for a range of equally spaced magnitudes (0.1 N/cm^2) of touch pressure are shown in Figure 76. At time t = 0, the positive step pressure is applied, and then at time t = 2 seconds, the pressure is stepped back to zero. As expected, the touch pressure causes the venous capacitance to contract in diameter and the capillary capacitances to expand in diameter, resulting in the reddening effect described earlier.

The results of the simulation show a characteristically nonlinear behavior. Firstly, the steady state diameters are not linearly proportional to the touch force magnitude. Secondly, the capillary diameters, which are of primary interest, respond much more sluggishly at lower force levels. In fact, the step response back to zero force is much slower than the step response up to a positive force. The venous diameter, on the other hand, responds just as quickly to the negative step as to the positive step. Therefore it is concluded that the asymmetry of the arterial behavior is related to the nonlinearity of the fluid dynamics between the arteries and veins. Specifically, the smaller fluidic resistance at low force slows the system response.

Figure 77 shows the step response of the two photodetectors for simultaneous step inputs at both the proximal and distal palmar surfaces. At time t = 0, a step pressure is applied, and at time t = 2 seconds, it is released. As expected, the output of the proximal photodetector decreases (reddening effect) and the output of the distal photodetector increases (whitening effect). While the output of the proximal photodetector still behaves nonlinearly, the output of the distal photodetector demonstrates a more linear behavior, with approximately equal loading and unloading response times. This indicates that the response of the distal capillary capacitance is dominated by the direct mechanical influence from the touch pressure, rather than by the fluidic interactions.

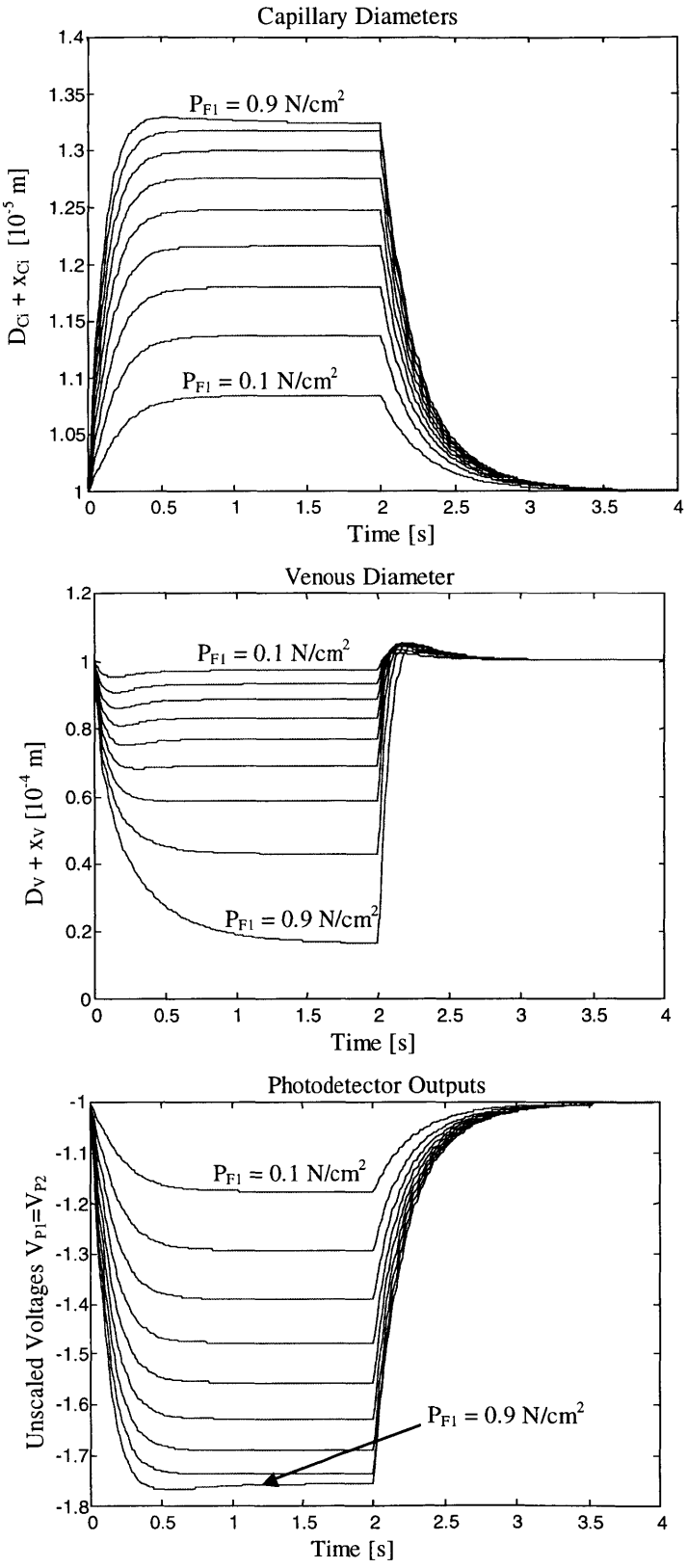

Figure 76: Simulated Dynamic Response to Step in P_{F1}
Increasing pressure at proximal palmar surface causes capillaries to swell.

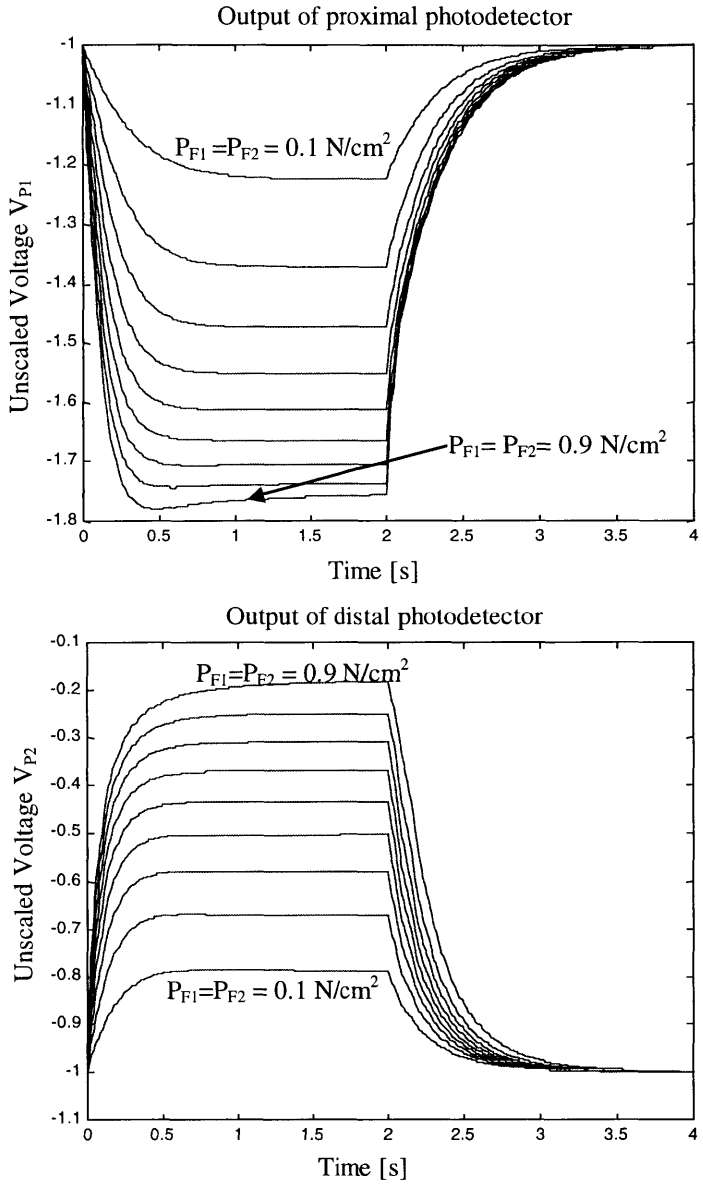

Figure 77: Simulated Dynamic Response to Steps in P_{F1} and P_{F2}
When pressure is increased both proximally and distally, the proximal capillaries swell (reflected light decreases) and the distal capillaries collapse (reflected light increases) as expected.

Figure 78 shows the steady-state relationships between the photodetector outputs and the touch pressure inputs. When touch pressure P_{F1} is applied at the proximal surface, the proximal photodetector voltage V_{P1} decreases roughly linearly and then levels off at approximately 1 N/cm^2 of touch pressure. When touch pressure P_{F2} is applied at the distal surface, the distal photodetector voltage V_{P2} at first increases steeply up to 0.1 N/cm^2, then gradually increases linearly, and finally levels off just beyond 1 N/cm^2.

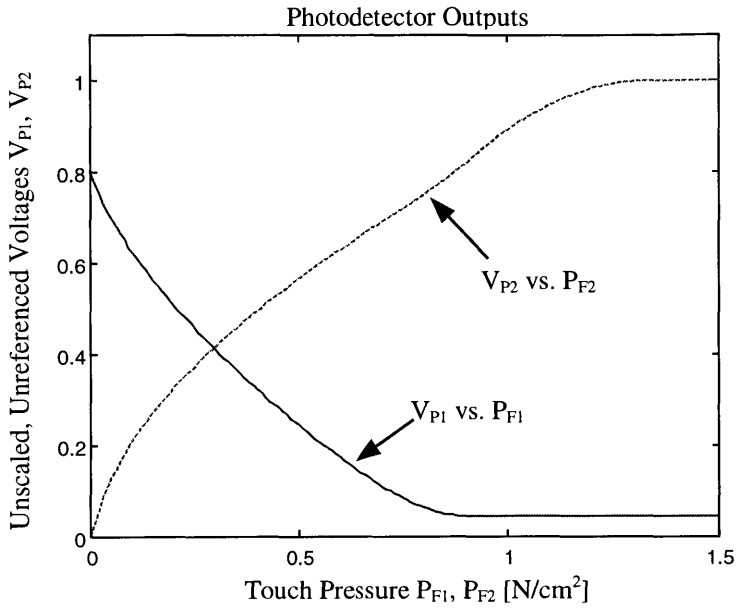

Figure 78: Simulated Static Response to P_{F1} and P_{F2}
Steady state responses from Figure 77 are compiled to show photodiode outputs vs. increases in proximal and distal touch pressures.

4.3.4. Experimental Comparison

In order to test the validity of the model, static and dynamic experiments are performed using the prototype nail sensors. Data is collected for eight human subjects of varying gender and skin color. The subjects are instructed to apply the forces themselves against the force measurement platform described in Chapter 3. As before, the force readings are fed back to the subject using a visual display, allowing the subjects to monitor and control the applied force.

Figure 79 shows the experimental steady-state response of a proximal photodetector to touch force applied normally at the proximal palmar surface of the fingertip. For this experiment, the subject is instructed to slowly cycle the force between 0 and 2 N (~ 20 Hz). The plot shows the average results of three cycles for each subject, and the average of all the subjects. As expected, an approximately linear decrease is observed up to about 1 N, past which the output exhibits a nonlinear leveling off. By tuning the previously unknown offset and scaling parameters in equation (8), the simulated response can be fitted to the experimental average, and is plotted overtop as a dashed line for comparison. The magnitude and range of sensitivity vary across the subjects, but the behavior is similar. Certain subjects show a slight increase in voltage at large force due to encroachment of the whitening zone, an effect not included in the model.

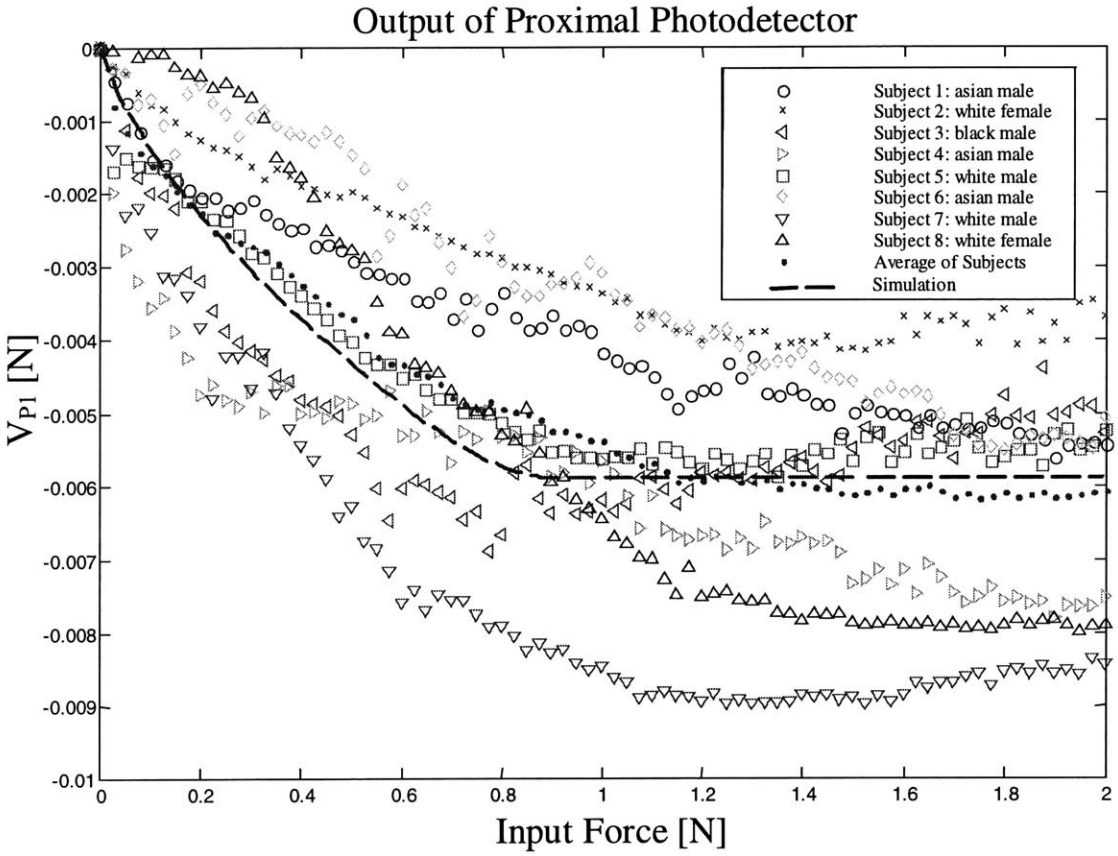

Figure 79: Experimental Static Relationship for Proximal Pressure
Eight human subjects of varying gender and skin color apply a normal force to the fingerpad. As expected, a proximal red zone forms and the output of the proximal photodetector decreases. Sensitivities vary in magnitude between the subjects, but the range of sensitivity and the general behavior is the same.

Figure 80 shows the corresponding dynamic response to proximal touch force for subject 2 (dark skin, static sensitivities close to average) and subject 3 (light skin, static sensitivities far from average). The subjects are instructed to apply a step force as quickly as possible, maintain it, and then release as quickly as possible. Although the sensitivities differ, all eight subjects show time constants that are at least as fast as that of the measured input force (average $\tau_1 = 0.16$ s for loading/0.12 s for unloading). The model time constants are first tuned to match the subjects by adjusting the stiffness and damping parameters of equation (2) within an order of magnitude. The model is then calibrated to each subject by tuning the scaling and offset parameters of equation (8). The model response to the measured forces is simulated and plotted overtop as dashed lines for subjects 2 and 3.

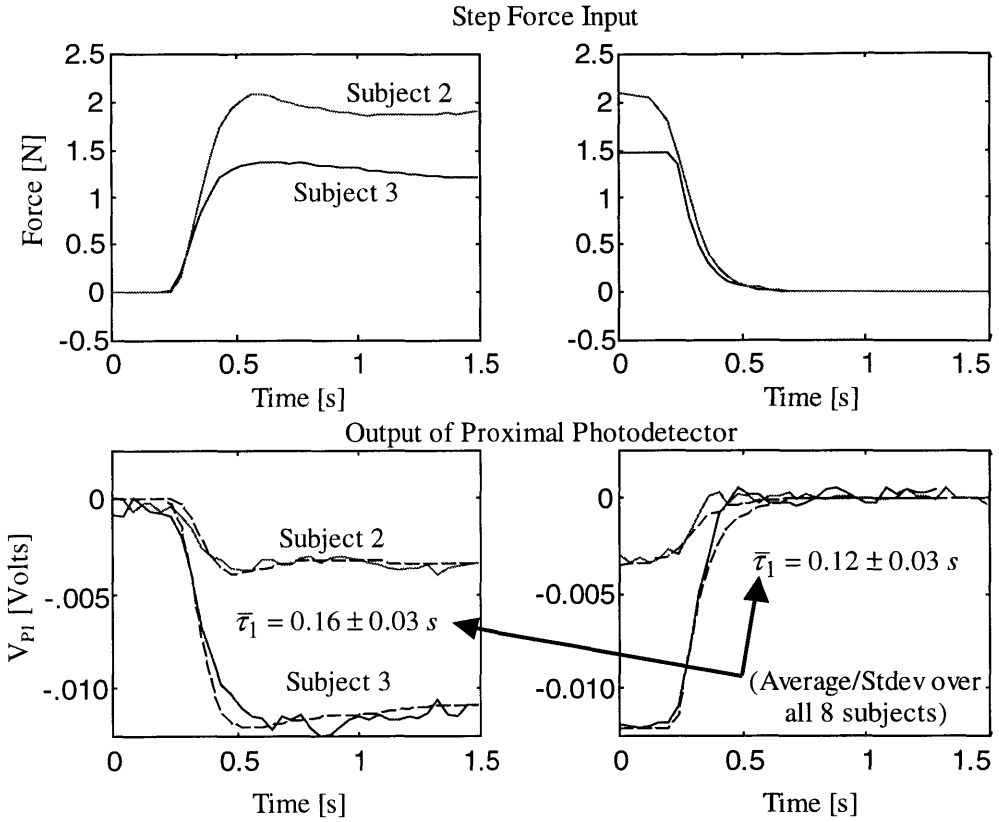

Figure 80: Experimental Dynamic Response to Proximal Pressure
Dynamic experiments for the same eight subjects show that the reddening effect has comparable time constants for both loading and unloading.

Figure 81 shows the experimental steady-state response of a distal photodetector to touch force applied at the distal palmar surface of the fingertip. As expected, an approximately linear behavior is observed up to about 1 N, past which the output exhibits a nonlinear leveling off. In this case, while the magnitude of sensitivity varies across subjects, the range of sensitivity is very consistent. The slightly positive slope beyond 1 N is a result of the widening of the whitening band, an unmodeled effect.

Figure 82 shows the corresponding dynamic response to distal touch force for the same two subjects. As before, the model response is calibrated to the experimental response for each subject and plotted overtop as dashed lines. Compared to proximal touching, the time constants here are noticeably longer (average τ_2 = 0.18 s for loading/0.36 s for unloading). On average, subjects exhibit a much longer time constant for unloading than loading, most likely due to unmodeled creep behavior of the distal finger pulp.

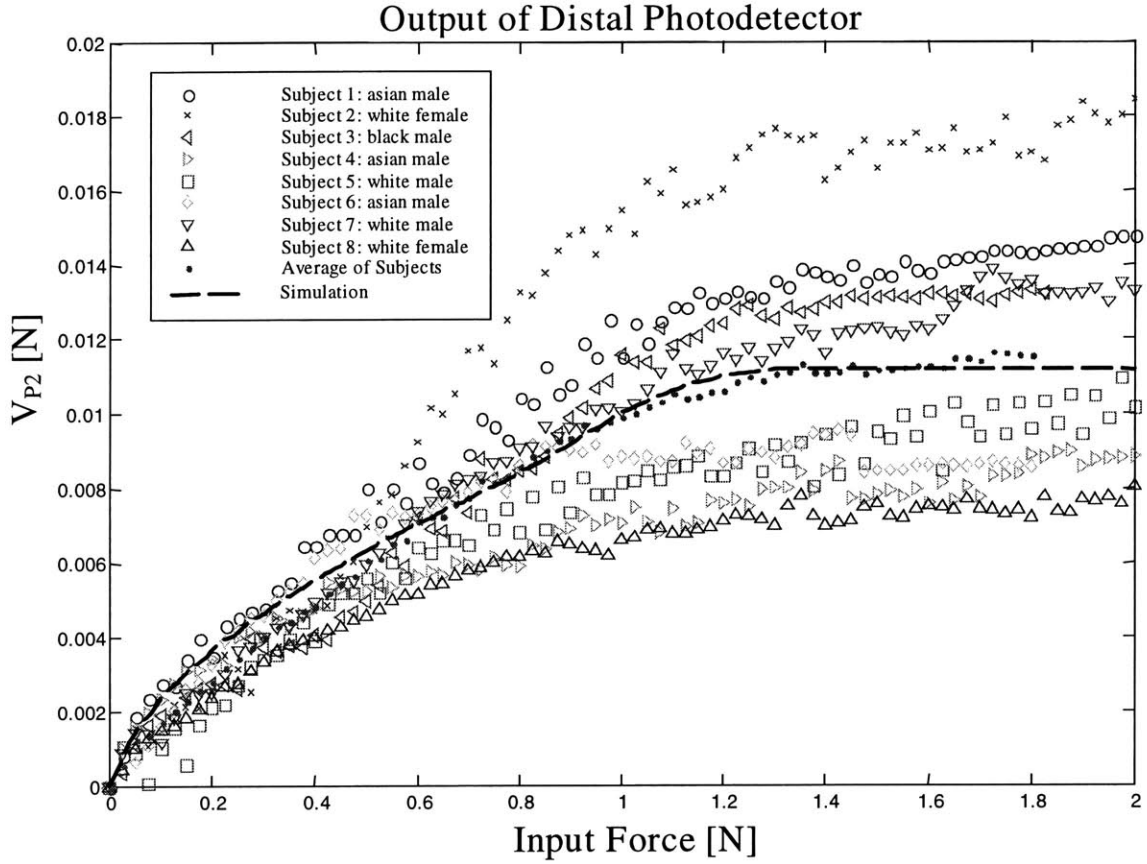

Figure 81: Experimental Static Relationship for Distal Pressure
As expected, the output of the distal photodetector increases with increasing force, corresponding to the distal whitening effect. As before, the sensitivities vary in magnitude between the subjects, but the range of sensitivity and the general behavior are the same.

At this point, the principal limitation in comparing simulations and experiments is that the simulations assume that two distinct, uniformly distributed pressures are applied to the proximal and distal palmar surfaces of the fingertip; whereas in our experiments, a single lumped force is applied and it is not known how the pressure is distributed across the fingertip. However, the comparison does show agreement between experiment and simulation in terms of general static and dynamic behavior.

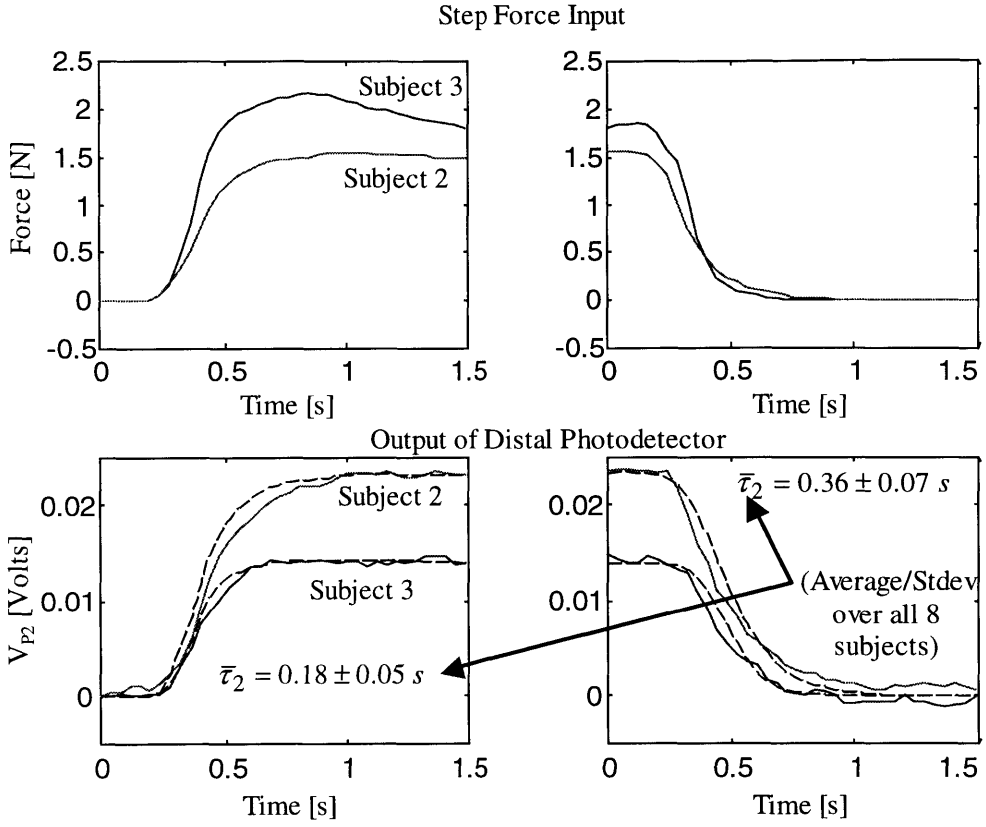

Figure 82: Experimental Dynamic Response to Distal Pressure
Dynamic experiments show that the whitening effect has slower average time constants than the reddening effect, particularly for unloading.

5. PREDICTOR DESIGN AND CALIBRATION

5.1. Black Box Modeling

5.1.1. Introduction

In Chapter 4, a nonlinear, physically-based, dynamic model was created that is capable of relating normal force to photodiode outputs in a physically meaningful way. The bone-nail interaction mechanism could in principle be used to extend this physical model to account for shear forces and bending in addition to normal force; however the effort required to accomplish this is beyond the scope of this thesis. Instead, the goal of Chapter 5 will be to develop a purely mathematical or data-driven "black box" model that can predict the variables of interest, but whose parameters have no known physical meaning. The model will be static, i.e. it will not have any dynamics or time-dependency, but will simply predict the variables of interest as a function of the photodiode outputs.

Several issues must be addressed and dealt with in this chapter in order to design and implement this black box predictor. Section 5.1 will address the issue of how to structure the predictor and model the input-output relationship. Specifically, the difficulty of simultaneously predicting forces and posture will be dealt with, as well as the uncertainty in how to best represent the input-output relationship. Section 5.2 will address the issue of how to calibrate or tune the predictor for multiple users. Specifically, method, constraints, trajectory, and protocol must be designed in order to consistently generate an accurate and properly distributed set of training data. Finally, in Sections 5.3 and 5.4, the performance of the predictor will be analyzed and used to suggest improvements in sensor design.

5.1.2. Modeling Goals

The preliminary experiments conducted in Chapter 3 show that the nail sensor prototype responds with different patterns to changes in normal force, F_z, lateral shear force, F_x, longitudinal shear force, F_y, and bending angle, θ. Recall that the bending angle θ is actually J_2, the angle of the PIP joint, which has been chosen to represent the coupled flexion of the DIP and PIP joints. The goal of this chapter is to design a multi-input, multi-output predictor, as shown in

Figure 83, which receives the eight photodiode signals and outputs predictions of the four variables just mentioned.

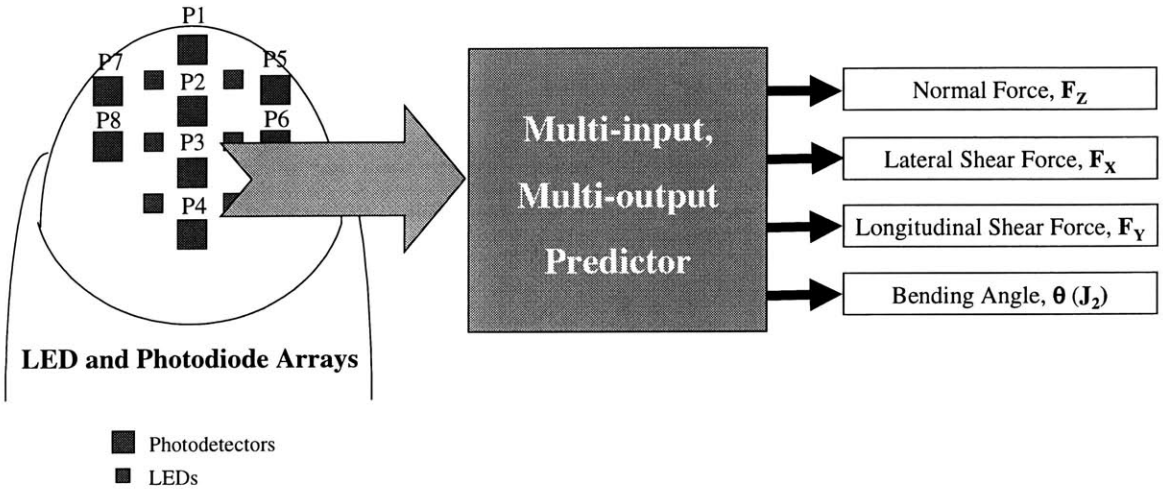

Figure 83: Force and Posture Predictor
The goal is a model that can predict three axes of forces and the bending angle based on the outputs of the eight photodiodes.

Since the model parameters will vary from user to user, the model will be calibrated by experimentally tuning the parameters for each user. To calibrate the model of Figure 83 so that it can predict any combination of touch force and bending angle, all four variables of interest should be simultaneously varied in different combinations while the photodiode outputs are recorded. However, this leads to three major problems:

1. It is extremely difficult to simultaneously vary the three forces and bending angle in a controlled manner.

2. When force is applied to the fingertip, the angles of the DIP and PIP joints are no longer coupled and can vary independently.

3. It is difficult to simultaneously measure the touch force and bending angle, since the force measurement platform and posture tracking system are difficult to physically coordinate.

The solution to these problems is to place a smaller demand on the functionality of the model—i.e. the model should predict either touch or bending but not both simultaneously. To justify this reduced functionality, the application of the sensor must be limited to situations where either touch or bending may occur but not both simultaneously. Indeed, this is just the

functionality required for the wearable mouse application described in Chapter 6, and mentioned in Chapter 3 as an acceptable compromise between the minimum functionality of a virtual switch application and the maximum functionality of a comprehensive skill monitoring application. As far as the device is used as a computer mouse, it is reasonable to assume that the operator will not try to execute simultaneous bending and touching actions. Therefore, it will be assumed that bending and touching are exclusive actions. Specifically, the bend angle will remain constant when force is applied, and the force will remain zero when bending occurs. Furthermore, as before in Chapter 3, we will constrain the contact angles to remain zero during touching by directing the operator to push the fingerpad flat against the surface to maximize the contact area and stability.

By limiting the functionality of the sensor in this manner, a new model is proposed as shown in Figure 84. The photodiode signals are first sent to a touch/bend discriminator, which decides whether touching or bending is occurring, and then passes the photodiode signals to either the touch predictor or the posture predictor. The two predictors can then be calibrated separately.

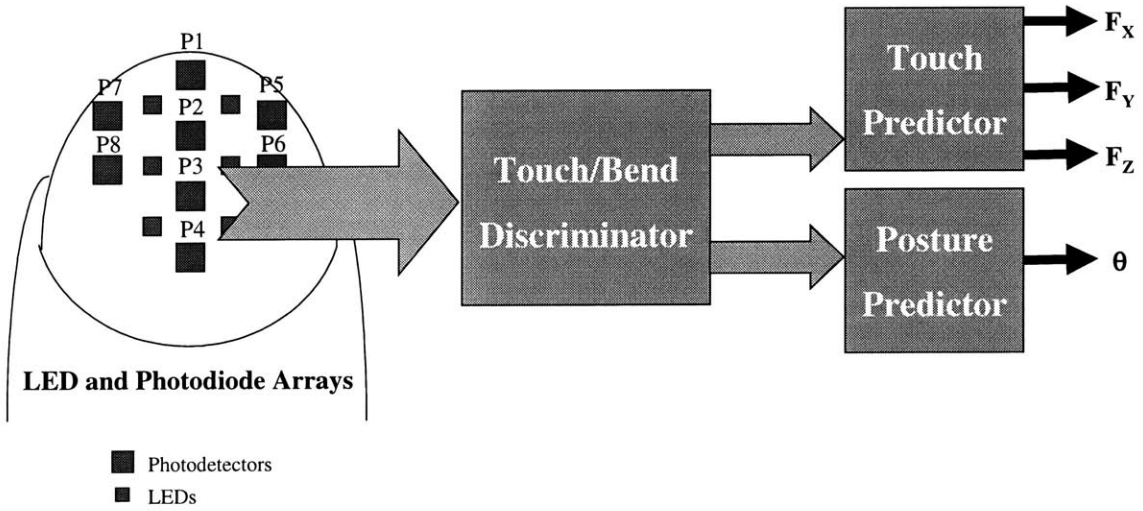

Figure 84: Touch/Bend Discriminator and Predictors
By limiting the functionality of the sensor, the complex model of Figure 83 can be replaced by three simpler models.

To make the model simpler, the functionality of the discriminator can be embedded into the touch predictor itself, as shown in Figure 85. Whenever the touch model predicts normal force below a certain threshold, touching is assumed to be nonexistent and the posture model is

allowed to function. Otherwise, the posture model predicts constant bending angle. In either case, the force predictions are valid. In order for this to work, the touch predictor must be trained to predict zero normal force in the presence of bending. This requirement is feasible and will be addressed in the calibration section of this chapter.

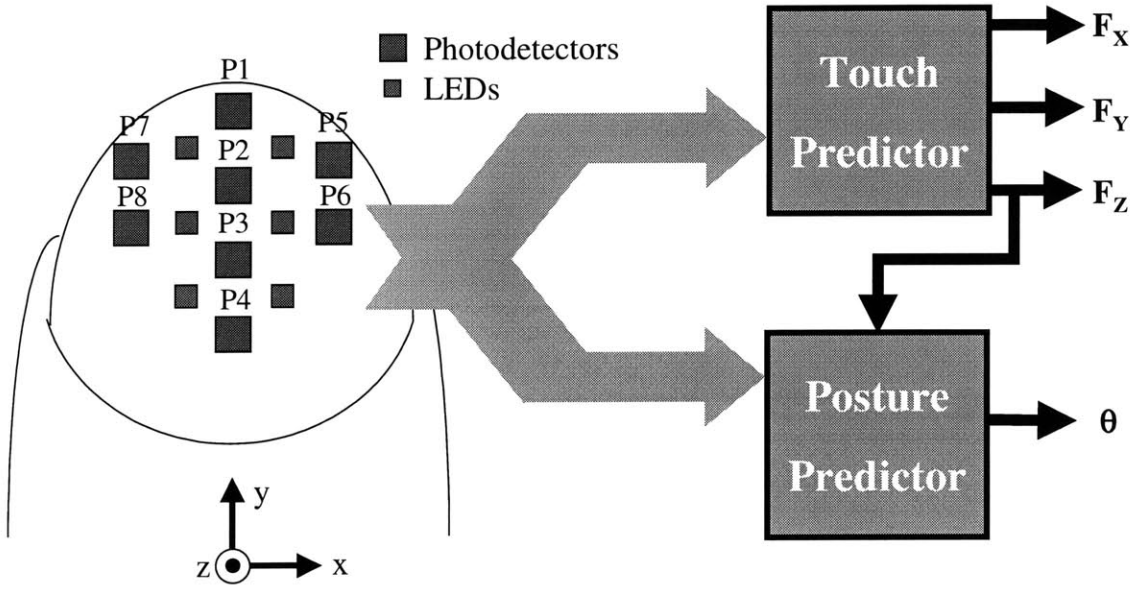

Figure 85: Dual Touch/Posture Predictor
The discriminator of Figure 84 can be eliminated by using the predicted normal force to turn the posture predictor off and on.

Finally, the internal structure of the dual predictors of Figure 85 needs to be addressed. Since the degree of nonlinearity of the real fingertip system is unknown, three types of predictor models will be explored, each having a different degree of nonlinearity.

5.1.3. Linear Model

The simplest model that can be used for the dual predictor is a linear model. Each variable of interest will be a linear combination of the outputs of the eight photodiodes:

$$\hat{\mathbf{F}} = \begin{pmatrix} \hat{F}_x \\ \hat{F}_y \\ \hat{F}_z \end{pmatrix} = \mathbf{J}_F\mathbf{P} + \mathbf{F}_0 \qquad (9)$$

$$\hat{\theta} = \hat{J}_2 = \begin{cases} \mathbf{J}_\theta\mathbf{P} + \theta_0, & \hat{F}_z < F_{\min} \\ \theta_{Touch}, & \hat{F}_z \geq F_{\min} \end{cases}$$

where $\mathbf{P}$ is an 8x1 vector of photodetector outputs, $\hat{\mathbf{F}}$ is a 3x1 vector of force predictions, $\hat{\theta}$ is the bending angle prediction. $\mathbf{J}_F$ and $\mathbf{J}_\theta$ are the 3x8 and 1x8 experimentally determined Jacobian matrices. $\mathbf{F}_0$ and θ_0 are the experimentally determined force and bending offsets, F_{min} is the chosen normal force threshold below which touching is assumed to be nonexistent, and θ_{Touch} is the constant bending angle that is assumed when touching does occur. To determine the Jacobian matrices and offsets, two separate multivariate linear least squares regressions are performed using experimental training data (Johnson and Wichern, 1988). Each regression assumes a model of the form:

$$\mathbf{Y} = \boldsymbol{\beta}\,\mathbf{Z} + \boldsymbol{\varepsilon} \tag{10}$$

where $\mathbf{Z}$ is a matrix of photodiode data, $\mathbf{Y}$ is matrix of force or bending data, and $\boldsymbol{\varepsilon}$ is the residual vector. The least squares solution is given by

$$\boldsymbol{\beta} = \mathbf{Y}\,\mathbf{Z}^T(\mathbf{Z}\mathbf{Z}^T)^{-1} \tag{11}$$

For the touch model, equation (10) becomes

$$\mathbf{Y}_F = \begin{bmatrix}\mathbf{J}_F & \mathbf{F}_0\end{bmatrix}\begin{bmatrix}\mathbf{Z}_P \\ \mathbf{1}\end{bmatrix} + \boldsymbol{\varepsilon}_F \tag{12}$$

where $\mathbf{Z_P}$ is an 8xn matrix of photodiode data, $\mathbf{Y}_F$ is a 3xn matrix of force data, and n is the number of data samples. The Jacobian and offset are given by the least squares solution, where equation (11) becomes

$$\begin{bmatrix}\mathbf{J}_F & \mathbf{F}_0\end{bmatrix} = \mathbf{Y}_F\,\mathbf{Z}_P^{\mathrm{T}}(\mathbf{Z}_P\mathbf{Z}_P^{\mathrm{T}})^{-1} \tag{13}$$

Likewise, for the bending model, Equation 10 becomes

$$\mathbf{Y}_\theta = \begin{bmatrix}\mathbf{J}_\theta & \theta_0\end{bmatrix}\begin{bmatrix}\mathbf{Z}_P \\ \mathbf{1}\end{bmatrix} + \boldsymbol{\varepsilon}_\theta \tag{14}$$

where $\mathbf{Z}_P$ is again an 8xn matrix of photodiode data, $\mathbf{Y}_\theta$ is now a 1xn matrix of bending data, and n is the number of data samples. The Jacobian and offset are again given by the least squares solution, where equation (11) now becomes

$$\begin{bmatrix}\mathbf{J}_\theta & \theta_0\end{bmatrix} = \mathbf{Y}_\theta\,\mathbf{Z}_P^{\mathrm{T}}(\mathbf{Z}_P\mathbf{Z}_P^{\mathrm{T}})^{-1} \tag{15}$$

After computing least squares solutions for both touch and bending, the Jacobians and offsets can then be used in equation (9) to predict forces and bending angle based on new photodiode readings.

5.1.4. Polynomial Model

In order to achieve a model that fits the data more closely, nonlinear regressions could be performed. However, because of the multiple dimensionalities of the data, it is difficult to postulate what type of nonlinear functions might be suitable to fit the data. Since preliminary **P** vs. **F** data in Chapter 3 shows some curvature, it is reasonable to try a polynomial model. The more terms in the polynomial, the better the model can fit the curvature. As a start, we can try a second-degree polynomial model, the most comprehensive of which includes all the squares and cross products of the photodetector readings (Rawlings, 1988). equation (9) can be rewritten as:

$$\hat{\mathbf{F}} = \begin{pmatrix} \hat{F}_x \\ \hat{F}_y \\ \hat{F}_z \end{pmatrix} = \mathbf{J}_F \mathbf{P}_Q + \mathbf{F}_0$$
$$\hat{\theta} = \hat{J}_2 = \begin{cases} \mathbf{J}_\theta \mathbf{P}_Q + \theta_0, & \hat{F}_z < F_{\min} \\ \theta_{Touch}, & \hat{F}_z \geq F_{\min} \end{cases} \tag{16}$$

where $\mathbf{P}_Q$ is the 44x1 vector $[P_1, P_2, \ldots, P_8, P_1^2, P_1P_2, P_1P_3, \ldots, P_1P_8, P_2^2, P_2P_3, \ldots, P_2P_8, \ldots P_8^2]^T$. As before, two separate 3x44 and 1x44 regressions are performed using experimental data for the touching and bending, respectively. The Jacobians and offset matrices are computed as before, except that $\mathbf{Z}_P$ is now a 44xn matrix containing n samples of $\mathbf{P}_Q$.

5.1.5. Neural Network Model

Neural network models can also be used to approximate a variety of nonlinear functions. Figure 86 shows a schematic diagram of a basic three-layer feedforward neural network model (Haykin, 1999; Demuth and Beale, 1994) that can be used to predict the three touch forces based on the eight photodiode signals.

The input layer on the left consists of the eight photodiode signals. The hidden layer consists of a chosen number of nodes, N, where the output of each hidden node is a function

(typically nonlinear, such as ***tansig*** or ***logsig***) of the weighted sum of photodiode signals. For example,

$$\mathbf{H} = \text{tansig}(\mathbf{W}_P\mathbf{P} + \mathbf{b}_H), \qquad \text{tansig}(x) = \frac{2}{1+e^{-2x}} - 1 \tag{17}$$

where $\mathbf{P}$ is the 8x1 vector of photodiode signals, $\mathbf{H}$ is the Nx1 vector out hidden layer outputs, $\mathbf{W}_P$ is an Nx8 matrix of weights, and $\mathbf{b}_H$ is an Nx1 vector of biases.

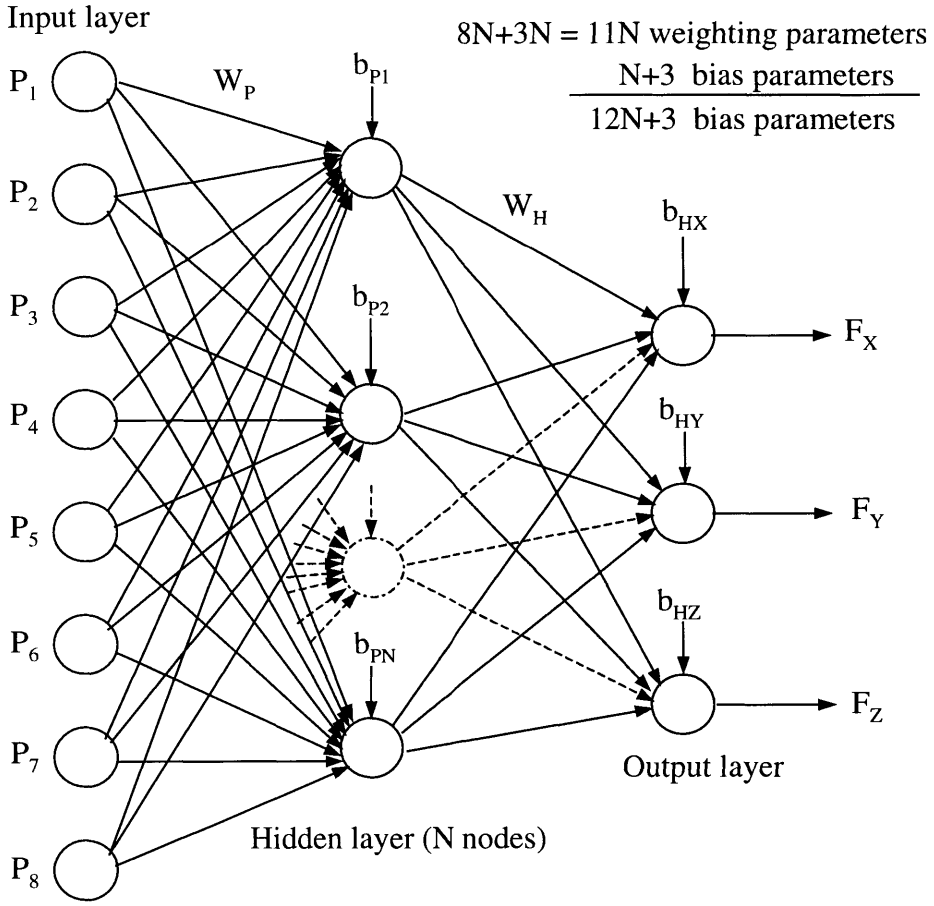

Figure 86: Feedforward Neural Network Model
A three-layered Neural Network can be trained to predict the three forces using the eight photodiode readings.

The output layer then computes the three forces, where each force is a function (typically linear) of the weighted sum of the outputs of the hidden layer. For example,

$$\hat{\mathbf{F}} = \mathbf{W}_H\mathbf{H} + \mathbf{b}_F \tag{18}$$

where $\mathbf{F}$ is the 3x1 vector of force predictions, $\mathbf{W}_H$ is a 3xN matrix of weights, and $\mathbf{b}_F$ is a 3x1 vector of biases. As shown in Figure 86, there are 11N weighting parameters and N+3 bias

parameters, resulting in a total of 12N+3 parameters. A smaller, separate network with only one output node and 10N+1 parameters will be constructed to predict the bending angle.

Each neural network model is "trained" with the Matlab Toolbox (Demuth and Beale, 1994), which uses a backpropagation algorithm where a set of training data (consisting of many samples of photodiode signals and corresponding forces) is repeatedly presented to the network. The predicted forces (or bending angle) are compared to the actual forces (or bending angle) and the errors are propagated backward through the network and used to modify each of the weighting parameters. One epoch of training is defined as a single presentation of the entire set of training data. Typically, several epochs of training are performed. There are a couple of important features of the neural network that must be treated with caution.

a) Number of Hidden Nodes

By increasing the number of nodes in the hidden layer, or the number of hidden layers, the network can become more flexible and better approximate the real nonlinear system. However, with too many nodes, the computation time becomes impractical, more training data is needed, and most importantly, the error actually worsens. In order to find the optimal number of nodes in a single hidden layer, the number of nodes should be iteratively increased as the performance of the training is monitored. After each epoch, the mean squared error (MSE) of the training data is checked. For small number of nodes the MSE will reach a minimum and plateau there as the number of epochs increases. When the number of nodes becomes too many, the MSE will first decrease, but then increase with more and more epochs.

b) Number of Epochs

Even though the MSE of the training data may continue to decrease as the number of training epochs increases, the neural network may become over-trained. The network begins to train itself to the noise in the training data, which is unique to that particular set of training data. As a result, the network does not generalize well and results in large errors when presented with new data that was not part of the training. In order to avoid over-training, a set of validation data is typically used in addition to the set of training data. After each epoch, the MSE of the validation data is checked. When the MSE of the validation data no longer decreases, the training is halted.

5.2. Calibration

5.2.1. Method

In this section, a method will be developed to calibrate the dual force/posture predictor of Figure 85 for each individual user. In order to calibrate the predictor using any of the three types of models (linear, polynomial, neural network), two separate sets of training data are needed: one for the touch predictor and one for the posture predictor. Each training set consists of a number of data samples. For the touch training, a data sample consists of a reading from each of the eight photodiodes and corresponding values of the three touch forces as measured by the force measurement platform. Similarly, for the posture training, a data sample consists of a reading from each of the eight photodiodes and corresponding value of the bending angle as measured by the posture tracking system.

To calibrate the posture predictor, it is a simple matter to generate a set of training data spanning the usable range of finger flexion/extension. However, in order to calibrate the touch predictor to predict any combination of touch forces, the training data should be distributed across the entire usable portion of the three-dimensional force space. Therefore, a means is needed to prompt the user to fully explore this space during the training session. Since it is difficult for a human to apply desired forces simultaneously in three dimensions, the desired forces and the actual forces (measured by the experimental platform) should be visually presented to the user in a maximally intuitive manner. The human can then act as a natural feedback controller to apply the prompted forces. In the past, three-dimensional force information has been visually presented using a pseudo-perspective view with horizontal, vertical, and diagonal bars representing each of the forces (Sheridan, 1992). However this requires the user to track three different positions on the screen at once. Instead, to achieve a more intuitive feedback, the information should be presented in such a way that the user must only track a single position on the screen.

Figure 87 shows a graphic user interface (GUI) programmed in Java that will be used as an intuitive force prompter. Since a two-dimensional screen must be used to display three dimensions of forces, two of the three dimensions of force are represented by position, while the third dimension is represented by color. The small colored circle in the center of the white

display represents the actual force applied. The colored ring represents the desired force generated by the prompter. The goal of the user is to keep the circle within the ring and match the color at the same time, while the prompter moves the ring along a prescribed trajectory. The x-positions of the circle and ring represent lateral shear force, F_x, the y-positions represent longitudinal shear force, F_y, and the colors represent normal force, F_z. The rainbow-colored bar on the right side of the GUI provides an alternate, redundant display of normal force. The vertical position of the triangle represents the desired normal force/color, while the position of the horizontal line represents the actual normal force/color. When the triangle and line are aligned, the colors of the circle and ring will match.

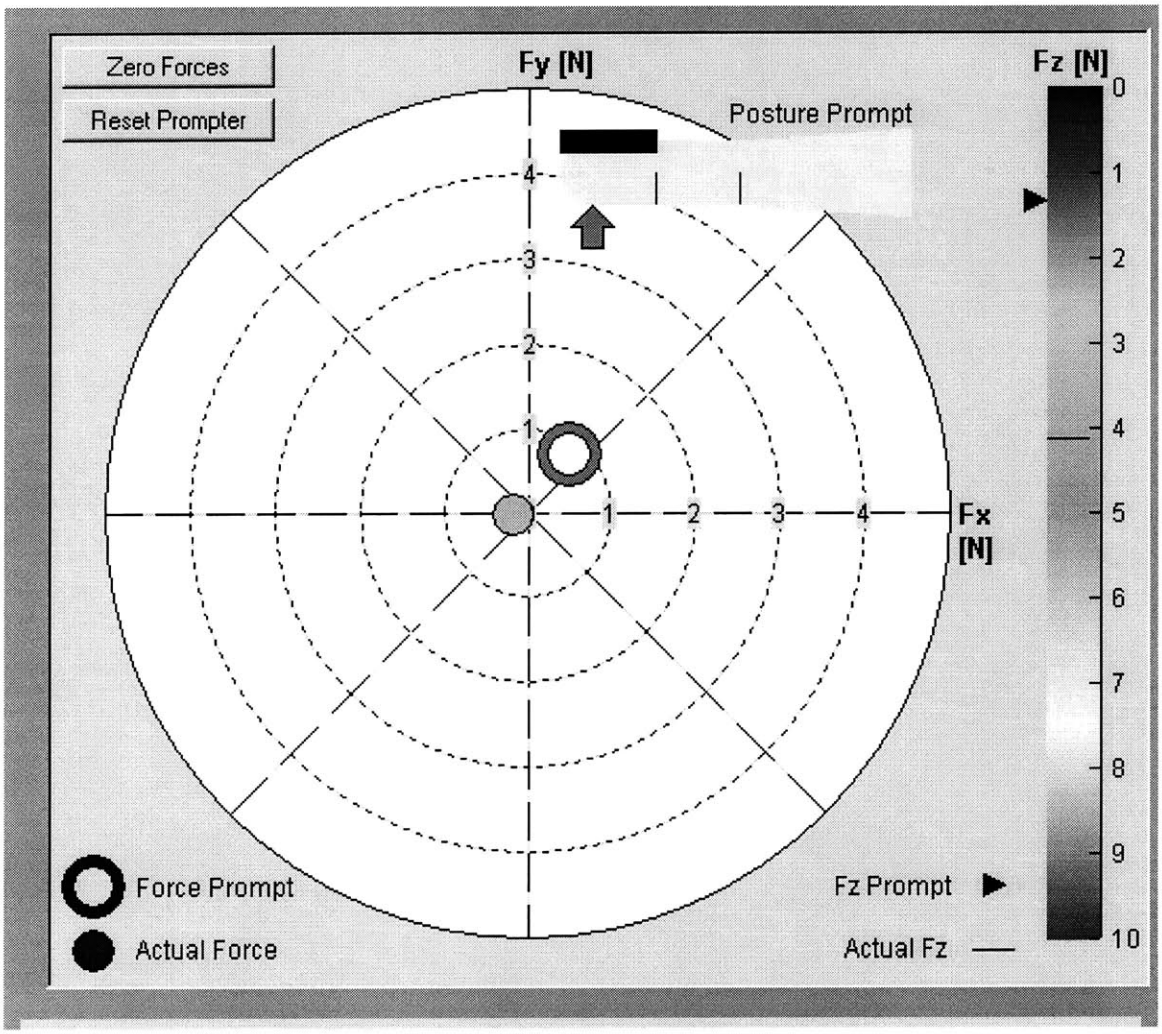

Figure 87: Graphic User Interface for Calibration
The user must keep the circle in the ring and match the color in order to fully explore the 3-dimensional force space during calibration.

In the previous section, it was mentioned that the touch predictor must also be trained to predict zero force in the presence of bending. Therefore, the GUI in Figure 87 also includes a posture prompt in the form of a graphically illustrated finger. After the touch prompting is complete, the user is prompted to bend the finger in synchronization with the finger on the screen, while readings of zero force are registered. The training data for the force predictor then contains a number of samples with zero force, whose photodiode readings correspond to finger bending. The posture prompt can also be used to help generate the training data for the posture predictor. As the user bends the finger in synchronization with the prompt, data from the photodiodes are recorded, and the actual posture is monitored using the video tracking system. Since the actual values of the bending angle are computed offline from the video tracking, they cannot be fed back in real time to the user as part of the GUI. However, the user can visually compare the actual finger posture with that of the prompter.

With both the force prompter and the posture prompter, it is not critical that the actual force/posture is identical to the prompted force/posture. The training data always consists of the actual measured force/posture values. The prompts are only a guide for fully exploring the force space and posture space.

5.2.2. Constraints

Now that the calibration method has been established, the constraints on this method must be addressed. Using the GUI described above, the calibration training data will be collected as the user is prompted to explore the entire usable portion of the 3-D force space and 1-D posture space. Here, the usable portion or range of the force space and posture space will be defined, as well as the speed in which they should be explored.

a) Range of Calibration

The usable portion of the force space is constrained by three factors:

1. The range of forces that a human can comfortably apply and control.
2. The range of sensitivity of the fingernail sensor.
3. The coefficient of friction of the finger against the surface of contact.

A number of references discuss the capability of the human to apply normal forces with the fingertip. As reported in Pawluk and Howe (1999), normal forces in the range of 0 to 2 N are most relevant for examining the response of the fingerpad during grasping (Westling and Johansson, 1987) and are also the typical forces in typing (Martin, et al., 1996). According to Jones (1998), a human is capable of controlling a constant force in the range of 2 to 6 N with average error of 6% using visual feedback in addition to natural haptic sense. However, when shear force is added, the maximum normal force that a human subject can comfortably apply for an extended time (i.e. a few minutes) is about 3 N. The preliminary experiments conducted in Chapter 3 indicate that this is within the range of sensitivity of the fingernail sensor.

The ability of the human to apply shear forces depends on the coefficient of friction between the finger skin and the surface of contact. To maximize the shear force during calibration, the experimental platform is covered with a soft rubber material, resulting in a static coefficient of friction of approximately 0.75. Therefore, if the normal force ranges between 0 and 3 N, the total shear force can range between 0 and 2.25 N. The preliminary experiments conducted in Chapter 3 indicate that this is well within the range of sensitivity of the fingernail sensor. Shear forces are easiest to apply when the fingerpad is flat against the surface, which usually requires the finger to be in a straight extended posture. Therefore the angles of the MIP and DIP joints should be constrained to be equal to zero during touching. (This implies that θ_{Touch}, the constant bending angle that is predicted by the model when touching is nonexistent, should be equal to zero).

The usable range of finger bending is limited by the natural limit of extension ($\sim -5^\circ$) and flexion ($+90^\circ$). An additional constraint is that the finger should not flex so far as to touch the palm, which might produce sensor measurements that are too similar to touching. Therefore the range of bending will be constrained to $-5^\circ \leq \theta \leq 75^\circ$.

b) Speed of Calibration

To make calibration of the fingernail sensor as convenient as possible, the total training time should be minimized. However, the speed of calibration is also constrained by the dynamics of the fingertip system. If the user is prompted to explore the force space too quickly, the sensor

response will lag too much behind the applied force due to viscoelastic dynamics. If the user explores too slowly, the response may err due to long-term poroelastic creep.

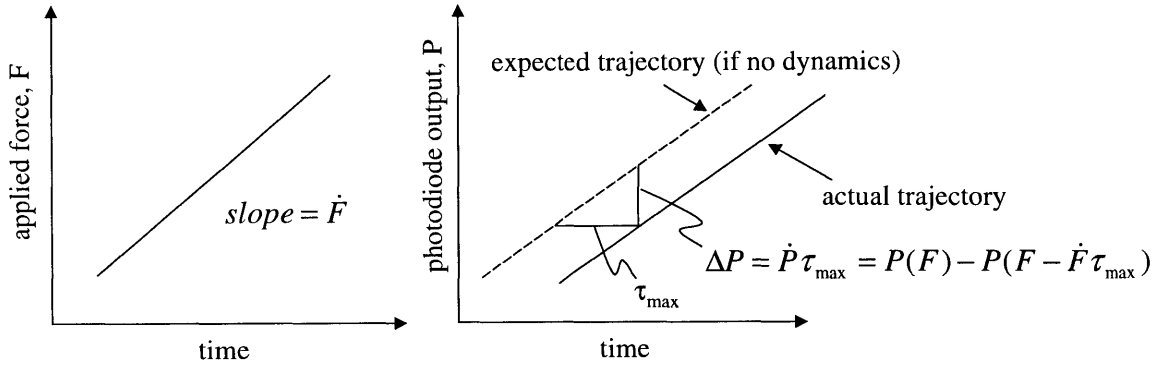

Figure 88: Dynamic Lag
The actual photodiode output lags behind the expected photodiode output according to the slowest time constant of the system.

In principle, if the fingertip dynamics can be approximated as a linear system that is dominated by its slowest mode or "dominant pole" with time constant τ_{max}, and the force is changing at a rate $\dot{F}$, then the sensor outputs will be delayed by τ_{max}, as illustrated by Figure 88 (Ogata, 1990). The error in the photodiode output will be $\dot{P}\tau_{max}$, as if the applied force F were actually $F - \dot{F}\tau_{max}$. If this apparent error in force is expressed as a percentage of the applied force,

$$\%\ error = \frac{\dot{F}\tau_{max}}{F} = f\,\tau_{max} \tag{19}$$

where f is the percent rate of change of force. Therefore, if the time constant is known and a limit is set on the allowable percent error in force, the maximum f can be calculated and used as a constraint on the speed of the prompter.

The experiments at the end of Chapter 4 indicate that the effective time constant of the sensor response is between 0.1 and 0.4 seconds. This is comparable to the viscoelastic time constants of the fingerpad determined by Pawluk and Howe (1999). They reported three stress relaxation modes with time constants of 4 ms, 70 ms, and 1.4 s, with respective magnitudes of 0.41, 0.18, and 0.15. Thus 75% of the dynamics settle within approximately 0.1 seconds. Therefore, if the % error in equation (17) is specified to be 10%, and τ_{max} = 0.1 s, then the

allowable percent rate of change of force is 100% per second. For example, at a force of 1 N, the allowable rate of change is 1 N/s.

On a longer time scale, soft hydrated tissue may exhibit poroelastic creep. According to Holmes (1986), the time constant for such behavior is on the order of 10 minutes. If the total training time is limited to two or three minutes, poroelastic creep should not be an issue.

5.2.3. Trajectory Design

Now that the calibration method and constraints are well defined, the calibration trajectory can be designed. This is the trajectory that the force prompter will execute within the GUI of Figure 87 in order to lead the user to explore the entire force space while training data is collected. The force space to be explored consists of a three dimensional cone defined by the constraints of maximum normal force and frictional shear force, as depicted in Figure 89.

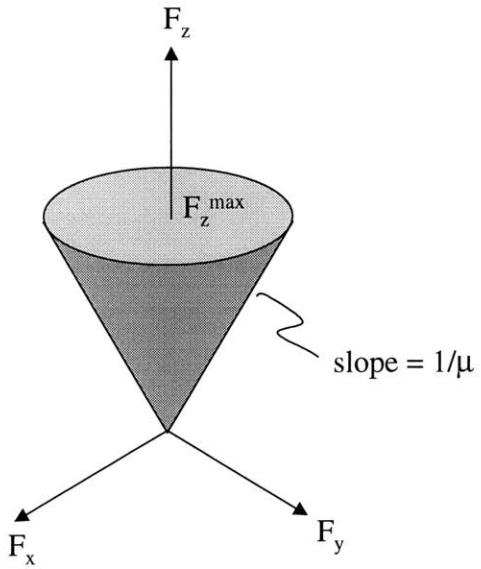

Figure 89: 3-D Force Space
According to the law of Coulomb friction, the possible shear forces are limited by the normal force, and the 3-D space of possible forces has a cone shape.

To efficiently explore this cone-shaped space, an upward moving, spiraling and circling trajectory can be designed as shown in Figure 90. As the normal force gradually increases from zero, the magnitude of shear force periodically increases and decreases while the direction of the shear force circles around. Due to the frictional constraint, the range of possible shear force increases linearly with normal force. However the training data should be spread uniformly

throughout the cone-space in order to create a predictor that is not biased toward any specific portion of the space (unless a specific application suggests otherwise).

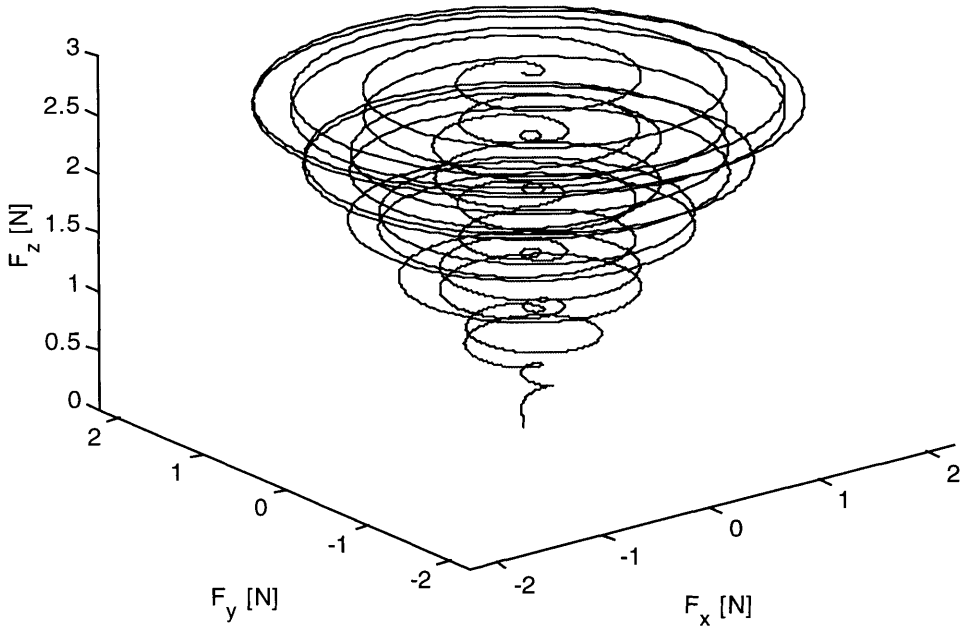

Figure 90: 3-D Calibration Trajectory
A circling, spiraling trajectory is designed to explore the 3-D force space.

The training data can be specified to be of uniform density in either cylindrical coordinates or Cartesian coordinates. If cylindrical coordinates are chosen, the predictor will be unbiased in terms of magnitude and direction of shear force; whereas if Cartesian coordinates are chosen, the predictor will be unbiased in terms of the magnitudes of the individual shear force components. Which method is chosen depends on the application of the predictor. In either case, the training data should be uniform in magnitude of normal force.

In order to create a set of training data with a uniform cylindrical density, the time spent to explore the range of shear force needs to increase linearly with normal force. This relationship can be expressed in differential form by the following equation, which includes the boundary condition that the maximum normal force is reached at time T.

$$dt = aF_z dF_z, \quad t = T \Rightarrow F_z = F_z^{\max} \tag{20}$$

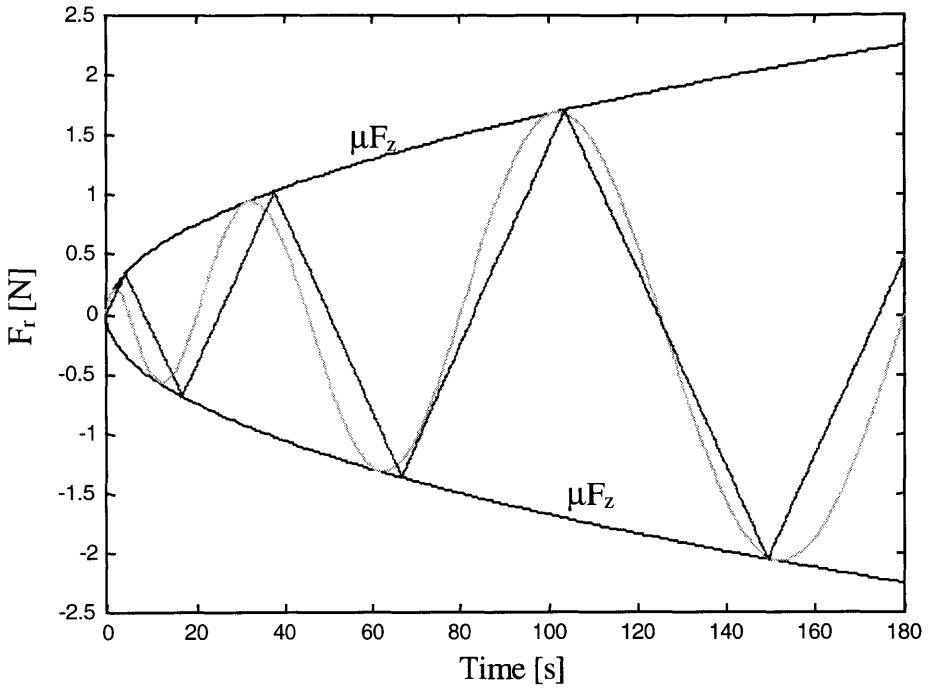

Figure 91: Calibration Trajectory – Radial Temporal Oscillation
The prompt must spend more time at larger normal force for uniform density.

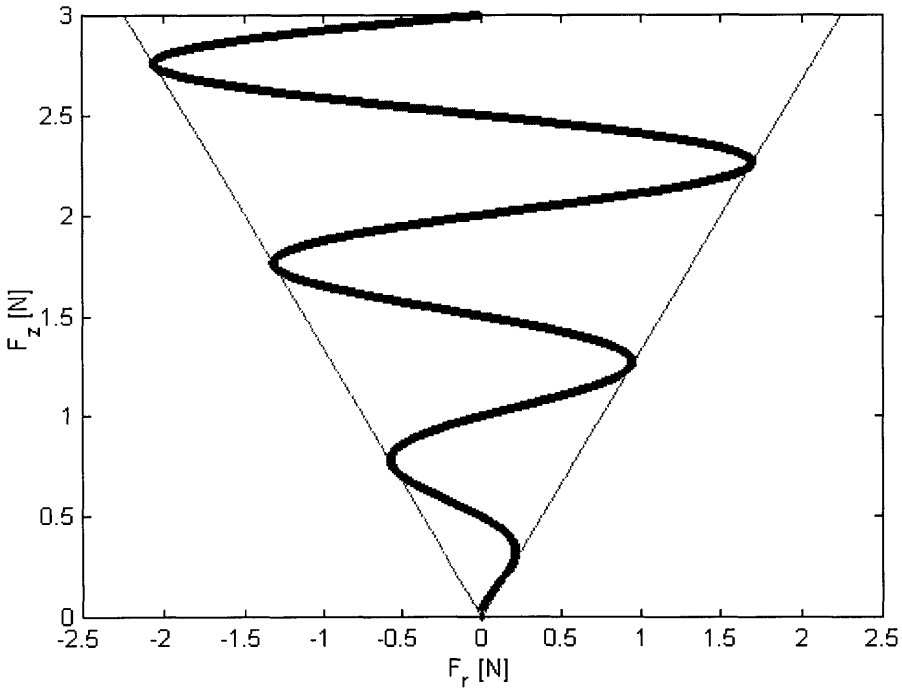

Figure 92: Calibration Trajectory – Radial Spatial Oscillation
The shear force oscillates back and forth between the limits imposed by Coulomb friction.

Integrating and applying the boundary condition gives a formula for normal force as a function of the square root of time:

$$F_z = F_z^{\max}\sqrt{t/T}, \qquad F_z^{\max} = 3\,N, \tag{21}$$

where F_z^{max} is given as shown by the range constraint, and T will be determined later from the speed constraint. Next, in order to create the spiraling action, the magnitude of the shear force, F_r, should oscillate between the minimum and maximum possible values, $\pm\mu F_z$. In order to create a uniform predictor, the rate of change of F_r should have constant magnitude. This requires F_r to be a cyclic function that alternately increases and then decreases linearly with t, as shown by the sawtooth function in Figure 91. However this would result in a jerk in motion whenever the rate of change of F_r switches direction. Instead, if F_r is given by

$$F_r = \mu F_z \sin(2\pi f_s F_z), \quad \mu = 0.75, \quad f_s = 1.0, \tag{22}$$

then F_r oscillates smoothly between the parabolic limits while approximating the ideal sawtooth function, as shown in Figure 91.Viewed as a function of F_z, F_r oscillates with a constant spatial frequency f_s along the F_z axis, as shown in Figure 92. The spiraling frequency, f_s, controls how often the trajectory spirals in and out from the center of the cone as F_z increases. A fast spiraling frequency will make the trajectory denser across F_z, but will require a faster radial speed. A value of f_s = 1.0 creates one cycle of radial oscillation per unit of normal force, as shown in Figure 92.

Finally, in order to create the circling action, the direction of the shear force should rotate around. In order to create a uniform predictor, the speed of rotation should be constant. The lateral and longitudinal components of the shear force are thus given by

$$\begin{aligned} F_x &= F_r \sin(2\pi f_c t) \\ F_y &= F_r \cos(2\pi f_c t) \end{aligned} \tag{23}$$

where f_c is the circling frequency. The ratio of the circling frequency to the radial velocity determines how many times the trajectory circles around for each unit of radial motion. To uniformly cover the force space, the circling frequency should be high enough to complete one or two circles per unit of radial motion, as shown in Figure 93.

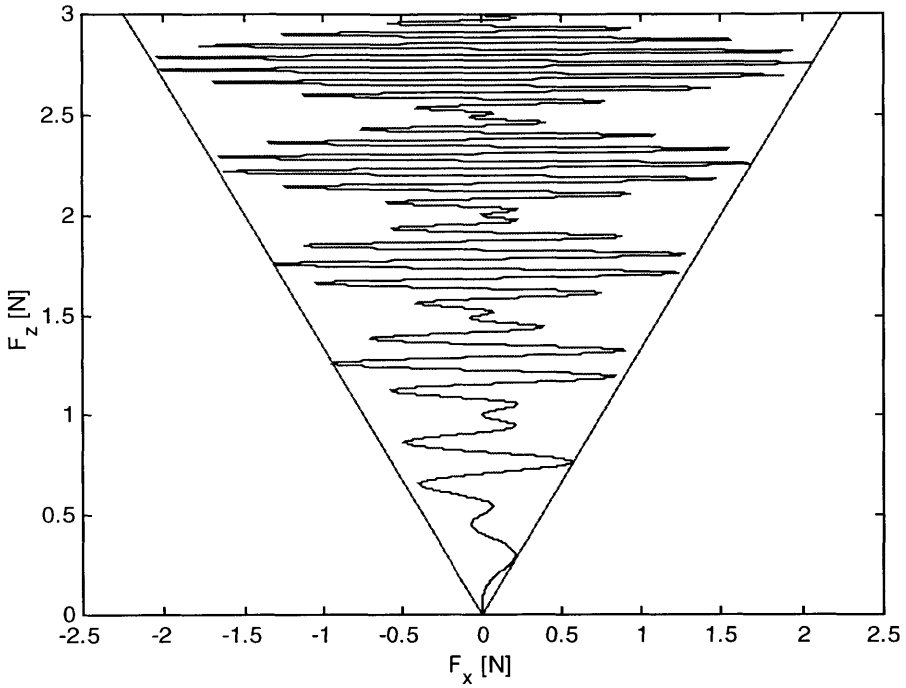

Figure 93: Calibration Trajectory – Spiraling and Circling
The shear force circles in direction as it oscillates in magnitude.

Assuming the circling action takes place much faster than the radial motion and the z-motion, the magnitude of the rate of change of force can be approximated by its tangential component. Thus from equation (23), the percent rate of change of force is approximately $2\pi f_c$. The speed constraint can then be used to choose f_c:

$$2\pi f_c < f_{\max} \Rightarrow f_c < \frac{1\,s^{-1}}{2\pi} \Rightarrow f_c = 0.15\,Hz \tag{24}$$

This then places a constraint on the radial velocity, which must be slow enough to allow one or two circles per unit of radial motion. From equation (22), the maximum radial velocity occurs when $F_r = 0$, and is given by

$$Max\left(\frac{dF_r}{dt}\right) = \frac{\mu \pi f_s (F_z^{\max})^2}{T}. \tag{25}$$

To ensure the time to complete one circle is less than the time to move one radial unit, the following equation must be satisfied:

$$\frac{1}{f_c} < \frac{T}{\mu \pi f_s (F_z^{\max})^2} \Rightarrow T > \frac{\mu \pi f_s (F_z^{\max})^2}{f_c} \Rightarrow T > 140\,s \quad (26)$$

Thus, by choosing a total calibration time T = 180 s (3 minutes), the trajectory will complete slightly more than one circle per radial unit. This is small enough that poroelastic creep is not an issue and that calibration is not overly fatiguing or impractical. Putting everything together, the 3-D trajectory of Figure 90 is achieved as shown. If F_z^{max} were chosen to be 2 N instead of 3 N, then the total calibration time would be only 80 seconds. Thus if the functional range of the sensor were decreased to 2 N of normal force, the calibration would take less than half as long.

Finally, the bending calibration trajectory should be specified. Since there is only one dimension of posture to explore, the joint angle is simply cycled across the constrained range of values:

$$\theta = J_2 = 35^\circ - 40^\circ \cos(2\pi f_b t) \quad (27)$$

A bending frequency, f_b, of 0.1 Hz should be more than sufficient to avoid exciting any dynamics. Several cycles should be executed to average out any variations in bending mechanics that might occur.

5.2.4. Protocol

Now that the calibration trajectories have been derived, the calibration protocol can be specified as follows:

1. Setup
   a. Affix sensor, aligning with tip of finger (not tip of fingernail)
   b. Ensure proper adhesion, especially during bending

2. Touching Experiments
   a. Make sure force platform is calibrated
   b. Position finger to be longitudinally aligned with y-axis of force platform with fingerpad flat against surface (zero bending angle of MIP and DIP joints: θ=0)
   c. Practice touching and following force prompt
   d. Practice bending over desired range and following posture prompt
   e. Reset prompt and begin data collection
   f. Subject follows force prompt for 180 s
   g. Subject follows posture prompt for 60 s (6 cycles)
   h. Stop and save data

i. Repeat steps 2e-2h to collect 2nd set of data
j. Build touch predictor using 1st set of data and validate using 2nd set
k. Test predictor on new randomly generated set of data

3. Bending Experiments
   a. Affix color markers for video tracking
   b. Practice bending with finger next to time index
   c. Align and focus video camera to record finger and time index
   d. Start video recording, reset prompt and begin data collection
   e. Subject follows posture prompt for 60 s (6 cycles)
   f. Stop and save data
   g. Capture video onto computer
   h. Build posture predictor using 1st half of data and validate using 2nd half
   i. Test predictor on randomly generated data

The setup is important in order to ensure that the sensor is aligned properly over the color-changing portion of the fingernail and will not peel off under the influence of touching and bending. Separate touching and bending calibration routines are performed in order to build the touch and posture predictors. The calibration may be repeated as many times as necessary to train the human subject and validate the predictor. Sets of randomly generated data may also be used to test the performance of the predictor. This is especially important for the touch predictor, since the spiral trajectory is such a unique way of exploring the space and may bias the training in some unforeseen manner.

5.3. Experiments

5.3.1. Touch Predictor

Using the calibration method and protocol detailed in the preceding section, touch-force predictors were trained for seven different human subjects. Each subject practiced following the force prompt and then executed the training trajectory three times. The first two times, the data was collected and used to train the predictor using the linear, polynomial and neural network models. The third time, the data was collected and used to validate the performance of the predictors. Results show that the predictor performs significantly better on validation data if calibrated using two sets of training data. This will be discussed in more detail in the following section.

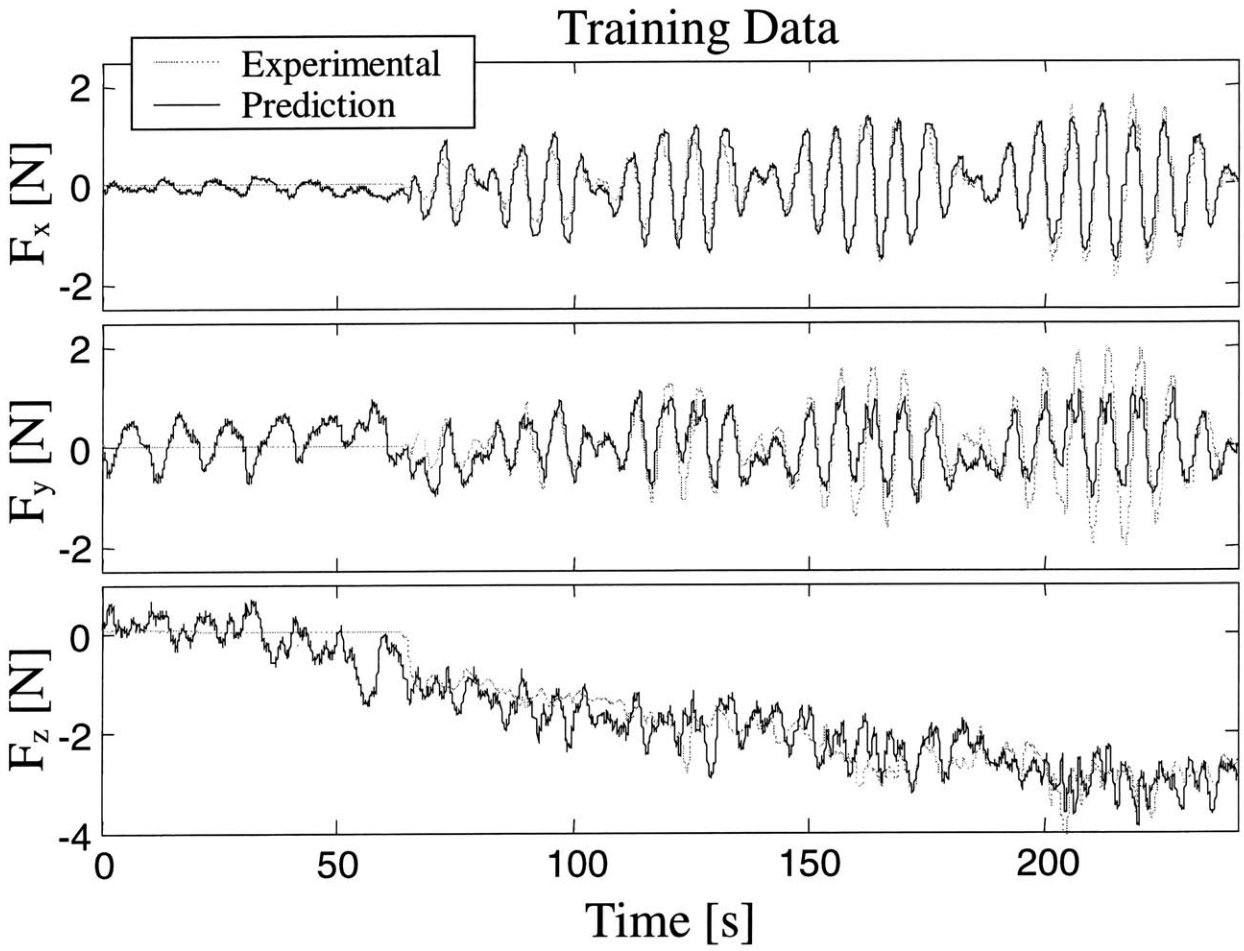

Figure 94: Sample Training Data for Touch Predictor
Sample training data for the touch predictor for a single subject. The data belongs to one of two consecutive spiraling trajectories that are used to train the model. The predicted forces using the linear model are superimposed on experimental forces measured by the 3-axis force sensor.

Figure 94 shows an example of typical training data from a single experiment. The actual forces are zero for the first 60 seconds as the finger is bent back and forth. Then the normal force slowly increases in the negative direction while the two shear forces oscillate with increasing magnitude. The predictions using a linear model are plotted overtop for comparison. The model performs relatively well in training to F_x, while it has some difficulty training to F_y and F_z. The bending motion also appears to interfere more with the training of F_y and F_z. Figure 95 shows the training performance for this sample data. The predicted forces are plotted vs. the actual forces, with the ideal relationship being a line with slope equal to one. As depicted, the predictions are scattered about the diagonal with the root mean squared error (RMSE) noted on each figure.

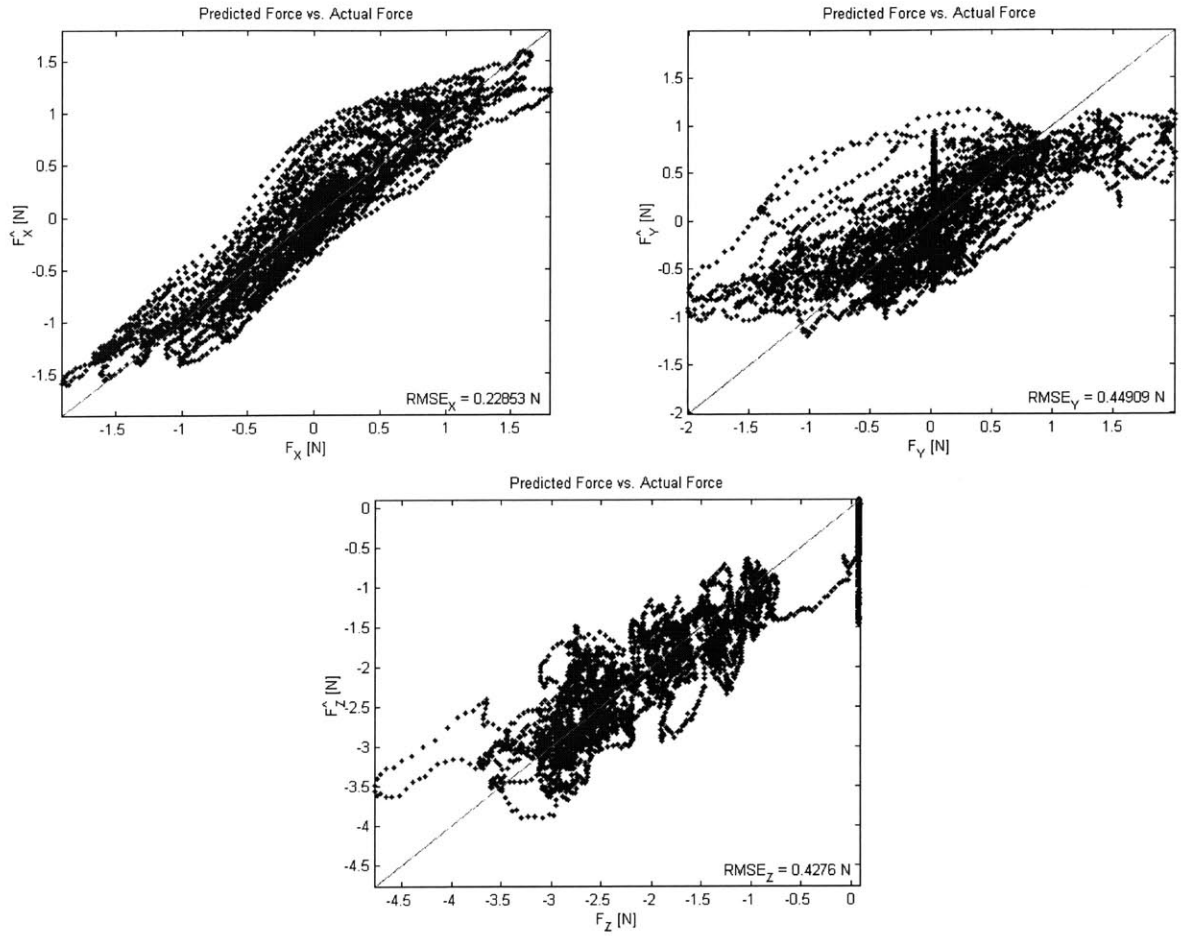

Figure 95: Sample Training Performance for Touch Predictor
Predicted forces are plotted vs. measured forces for the training data. Ideally, the data points should all lie on the diagonal.

Figure 96 shows sample validation data from the same subject. Data from a third spiral trajectory is followed and the forces are predicted based on a linear model that was trained on the first two spirals. The force predictions are plotted overtop of the actual measured forces. In this case, there is a slight degradation in the predictor performance, but the predictor still performs well. Figure 97 shows the validation performance.

Figure 98 shows a sample Singular Value Decomposition (SVD) of the linear model. The SVD decomposes the model of equation (9) into its principal modes and shows which combinations of forces depend on which combinations of photodiode signals (Nakamura, 1991). The relative magnitudes of the singular values (σ_1, σ_2, σ_3) give the relative strengths of the three principal modes. The top plot shows the contributions of the three forces to each of the three modes, while the bottom plot shows the contributions of the eight photodiode signals to each of

the three modes. The important result is that each of the three modes consists of a different combination of the three forces and all the modes are relatively strong. Therefore, the model can independently predict the three forces. In this example, the three modes are each dominated by a particular force, however this is not true in general for all subjects. Each of the three modes also depends on a different set of photodiode signals. In general, for all subjects, it is difficult to say which photodiodes are most important for which forces.

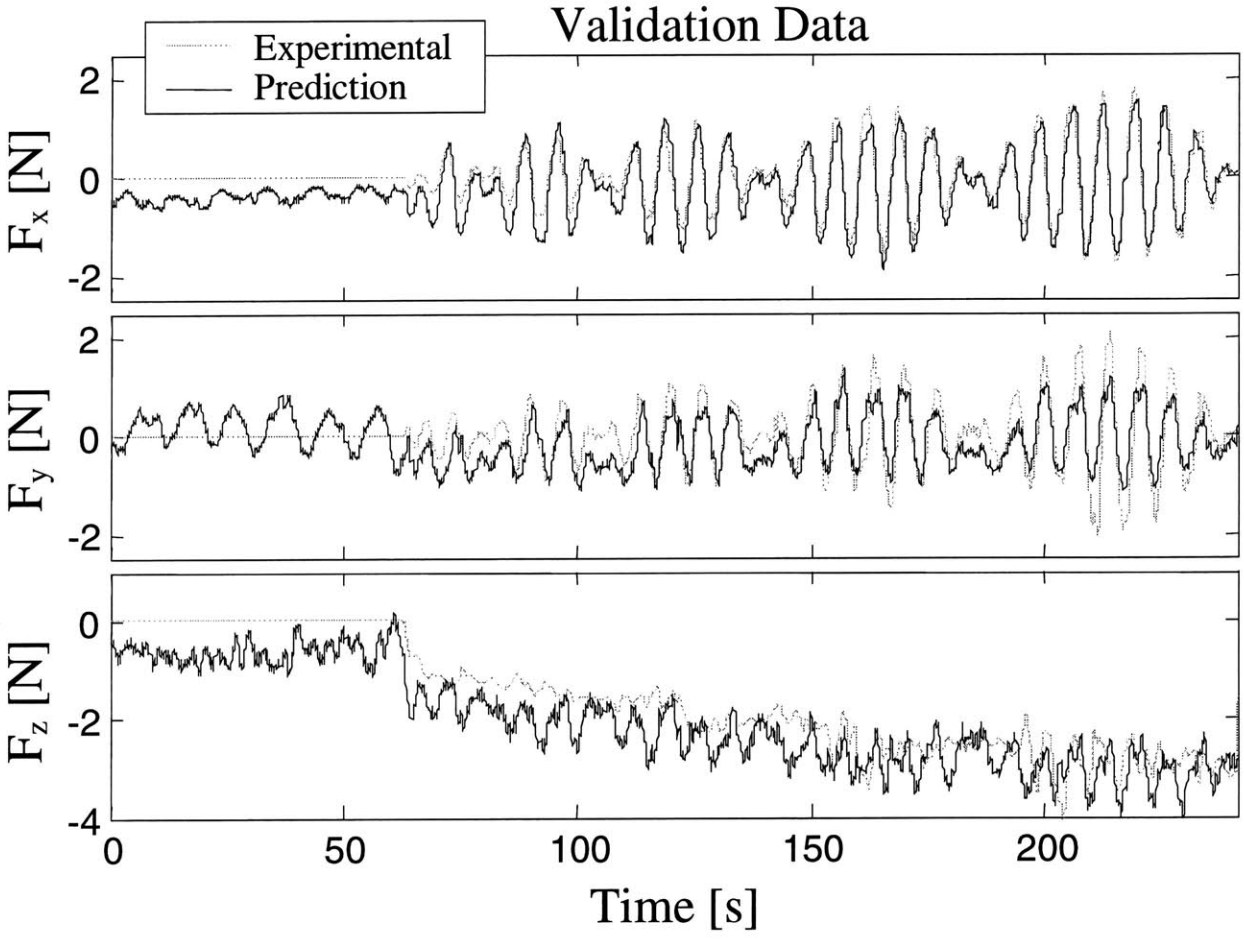

Figure 96: Sample Validation Data for Touch Predictor
Sample validation data for the touch predictor for a single subject. The data belongs to third spiraling trajectory that is used to validate the model. The predicted forces using the linear model are superimposed on experimental data.

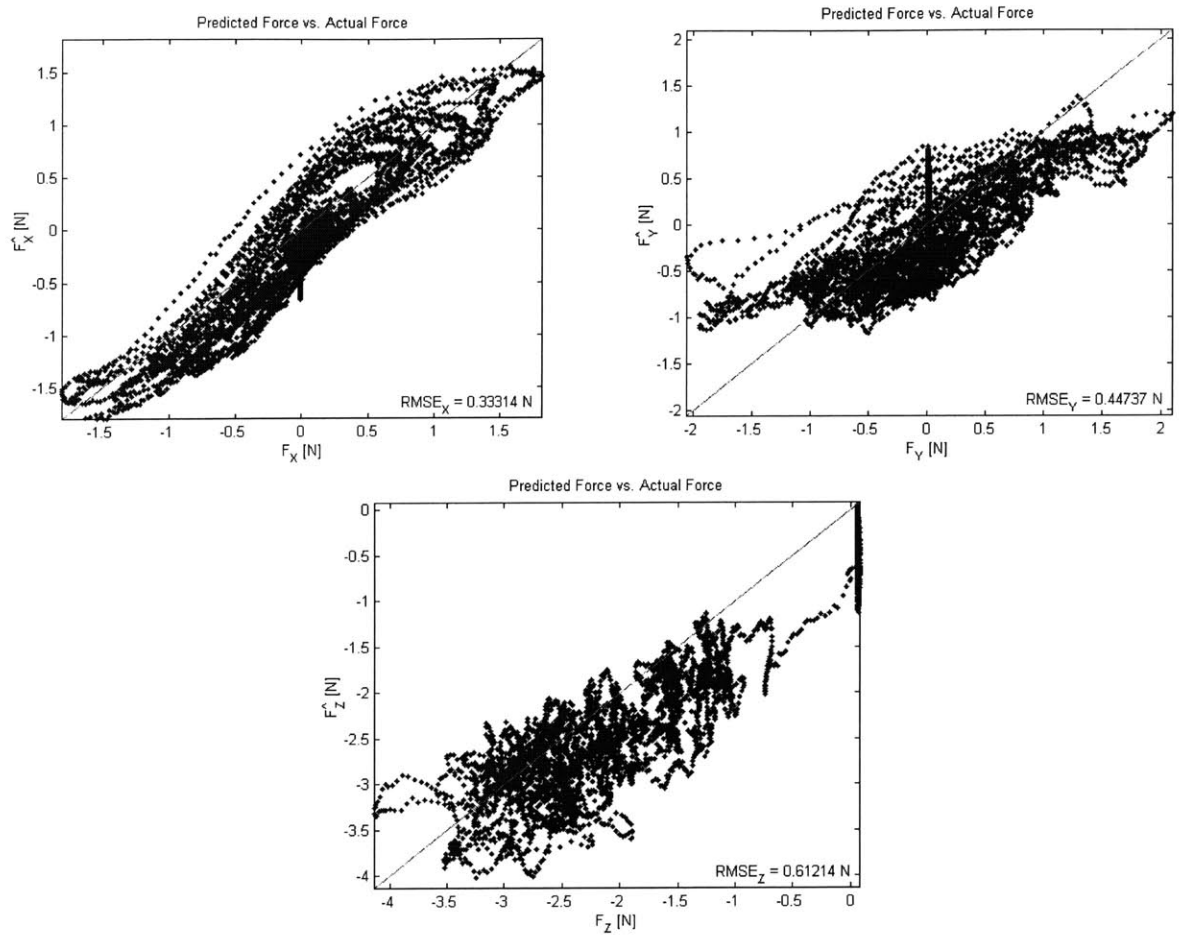

Figure 97: Sample Validation Performance for Touch Predictor
Predicted forces are again plotted vs. measured forces for the validation data.

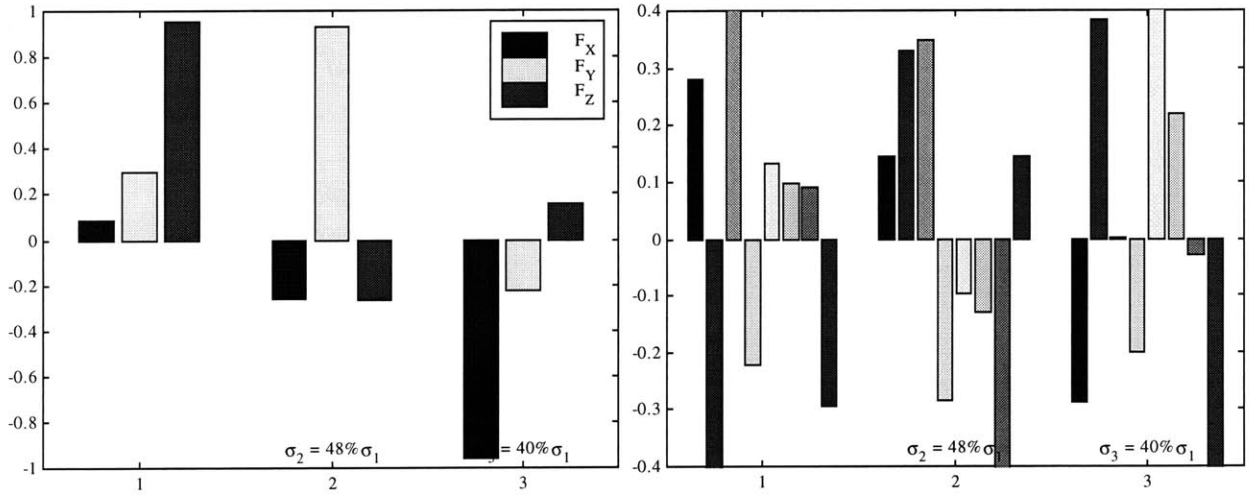

Figure 98: Singular Value Decomposition for Linear Model
The SVD shows which combinations of photodetector readings affect which combinations of forces. In this case, the three forces are fairly decoupled from each other, but the photodiode readings are not. The ratios of the singular values indicate that the model is well conditioned.

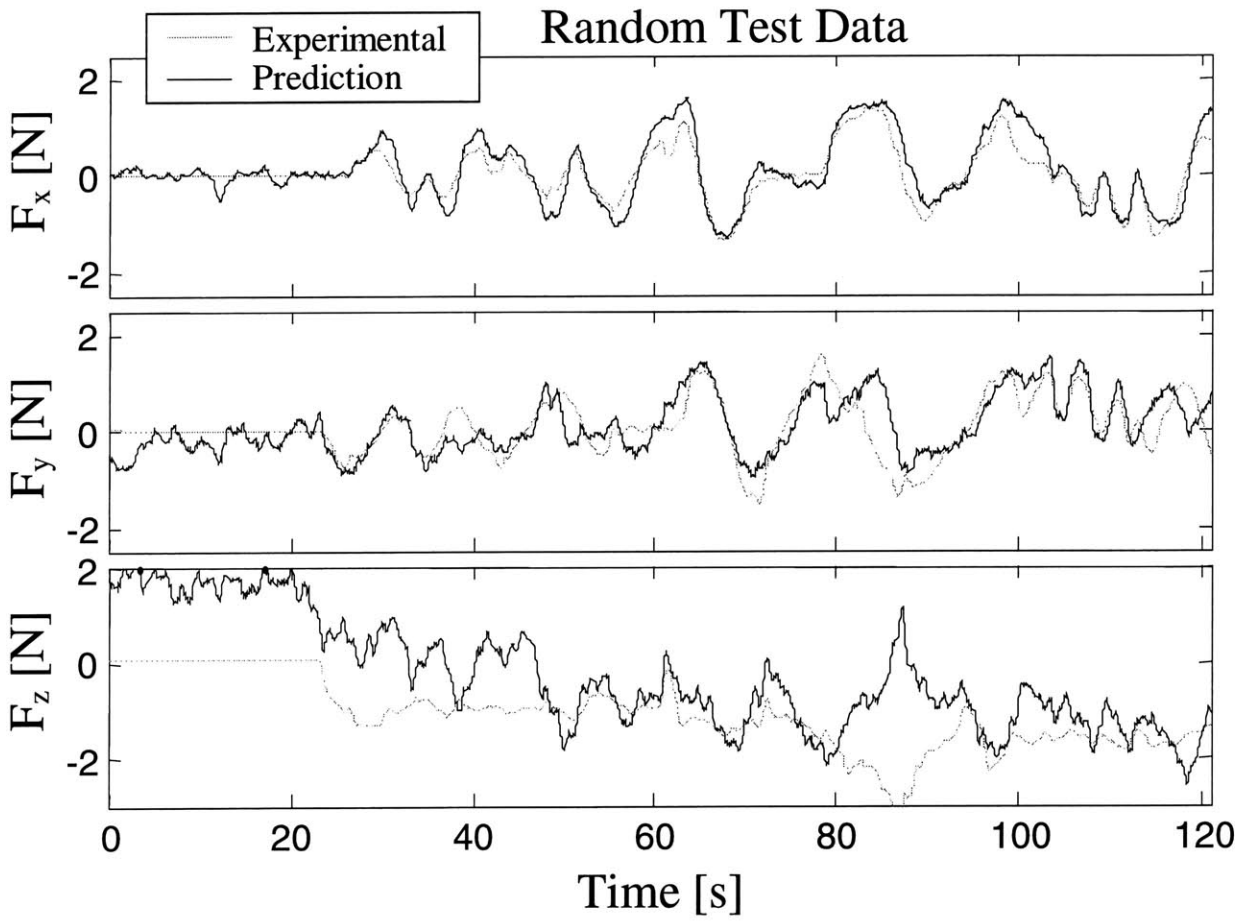

Figure 99: Sample Random Test Data for Touch Predictor
Sample test data for the touch predictor for a single subject. The data belongs to a random user-generated trajectory that is used to test the model. Linear model predictions are again superimposed.

Finally, Figure 99 shows sample test data using a random trajectory. In this case the subject began with 20 seconds of bending followed by 100 seconds of random motion through the force space. The same predictor that was calibrated using the first two spirals was now used to predict the forces for the test data. The predictions are plotted overtop the actual forces for comparison. In this case, the predictor performs well for the shear forces, but suffers a significant degradation in performance for predicting the normal force. The normal force predictions do relatively well at times, but seem to be periodically confused. The performances for the predictor are shown in Figure 100.

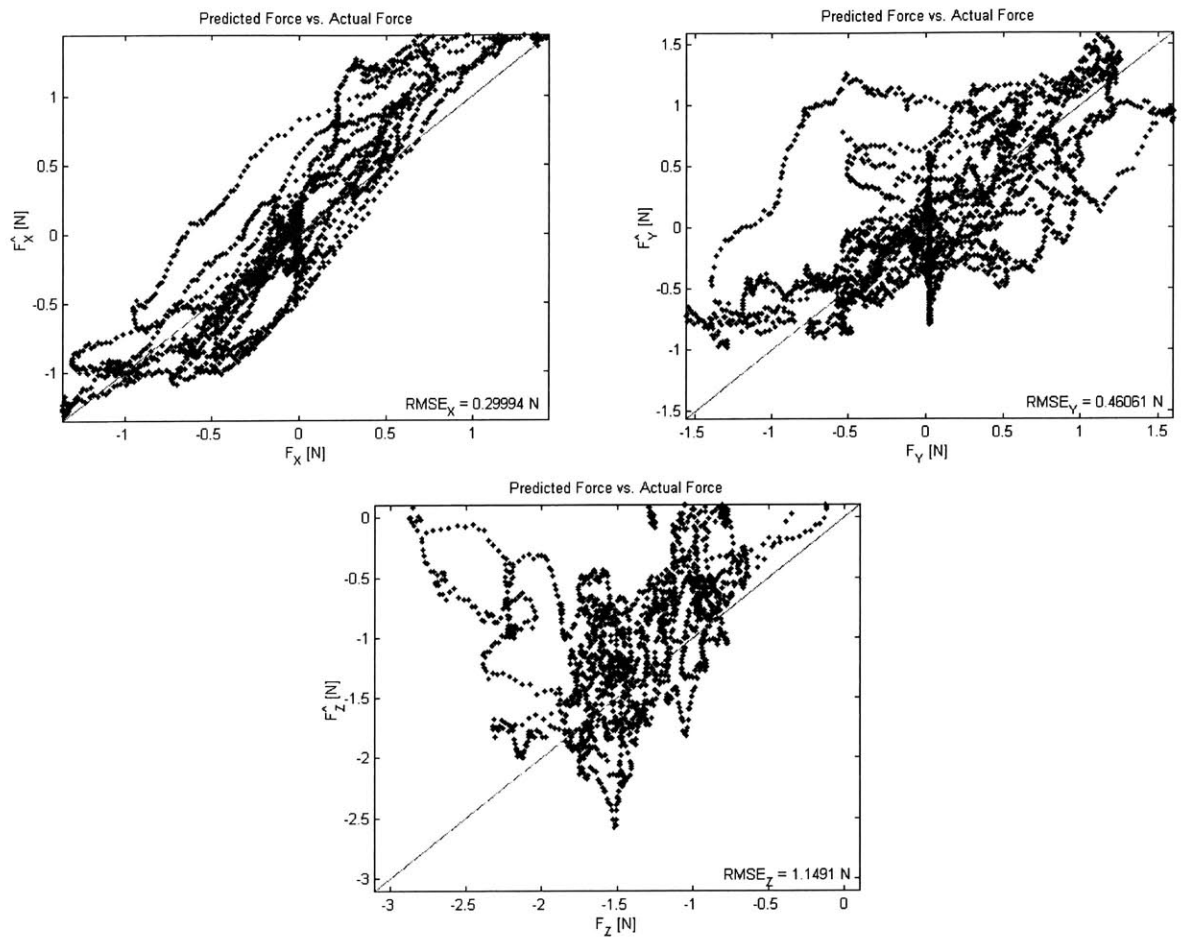

Figure 100: Sample Test Performance for Touch Predictor

Predicted forces are again plotted vs. measured forces for the random test data. Performance is worse for the random data than for the spiral data.

5.3.2. Posture Predictor

Bending experiments were also performed using the same seven human subjects. The subjects were instructed to slowly flex and extend the finger over six cycles at a rate of 0.1 Hz, following the protocol outlined earlier. Figure 101 shows sample training data for a typical subject and Figure 102 shows sample training performance using a linear model.

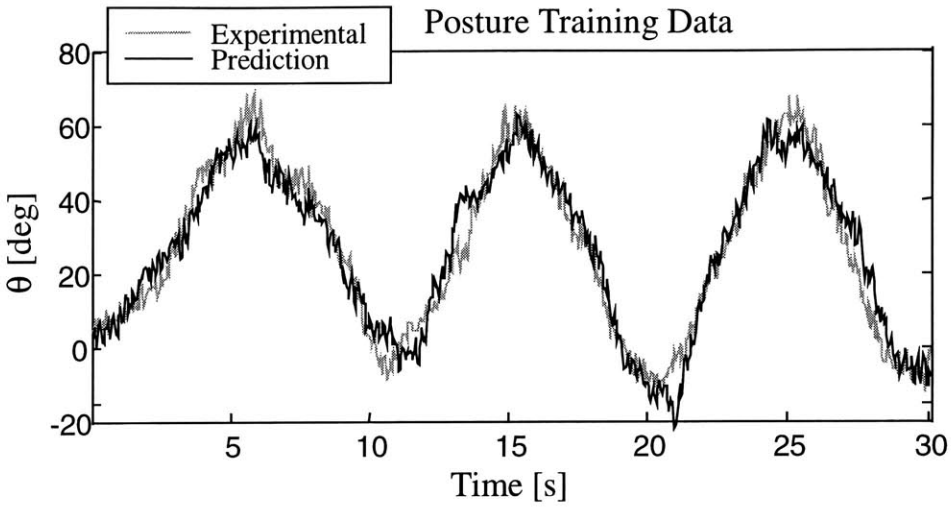

Figure 101: Sample Training Data for Posture Predictor
Training data for the posture predictor for a single subject. The model is trained using the first half of a 60 second data set. The predicted posture angle for the linear model is superimposed on the experimental posture measured by the video tracking system.

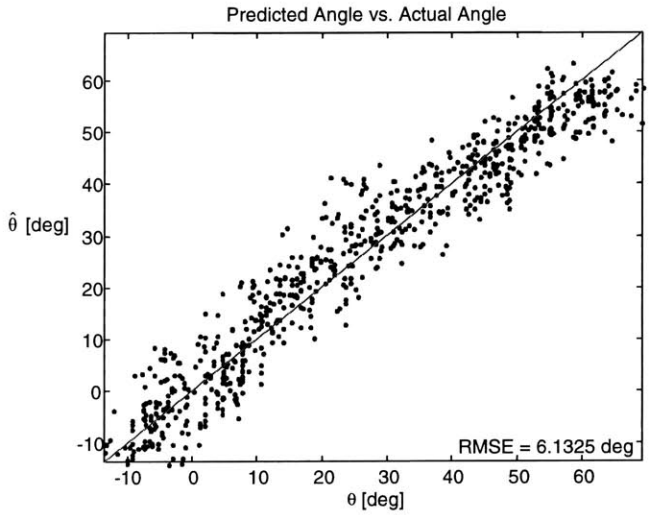

Figure 102: Sample Training Performance for Posture Predictor
The predicted posture angle is plotted vs. the measured angle for the training data. Ideally, the data should lie on the diagonal.

Figure 103 shows sample validation data for the same subject and Figure 104 shows the corresponding performance for the posture predictor trained above. As shown, the model is able to consistently train with RMSE of 6 degrees and predict new data with RMSE of 8 degrees, which is only a slight degradation in performance.

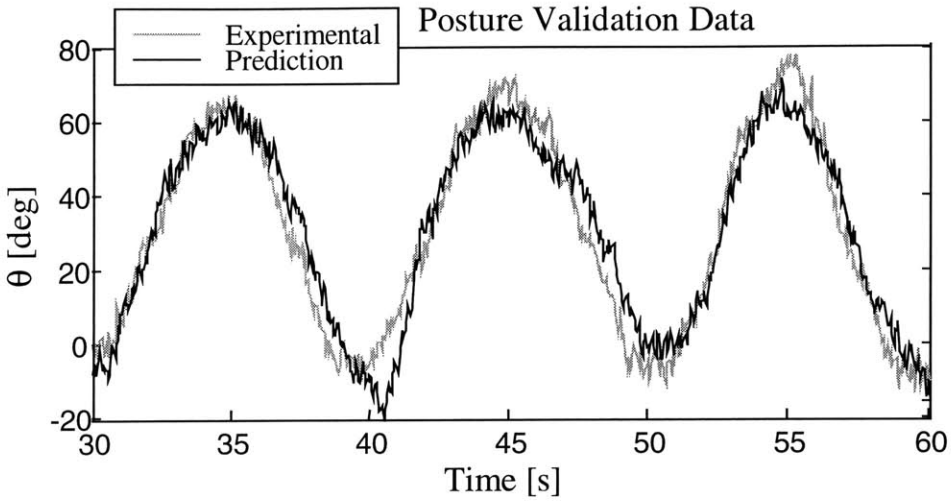

Figure 103: Sample Validation Data for Posture Predictor
Validation data for the posture predictor for a single subject. The model is validated using second half of data set. The predicted posture angle for the linear model is superimposed on experimental data.

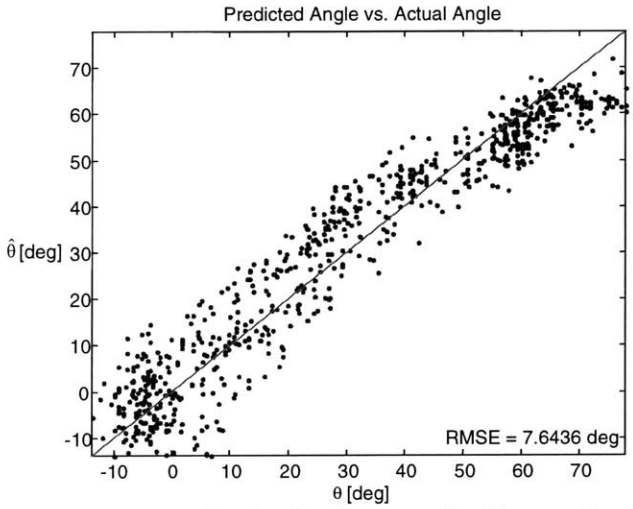

Figure 104: Sample Validation Performance for Posture Predictor
Predicted angle is again plotted vs. the measured angle for the validation data.

5.4. Model Comparison and Analysis

5.4.1. Touch Predictor

In this section, the calibration results from all seven human subjects using all three models are compiled and analyzed. Figure 105, Figure 106, and Figure 107 show the average performances of each of the three models for predicting the validation data (third spiral) when the model is calibrated using either the first, second, or both first and second sets of training data. In each case, the model performs better when trained on the second set vs. the first set. This alone would indicate that there is a learning factor in the calibration procedure and that the

human subjects perform more consistently with more training. However the models perform even better when trained on both the first and second sets, indicating that there is some useful information in the first set that is not represented in the second set.

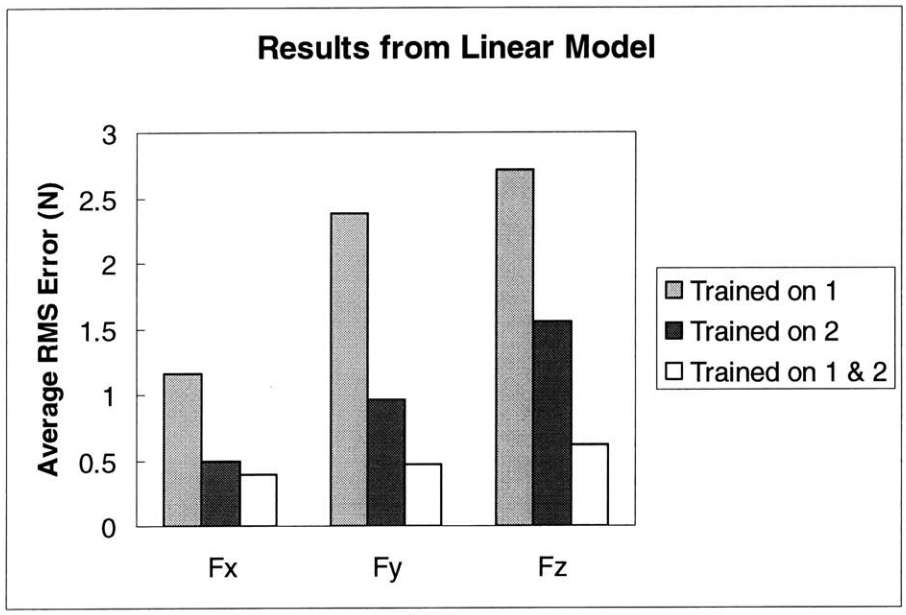

Figure 105: Validation Performance of Linear Touch Model
Root mean square error is averaged over 7 human subjects using the linear model. Performance is best when the model is trained using two separate sets of training data.

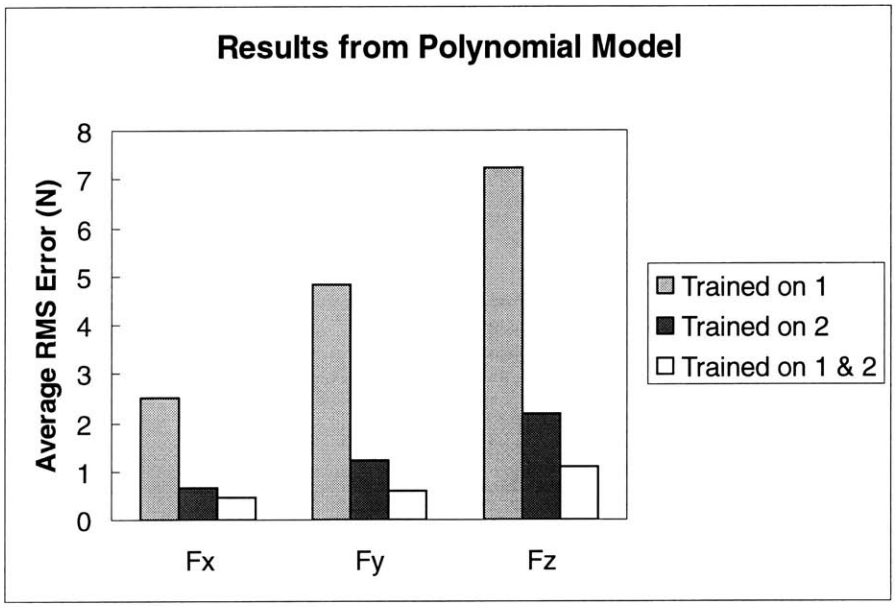

Figure 106: Validation Performance of Polynomial Touch Model
Performance is averaged over 7 subjects using the polynomial model. Performance is again best when two sets of training data are used.

A probable explanation is that some unmodeled variable is changing in between or during the two training sessions. One such variable would likely be the finger having a slightly different posture on the force measurement platform. When two sets of data are used for training, it forces the model to train to the features that remain constant between training sessions.

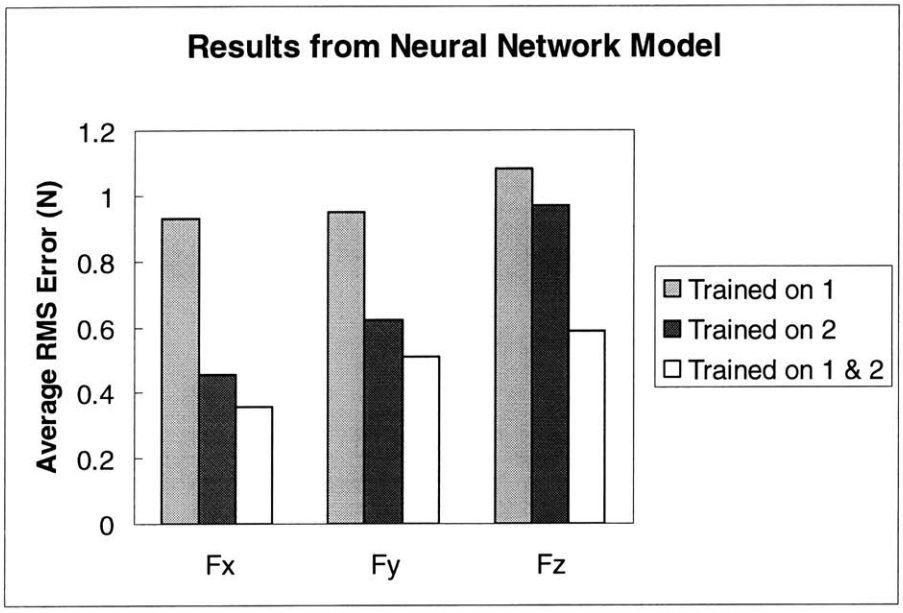

Figure 107: Validation Performance of Neural Network Touch Model
Performance is averaged over 7 subjects using the Neural Network model. Performance is again best when two sets of training data are used.

Figure 108 and Figure 109 compare the average performances (over all seven human subjects) of the three types of models for fitting the training data and predicting the validation data. As shown in Figure 108, the polynomial model fits the training data with the least amount of error because of the large number of parameters. However, as shown in Figure 109, the polynomial model results in the worst error when predicting the forces for the validation data, especially in predicting the normal force, $\mathbf{F}_z$. While the polynomial model is better able to fit the curvature of the data, it actually fits the training data too well. In other words, the polynomial model trains itself to the noise in the training data and thus cannot generalize when predicting forces for new data. Therefore, the polynomial model is unfit for this application and is ruled out.

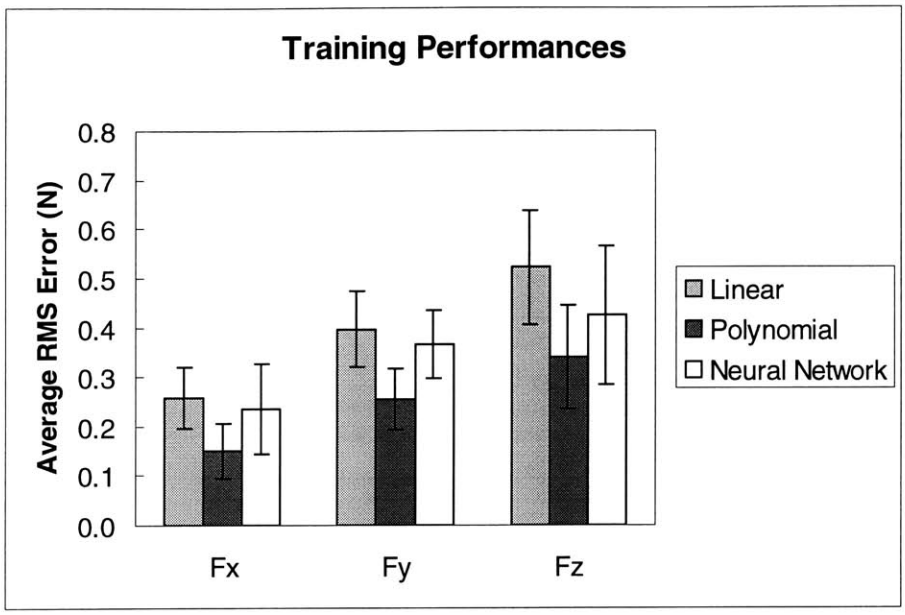

Figure 108: Comparison of Training Performances for Touch Models
Training performances for the touch predictor. The RMS errors of the model predictions are averaged for the 7 human subjects. The results show that the polynomial model fits the training data with the least error.

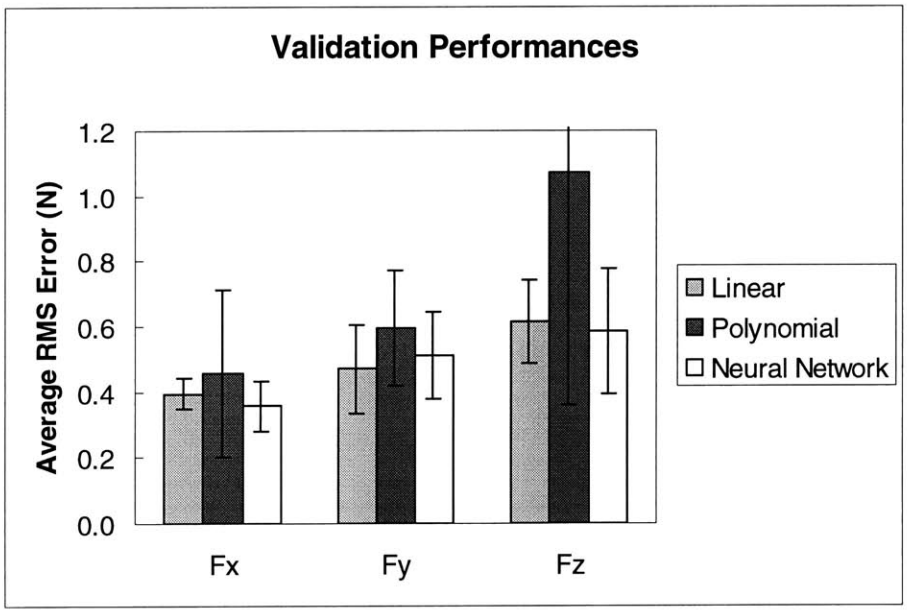

Figure 109: Comparison of Validation Performances for Touch Models
Validation performances for the touch predictor for the same 7 subjects. The results show that the polynomial model performs the worst when presented with new validation data.

The linear and neural network models both show comparable performance for fitting the training data and predicting all three forces for the validation data. The neural network does have more flexibility to fit the data, but is prevented from over-training by the validation check. Using

either the linear model or neural network, all three forces can be predicted with an average RMS error of 0.6 N or less. For further comparison between the linear and neural network models, the performances for predicting the random test data are averaged and plotted in Figure 110. Both models show a decrease in performance in predicting the random test data compared to the spiral validation data, especially in predicting the normal force, F_z. Therefore, there is indication that the method of varying the normal force in the spiral trajectory does not generalize well to arbitrary motion.

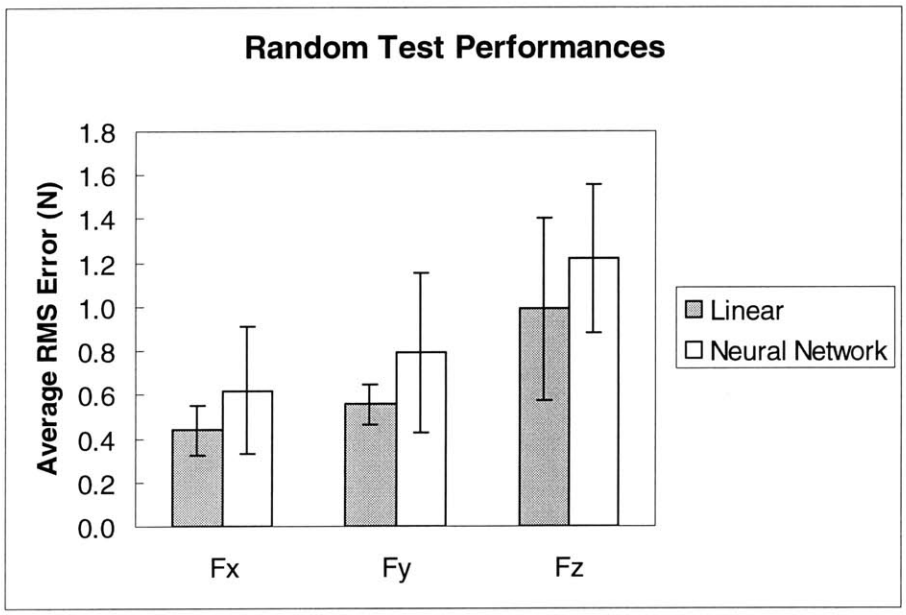

Figure 110: Comparison of Test Performances for Touch Models
Test performances for the touch predictor for same the 7 subjects. The results show that the linear model performs better than the neural network model when presented with new random test data.

When presented with new random data, the linear model performs better on average than the neural network model for predicting all three forces. Especially for the two shear forces, the linear model has a consistently lower RMS error in predicting new random data. Therefore, the linear model, which also has the advantage of being less complex and faster to train, should be used. Using the linear model, the two shear forces can be predicted with an RMS error of 0.6 N or less, while the normal force can be predicted with an RMS error of 1.4 N or less.

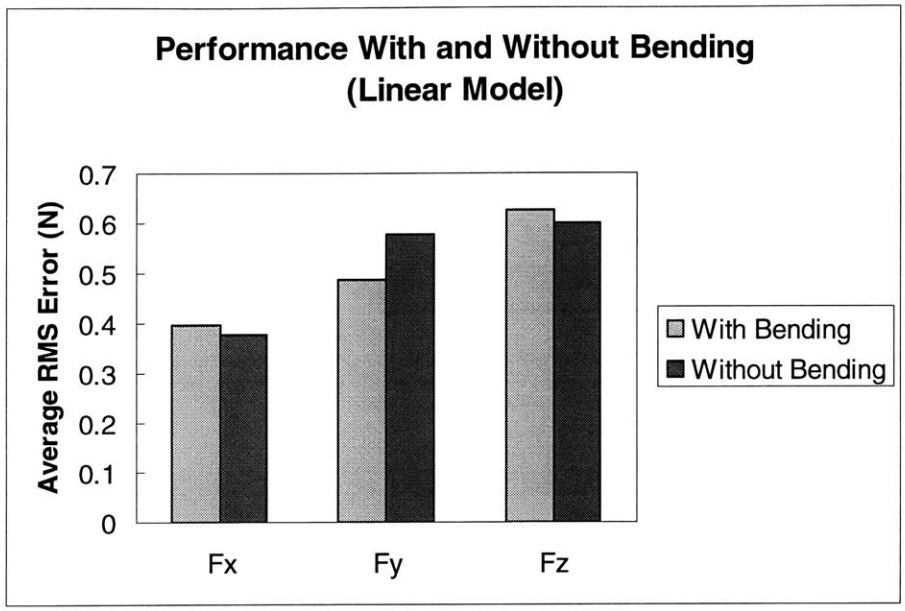

Figure 111: Effect of Bending on Performance of Linear Touch Model
The performance of the linear touch predictor is compared when it is trained with and without bending data. The results show that it does not matter whether the bending data is included or not.

Finally, the effect of including some bending data in the touch calibration is addressed. Figure 111 shows the average performance of the linear model on validation data when the model is trained with and without the 60 seconds of bending. Note that when bending is excluded from the training, it is also excluded from the validation data. Therefore, the figure is only comparing the performance of the model with regards to the types of data it was trained for. If the non-bending trained model were presented with bending, it would naturally have trouble predicting zero force. Interestingly, the inclusion of the bending data appears to have no significant detrimental effect on the touch model performance. In other words, there are sufficient patterns in the data that are not affected by bending to still predict force with the same accuracy. There is a slight loss in performance for F_y, probably because the color patterns for F_y are most similar to the color patterns due to bending (they both result in whitening over the bone). However, since the loss in performance is so small, it is worth including the bending during training in order to make the touch predictor resistant to bending.

5.4.2. Posture Predictor

The performance of the posture predictor should also be compared for the three types of models. Figure 112 shows the average training and validation performances for the three models

when predicting the angle of the PIP joint. As with the touching, the polynomial model over-trains to the data and cannot generalize to the validation data. The neural network model performs slightly better than the linear model on average, but not enough to justify the increased complexity. With the linear model, the bending angle can be predicted with an RMS error of approximately 10 degrees.

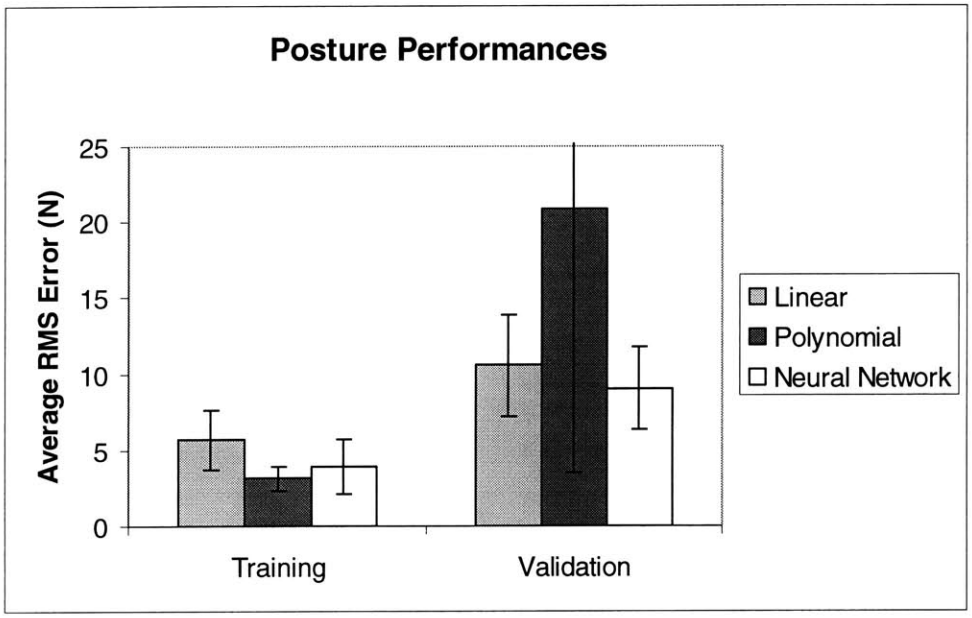

Figure 112: Comparison of Performances for Posture Predictors
Performance of posture predictor for training and validation. RMS errors of model predictions are averaged for 7 human subjects. Polynomial model fits training data better but again performs worst when presented with new validation data. Linear and neural network models are again comparable.

5.5. Sensor Pruning and Optimization

A final piece of analysis that can be performed is to investigate the role of each of the eight photodetectors in the predictor performance. The best way to determine the relative importance of each photodetector is to compute the predictor performance when each photodetector is removed from the predictor. Figure 113 shows the average performance for the seven human subjects when each photodetector is removed from the data pool, and the touch predictor is trained and validated using data from the other seven photodetectors. The performance with none removed is also shown for comparison.

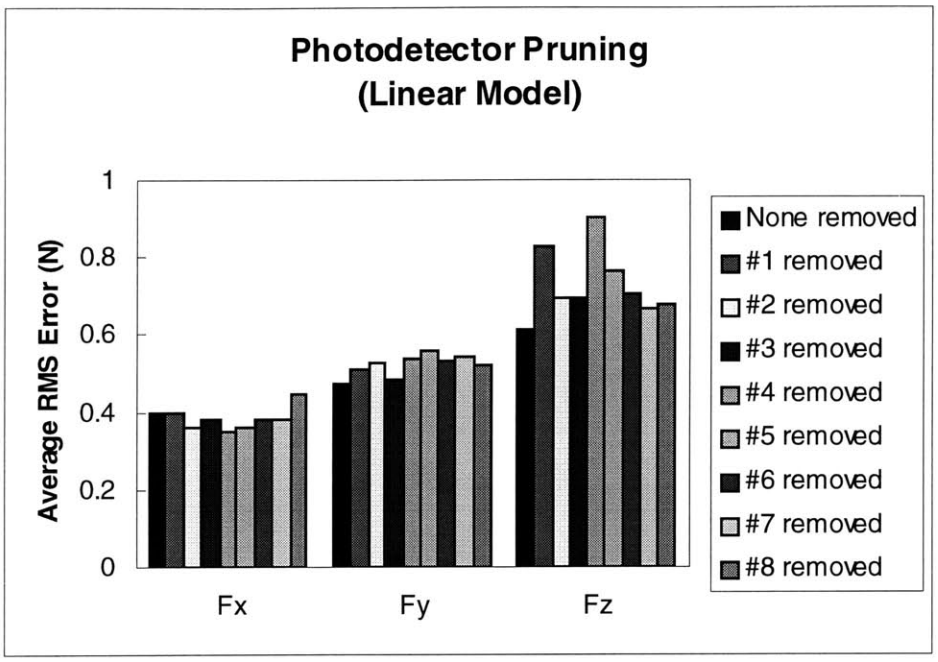

Figure 113: Performance with Photodetector Pruning
Performance of the linear touch predictor is compared when each of the eight photodiodes is removed from the model. The results show that any one photodiode can be removed without sacrificing performance.

Interestingly, the removal of a single photodetector has little effect on the performance in predicting the two shear forces, F_x, and F_y. The normal force, F_z, appears to suffer a noticeable degradation in performance when photodetectors 1, 4, or 5 are removed. However, the removal of photodetectors 2, 3, 6, 7, or 8 seems to have little effect on the performance of the touch predictor in general. This suggests that the next generation of fingernail sensors could be designed with less than eight photodetectors. However, the optimal redesign is not likely to be achieved by simply removing one or more photodetectors and leaving the others in their current configuration. Instead, an optimal redesign should also be based on some study of the effect of photodetector location in addition to quantity. In addition to the experiments and analysis of Chapter 5, the photographic experiments and physical understanding of Chapter 4 should provide important insight into optimal positioning of the photodetectors. However a thorough treatment of this optimization problem and the necessary experimental verification is beyond the scope of this thesis.

6. APPLICATIONS

6.1. Virtual Switches

There are several potential applications for the fingernail sensor in the area of human-machine interface. The simplest application would be on/off detection of touch force. By detecting whether a finger is pressed down against a surface or not, the fingernail sensor could be used as a simple switch. Figure 114 shows the concept of a "virtual switch,", where, the human is instrumented rather than the machine, and the need for a physical switch can be eliminated. Instead an image of a switch can be placed in a flexible location. By combining the fingernail sensor with a position tracker, the system can detect when the user presses a particular virtual switch, and send commands to the machine.

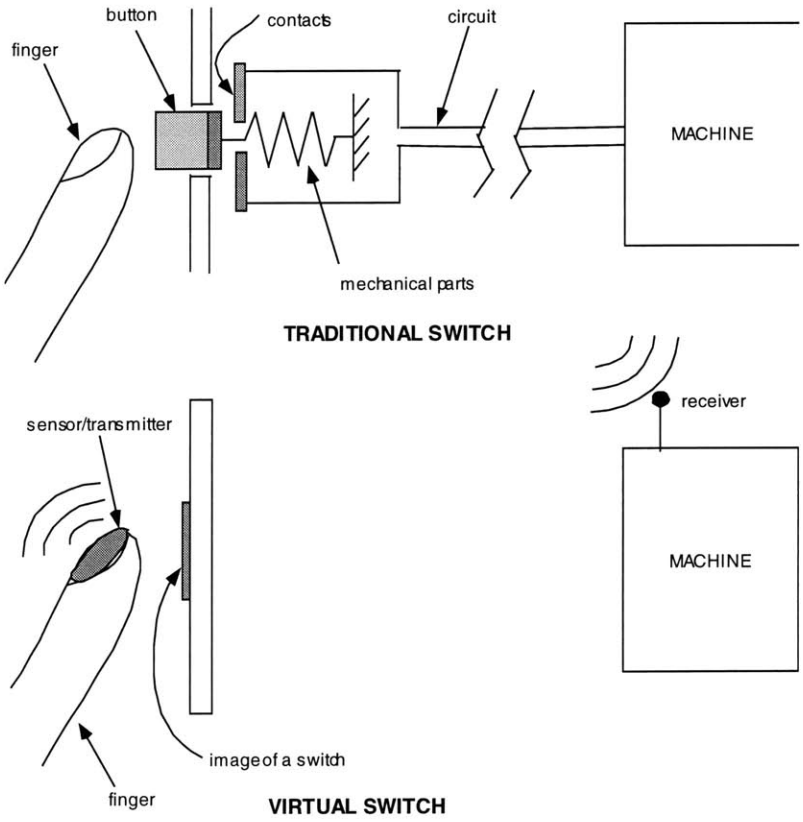

Figure 114: Virtual Switch Concept

A virtual switch is simply a picture of a switch. The switch is activated by the fingernail sensor in combination with a position tracker.

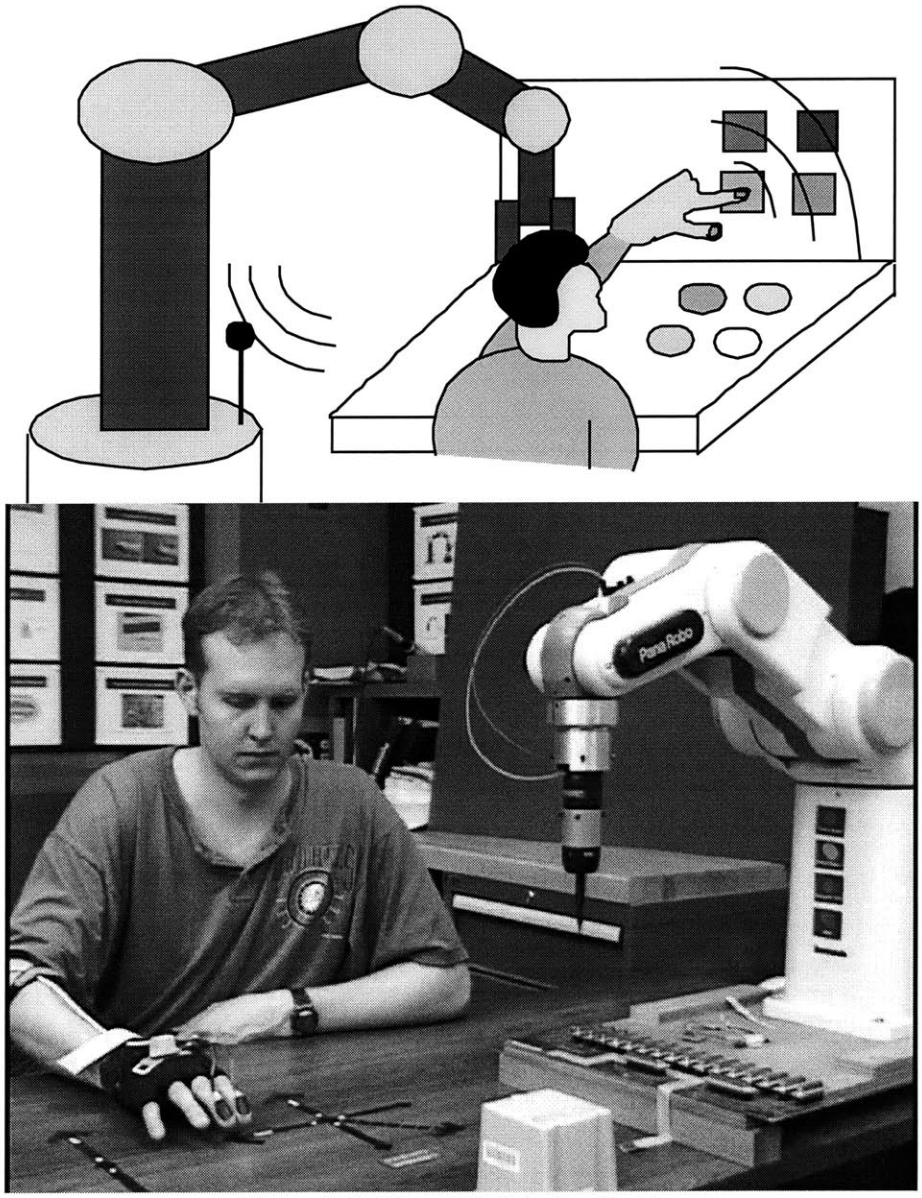

Figure 115: Virtual Switch Application
A virtual switch panel could be used to control a machine such as a robot. The panel would be completely reconfigurable without altering any hardware and can be placed in intuitive arrangements.

Figure 115 shows a virtual switch application where a human wearing fingernail sensors and a position tracker controls a multi-axis robot using a panel of virtual switches. The virtual switches can be located in an intuitive arrangement around the workspace, including on the surfaces of the robot itself, without altering the robot hardware. The virtual switch layout could be reconfigured simply by altering parameters in the control software. Experiments in manual operation of the robot show that user performance can be significantly increased by using virtual switches in place of a teaching pendant. These experiments are presented in detail in Appendix

C. By placing nail sensors on all ten fingers, one could even imagine a virtual computer keyboard, where the user could type on any surface. If the nail sensors could measure a range of magnitudes of touch force, the virtual switches could be further enhanced in functionality.

6.2. Wearable Computer Mouse

By using the fingernail sensor to measure shear forces in addition to normal forces, the sensor could be used as a wearable replacement for a computer mouse, as shown in Figure 116.

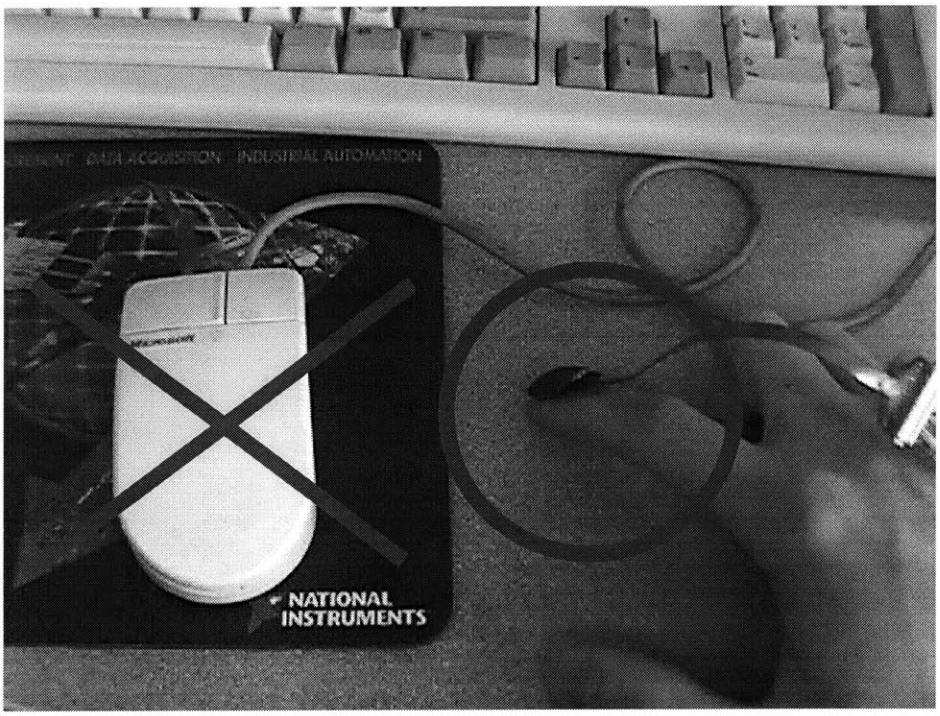

Figure 116: Computer Mouse Application
The fingernail sensor could be used as a wearable mouse in order to control a computer pointer by pushing on any surface.

Lateral and longitudinal shear forces could control the position or velocity of a pointer on the computer screen, while normal force could be used to perform clicking. The "fingernail mouse" could be carried anywhere and used in conjunction with a wearable computer, cellular phone, or PDA (personal digital assistant) device. By instrumenting multiple fingernails, finger posture measurement could also be used to control the pointer location or to provide additional functionality such as performing scrolling actions.

6.3. Skill Monitoring

By simultaneously measuring normal force, shear forces, finger posture, and possibly even location of contact, the fingernail sensor could by used for human skill monitoring. For example, Figure 117 shows a human performing a complex assembly task. By monitoring and analyzing the grasp forces and posture during such an assembly task, the performance of the human could be tracked or a robot could be trained to perform the same task.

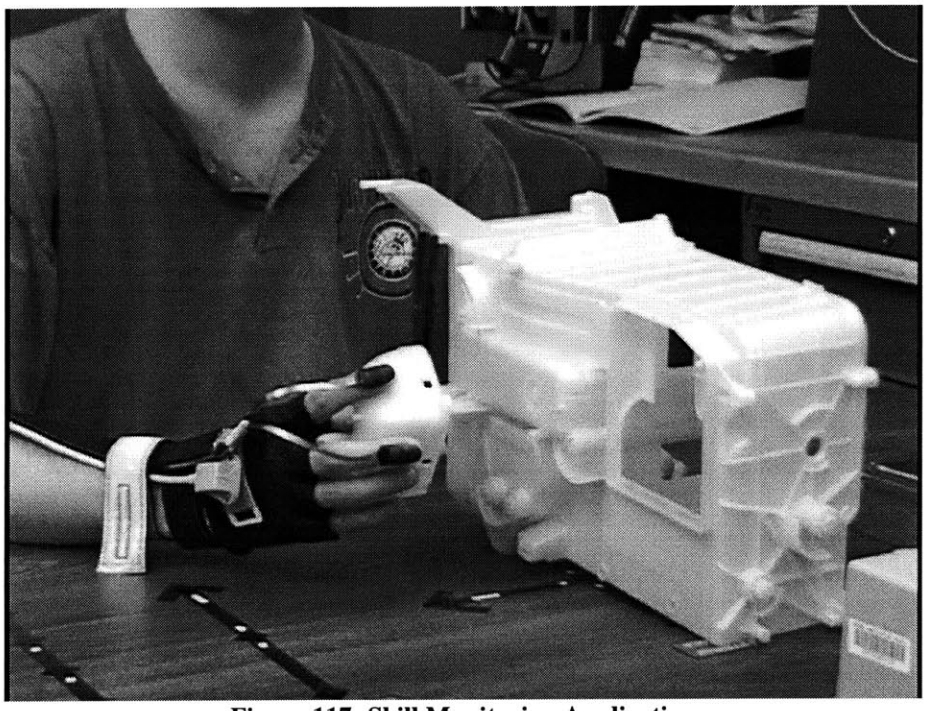

Figure 117: Skill Monitoring Application
The fingernail sensor could keep track of finger posture and forces during a variety of tasks such as assembly or fine manipulation.

7. CONCLUSIONS

7.1. Summary of Contributions

This thesis presented a new type of wearable sensor for detecting fingertip touch force and finger posture. Unlike traditional electronic gloves, in which sensors are embedded along the finger and beneath the fingertips, this new device does not constrict finger motion and allows the fingers to directly contact the environment without obstructing the human's natural haptic senses.

First, a new method of sensing finger force and posture was proposed. Instead of directly measuring the force and posture, the variables of interest are indirectly predicted by measuring the internal state of the fingertip. From several alternatives, the idea of photoplethysmography, or measuring the change in blood volume beneath the fingernail, was chosen; hence, the sensor is mounted on the fingernail and does not interfere with bending or touching actions. Specifically, the fingernail is instrumented with miniature light emitting diodes (LEDs) and photodetectors in order to measure changes in the reflection intensity when the fingertip is pressed against a surface. The changes in intensity are then used to determine changes in the blood volume under the fingernail. By arranging the LEDs and photodetectors in a spatial array, the two-dimensional pattern of blood volume can be measured.

Secondly, a prototype nail sensor was designed to measure the normal touching force, lateral shear force, longitudinal shear force, and finger posture, while eliminating or minimizing the effect of other extraneous variables. A manufacturing process was devised to achieve the desired functional and aesthetic requirements of the sensor. A prototype sensor was then built, and tested using a specially designed experimental apparatus for taking actual measurements of 3-axis touch force and finger posture. Preliminary experiments showed that the sensor responds with different patterns to each of the three forces and finger bending. These patterns are repeatable and consistent with observable fingernail color patterns.

Fourth, physically based, mechanical and hemodynamic models were created in order to understand the mechanism of the blood volume change at multiple locations within the fingernail bed. Relevant fingertip anatomy and physiology along with photographic experiments were used

to construct a qualitative bone-nail interaction model that explained the changes in blood volume beneath the fingernail due to normal force, lateral shear force, longitudinal shear force, and finger bending. Then a quantitative lumped-parameter dynamic model was created to simulate the dynamics of the sensor response. The dynamic properties were verified using experiments with several human subjects, and served as guidelines for further experimentation.

Fifth, data-driven mathematical models were designed to comprehensively predict normal touching forces, shear touching forces, and finger bending based on readings from the sensor. Two separate predictors for touch force and posture were devised, and three types of models were used for each: linear, polynomial, and neural network. A method to experimentally calibrate the predictors was designed using a special graphical interface to prompt the user to explore the entire range of possible forces and finger posture. Experimental data was collected and analyzed for several human subjects. Results indicated that a simple linear model performs best. The two shear forces can be consistently predicted with an average RMS error less than 0.6 N, the normal force can be predicted with an average RMS error less than 1.4 N, and the angle of the PIP finger joint can be predicted with an average RMS error of 10 degrees. Analysis also shows that one or more photodetectors could be removed with little effect on the predictor performance.

Finally, applications to human-machine interface were discussed, along with the functional requirements placed on the sensor. The fingernail sensor could be used for applications such as a virtual switch for interacting with machines and robots, a wearable computer mouse or PDA interface, or a non-obtrusive skill monitoring system for teaching robots or tracking human performance.

7.2. Future Areas for Research

There are several potential areas of future research that could expand upon the work in this thesis:

1. **Sensor redesign based on optimal positioning of LEDs and photodiodes**. Experiments in Chapter 5 indicate that one or more photodiodes could be removed from the nail sensor with a small tradeoff in performance of the force predictor. The physical understanding in Chapter

4 also indicates that the photodiodes could be placed in a more advantageous arrangement. Future research should include redesign of a pruned sensor with optimal positioning of photodetectors.

2. **3-D finite element model of the fingertip including bone-nail interaction**. In the past, 2-D and 3-D finite element models of the fingertip have been created in order to investigate the mechanics of the human fingerpad (Raju, 1998). However, none of these models take into account the mechanical interaction between the fingernail, bone, and surrounding tissues. A new 3-D finite element model (FEM) including the fingernail and connective tissues could verify the physical mechanisms presented in Chapter 4 of this thesis and further increase the understanding of how forces affect the tissues underneath the fingernail.

3. **Real-time virtual finger model with fingernail** (controlled by human with fingernail sensor). Virtual environments often include a virtual hand model that is controlled by the human and used to touch and grasp objects in the virtual environment. Haptic feedback from the virtual fingers is then presented to the human, creating a closed loop haptic control system, where the human is the controller. In order for the human to accurately and naturally control the virtual fingers, the virtual fingers should behave as much like human fingers as possible. Since the mechanics of a real finger depend so highly on the presence of the fingernail, the realistic virtual finger should have a fingernail as well, including a model of the mechanical interaction between the nail and bone. Readings from the fingernail sensor worn on the real finger could be used to drive the virtual finger model in the virtual environment.

4. **Biomimetic robot finger with fingernail and fluid flow**. Another step beyond creating a virtual finger with a fingernail is to create a biomimetic robot finger with a fingernail and nail-bone connection. This robot finger would benefit from the enhanced grasping functionality that the fingernail gives to the human, such as improved ability of the fingerpad to conform to surfaces and exert shear forces. Han, et al. (1996) have already created a robot finger with a bone, fingernail, and elastic tissue, which shows improved ability to exert shear forces during grasping. However their finger does not include connective fibers between the nail and bone. By adding fluid to the robot finger to mimic the blood flow in a real finger,

additional novel robotic functionalities could be researched. Fluid could be used for temperature regulation of a shape-memory alloy actuated finger. It could also be used as a pressure sensing mechanism, just as the blood in the real finger allows the nail sensor to measure touch pressure. A robot finger that secretes fluid or "sweats" could also have a novel type of friction control.

APPENDIX A. SENSOR MANUFACTURING PROCESS

1. **Begin with custom printed circuit board**

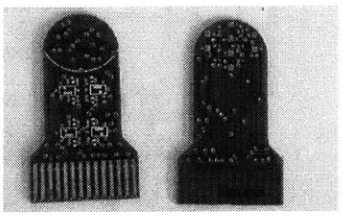

2. **Solder on 14-pin connector**

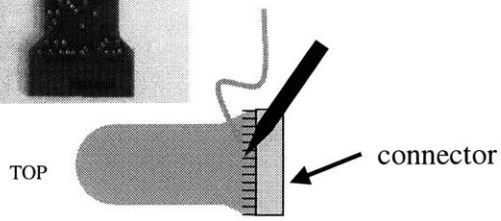

3. **Coat with protective epoxy**

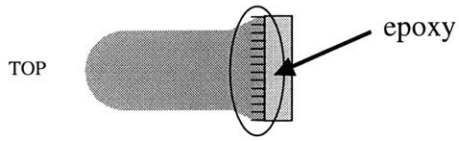

4. **Attach LEDs and photodiode arrays using conducting epoxy**

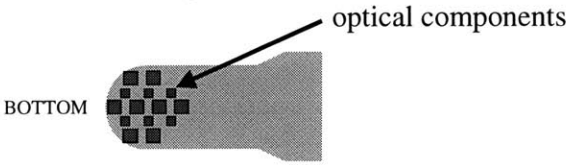

5. **Shield photodiodes from LEDs using opaque epoxy**

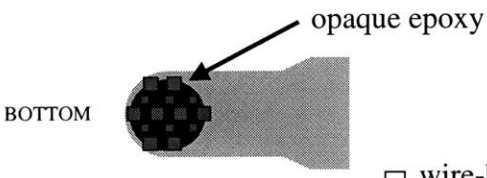

6. **Wire-bond LEDs and photodiodes**

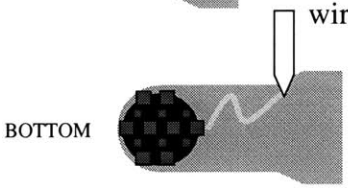

7. **Coat with transparent epoxy**

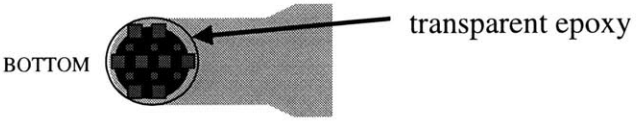

8. **Attach op-amps and resistors using non-conducting epoxy**

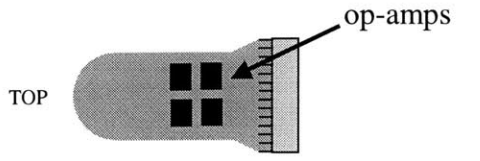

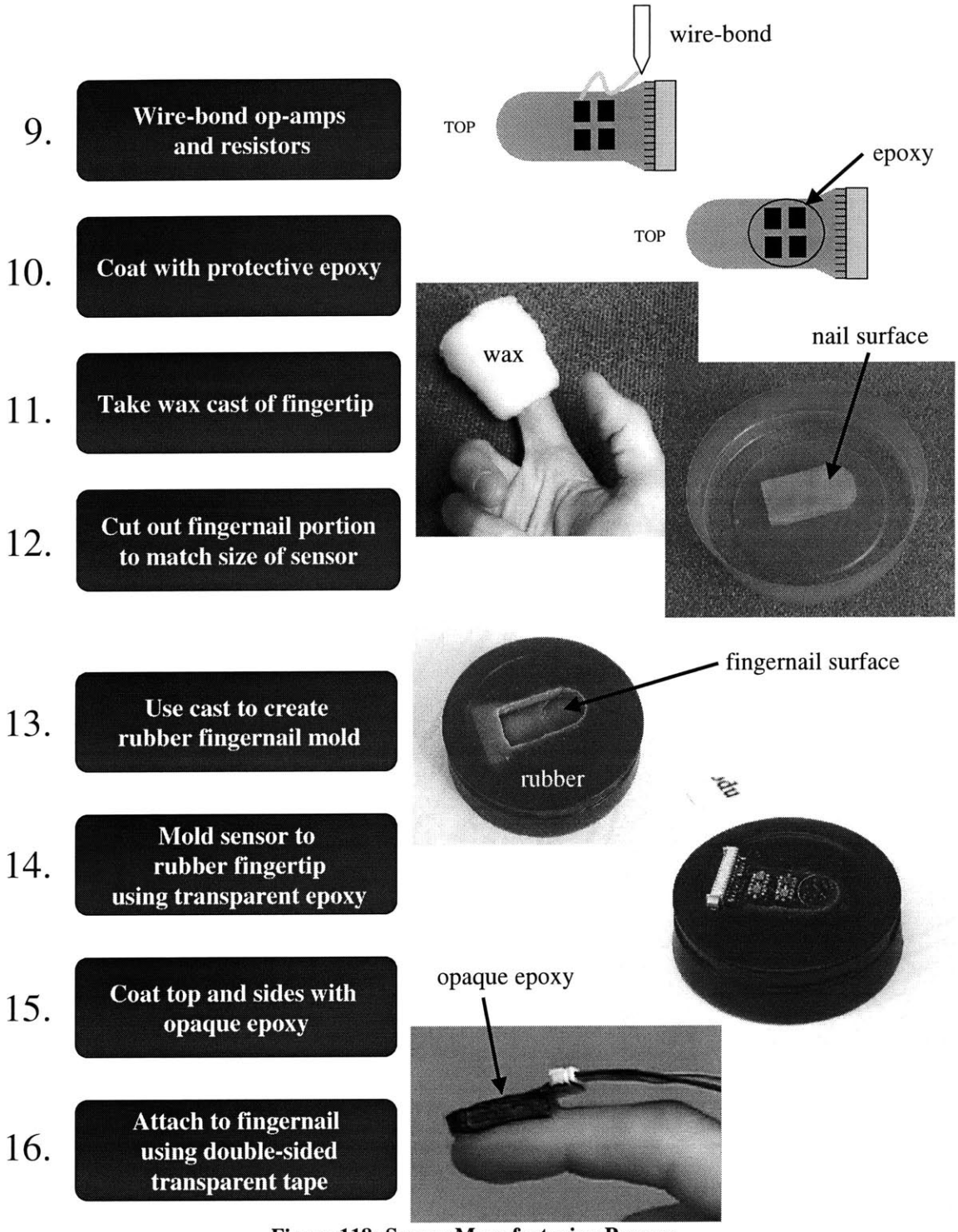

Figure 118: Sensor Manufacturing Process
This figure demonstrates the steps involved in the assembly of the fingernail sensor including the circuit assembly and the molding process.

APPENDIX B. EXPERIMENTAL HARDWARE

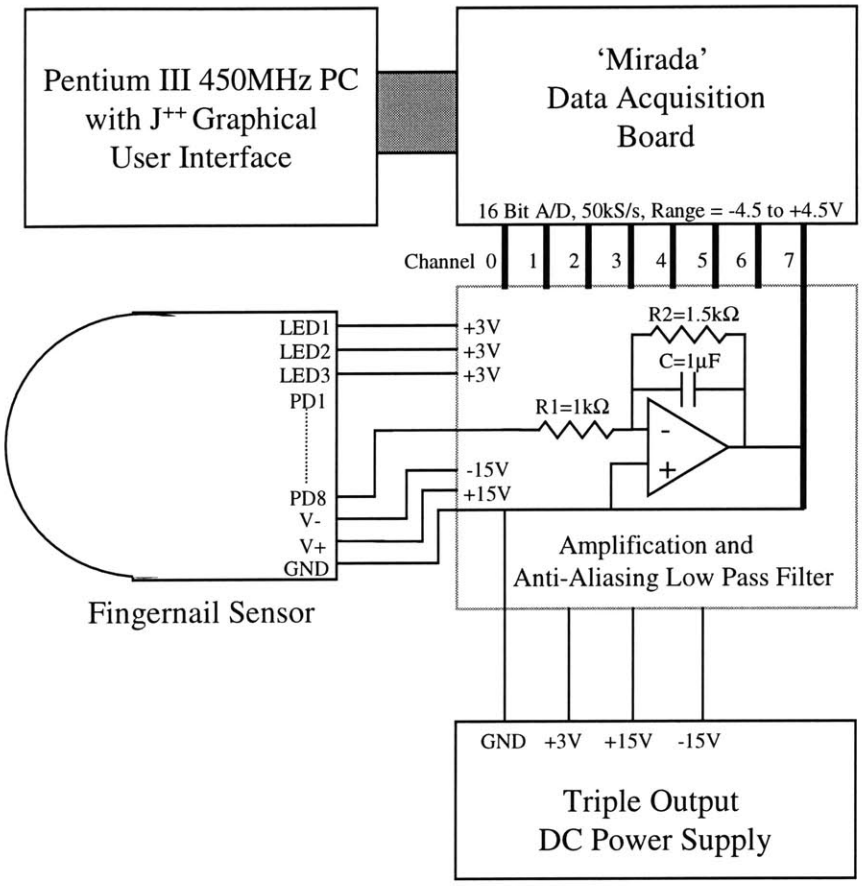

Figure 119: Experimental Hardware
The figure shows a schematic of the signal conditioning circuitry, power supply, and data acquisition system used to operate the fingernail sensor.

APPENDIX C. VIRTUAL SWITCH EXPERIMENTS

Since the virtual switch increases flexibility in terms of positioning and functionality, it seems reasonable to expect that increased performance can be achieved by making the virtual switch panel more intuitive than a traditional switch panel. A good case study for this hypothesis is the teaching of an industrial robot such as the PanaRobo KS-V20 manufactured by Panasonic. Figure 120 shows a picture of the robot and its teaching pendant. The robot has five rotational joints in series and can be controlled in joint angle mode or linear Cartesian mode. As seen in the figure, the top three pairs of buttons on the right are used for linear Cartesian moves, and the top five pairs are used for joint angle moves.

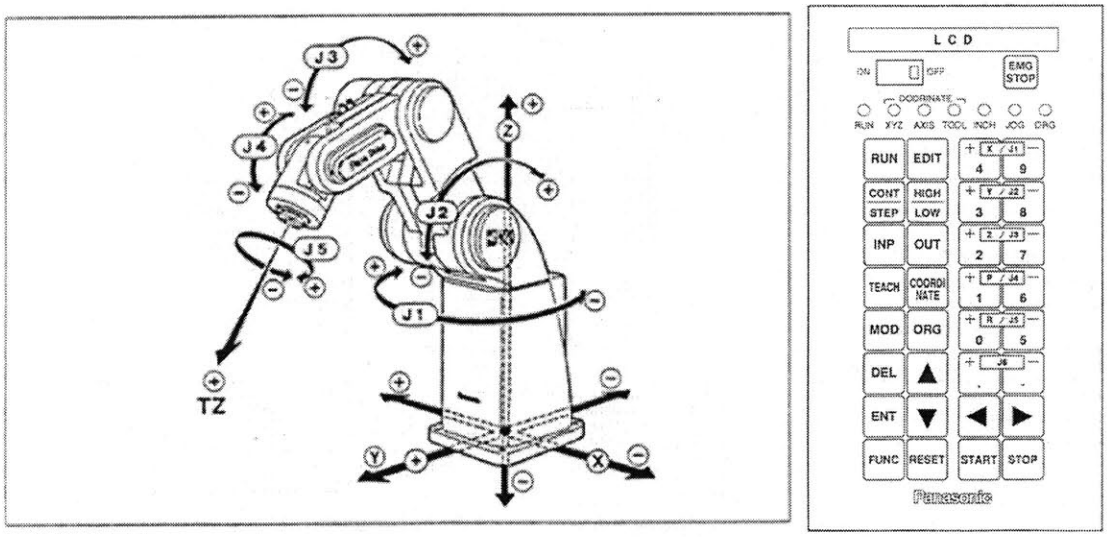

Figure 120: PanaRobo KS-V20 and Teaching Pendant
The teaching pendant is hard to operate because there is no physical intuition as to which button causes what direction of motion, particularly if the pendant is not held so as to be aligned with the robot coordinate system.

A major limitation of this standard method of control is the lack of intuition between the buttons on the pendant and the resulting actuation of the robot. Depending on which way the person is facing the robot, a right button could, for example, cause the robot to move to the left. A button for a particular joint has no intuitive connection to the particular joint of the robot. Intuition can be greatly enhanced by using a virtual switch panel. By using virtual switches, we now have the option of mounting switches on the workspace and the robot itself. Because the switches are virtual, they are not at risk of being damaged within the workspace environment, and they do not require any physical modifications to the robot hardware or the workspace.

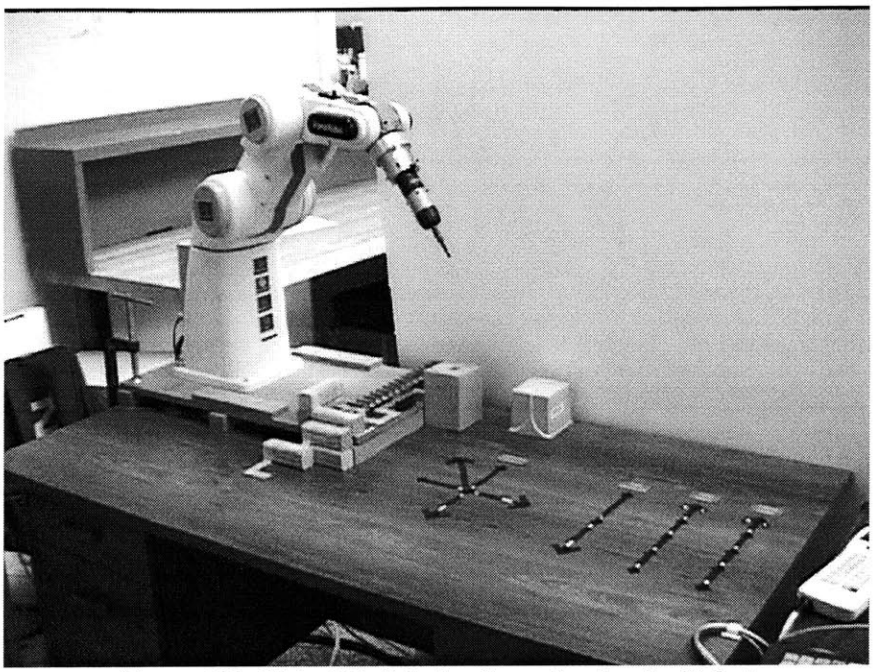

Figure 121: Virtual Switch Configuration for the Robot
A virtual switch panel on the desk is used to control the robot in Cartesian coordinates while virtual switches on the joints are used to control each joint.

Figure 121 shows an obvious configuration for the virtual switch panel for the KS-V20 robot. Virtual switches are located on each joint in order to perform joint moves, intuitively connecting each switch with its resulting actuation. The human is equipped with two touch force sensors on the index and middle fingers. The index finger causes counter-clockwise rotations while the middle finger causes clockwise rotations. Virtual switches for linear Cartesian control are located on the surface of the workspace in the shape of a set of coordinate axes, corresponding to the coordinate frame of the robot. The operator can use two switches for each axis, or one switch for each axis with separate fingers for positive and negative directions.

An experiment was set up in which a human operator is required to move the tip of the robot tool along a path in 3-dimensional Cartesian space. Figure 122 shows a drawing of the experimental setup. The operator is asked to maintain a constant gap of approximately 5-7 mm between the tip of the tool and the path surface. The total path length is 1.42 m. The path is comprised of 27 distinct moves: 11 in the x-direction, 9 in the y-direction, and 7 in the z-direction. The operator must therefore make at least 27 decisions in order to choose the correct switches, either on the teaching pendant or on the virtual switch panel. The robot is programmed

to run at a linear speed of 25 mm/s for both cases. The time it takes the operator to complete the course will be used as a measure of human performance for each method of control.

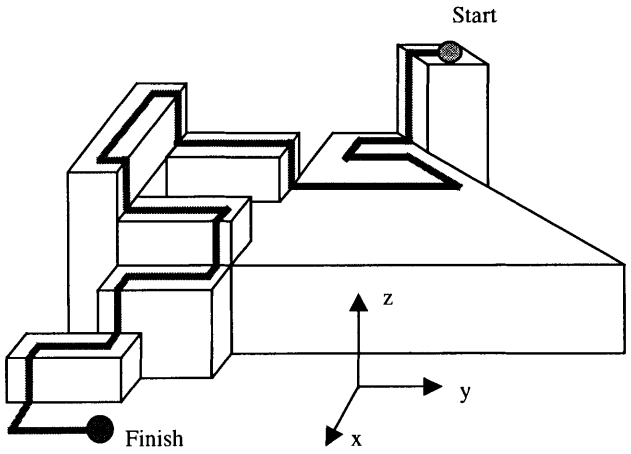

Figure 122: Tool Course
The operator must navigate the robot along this trajectory as quickly as possible.

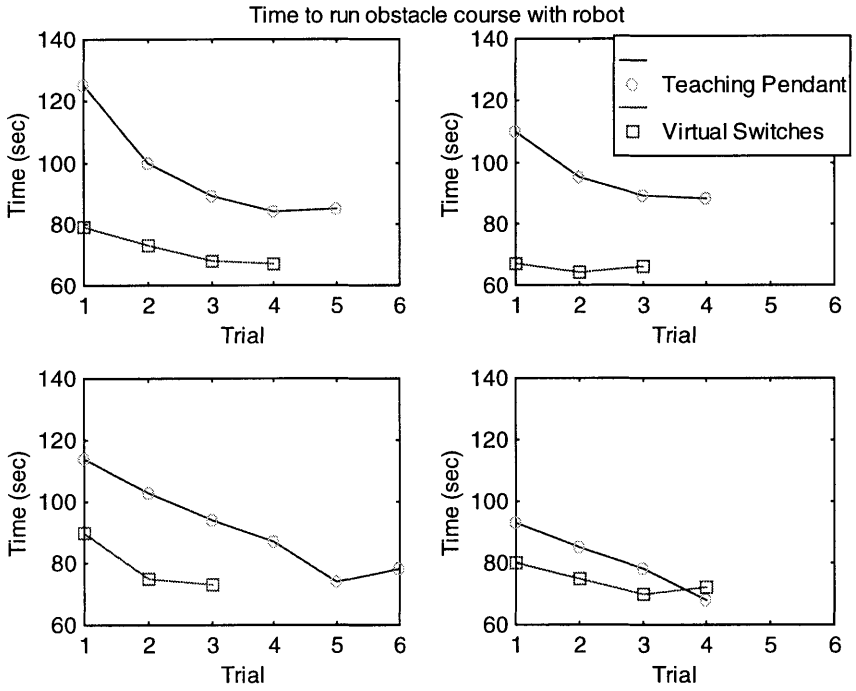

Figure 123: Performance Data for Teaching Pendant and Virtual Switches
Data for four different operators is shown comparing performance using teaching pendant and virtual switches. The operators learn quicker and often perform faster in the long run with virtual switches.

Figure 123 shows the results of this experiment for four human operators. As one might expect, there is certain variation between the operators. However, the learning curve trends are

quite consistent. Compared to using the teaching pendant, the learning curve is noticeably faster when using the virtual switches. The operators converge more quickly on their peak performance when using the virtual switches. This suggests that the virtual switches are a better match for the learning pattern of a human. Also, for some of the operators, the steady-state performance is better when using the virtual switches as compared to the teaching pendant. This suggests non-intuitiveness cannot always be overcome by repetitive experience. The intuition of virtual switches allows some people to operate at a consistently higher performance level in such tasks.

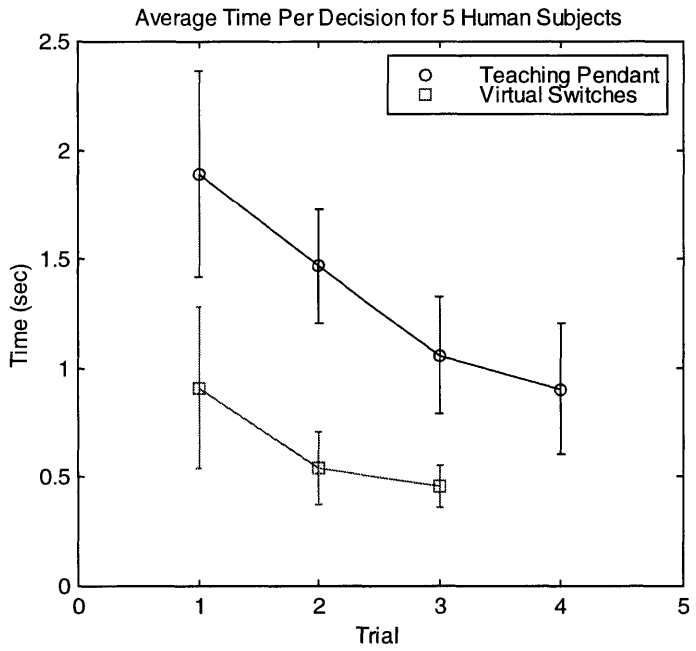

Figure 124: Average Time per Decision for Teaching Pendant and Virtual Switches
On average, subjects are quicker and learn faster with virtual switches.

Based on the speed of the robot, the minimum time to cover the distance of the course is 57 seconds. By subtracting this minimum time required for moving, we can get the approximate time taken up by mental decision making for each operator. Dividing by the total number of decisions required, we get the approximate average time per decision for the operators. The results are averaged for five operators and shown in Figure 124 with standard deviation. The difference here is quite pronounced. The virtual switch seems to offer an initial advantage of taking less than half the time per decision compared to the teaching pendant. At most, about half the number of trials is required for the learning curve to level off. To make any general comparisons about the final steady-state performance, this experiment needs to be conducted with a larger number of trials on a larger pool of human operators.

REFERENCES

Asada, H., Chang, K.-W., and Mascaro, S., 2001. "Finger Touch Sensors and Virtual Switch Panels," US Patent 6,236,037.

Baran, R. and Dawber, R.P.R., eds., 1994. *Diseases of the Nails and their Management.* Oxford: Blackwell Scientific, 2nd edition.

Beaven, D.W. and Brooks, S.E., 1994. *Color Atlas of the Nail in Clinical Diagnosis.* London: Mosby-Wolfe, 2nd edition.

Beebe, D., Denton, D., Radwin, R., and Webster, J., 1998. "A Silicon-Based Tactile Sensor for Finger-Mounted Applications," *IEEE Transactions on Biomedical Engineering*, vol. 45, no. 2, pp. 151-159.

Bollinger, A., Butti, P., Barras, J.-P., Trachsler, H., and Siegenthaler, W., 1974. "Red Blood Cell Velocity in Nailfold Capillaries of Man Measured by a Television Microscopy Technique," *Microvascular Research*, vol. 7, pp. 61-72.

Brooks, M., 1989. "The DataGlove as a Man-Machine Interface for Robotics," *2nd IARP Workshop on Medical and Healthcare Robotics*, pp. 213-225.

Burdea, G. et al., 1992. "A Portable Dextrous Master with Force Feedback," *Presence*, vol. 1, no. 1, pp. 18-28.

Burdea, G.C., 1996. *Force and Touch Feedback for Virtual Reality.* Wiley.

Buss, M. and Hashimoto, H., 1994. "Hand Manipulation Skill Modeling for the Intelligent Cooperative Manipulation System—ICMS," *Proceedings of the IEEE/RSJ/GI International Conference on Intelligent Robots and Systems*, pp. 1234-1241.

Castro, M. and Cliquet, A., Jr., 1997. "A Low-Cost Instrumented Glove for Monitoring Forces During Object Manipulation," *IEEE Transactions on Rehabilitation Engineering*, vol. 5, no. 2, pp. 140-147.

Charm, S.E., and Kurland, G.S., 1974. *Blood Flow and Microcirculation.* NY: Wiley & Sons.

Coffman, J.D. and Cohen, A.S., 1971. "Total and Capillary Fingertip Blood Flow in Raynaud's Phenomenon," *The New England Journal of Medicine*, vol. 285, no. 5, pp. 259-263.

Dawber, R.P.R., De Berker, D., and Baran, R., 1994. "Science of the Nail Apparatus," *Diseases of the Nails and their Management*, Baran, R. and Dawber, R.P.R, eds. Oxford: Blackwell Scientific, 2nd edition.

Debousset, J.F., 1981. "The Digital Joints," *The Hand*, Tubiana, R.T., ed. Philadelphia: W.B. Saunders, vol. 1, pp. 191-201.

DeFanti, T.A. and Sandin, D.J., 1977. "Final Report to the National Endowment of the Arts," US NEA R60-34-163, University of Illinois at Chicago Circle.

Demuth, H. and Beale, M., 1994. *Matlab Neural Network Toolbox User's Guide.* Natick, MA: The Math Works, version 2.

Ducharme, R., Phiroze, K., and Dowden, J., 1991. "A Mathmatical Model of the Flow of Blood Cells in Fine Capillaries," *Journal of Biomechanics*, vol. 24, no. 5, pp. 299-306.

Fels, S. and Hinton, G., 1995. "Glove-TalkII: An Adaptive Gesture-to-Formant Interface," *CHI'95 Conference on Human Factors in Computing Systems*, pp. 456-463.

Fleckman, P. and Allan, C., 2001. "Surgical Anatomy of the Nail Unit," *Dermatologic Surgery*, vol. 27, no. 3, pp. 257-260.

Fleckman, P., 1997. "Basic Science of the Nail Unit," *Nails: Therapy-Diagnosis-Surgery*, Scher, R.K. and Daniel, C.R. III, eds. Philadelphia: W.B. Saunders, 2nd edition, pp. 37-54.

Flint, M.H., 1956. "Some Observations on the Vascular Supply of the Nail Bed and Terminal Segments of the Finger," *British Journal of Hand Surgery*, vol. 8, pp. 186-195.

Foucher, G., ed., 1991. *Fingertip and Nailbed Injuries*. Edinburgh: Churchill Livingstone.

Fung, Y.C., 1993. *Biomechanics: Mechanical Properties of Living Tissues*. New York: Springer-Verlag, 2nd edition.

Ginsburg, C.M. and Maxwell, D., 1983. "Graphical Marionette," *Proceedings of the ACM Siggraph/Sigart Workshop on Motion*, pp. 172-179.

Glicenstein, J. and Dardour, J.C., 1981. "The Pulp: Anatomy and Physiology," *The Hand*, Tubiana, R.T., ed. Philadelphia: W.B. Saunders, vol. 1, pp. 116-120.

Gonzalez-Serva, A., 1997. "Structure and Function," *Nails: Therapy-Diagnosis-Surgery*, Scher, R.K. and Daniel, C.R. III, eds. Philadelphia: Saunders, 2nd edition, pp. 12-31.

Goratowski, R., Langrana, N., and Burdea, G., 1995. "An Innovative Method to Measure Finger Forces, *ASME Bioengineering Conference*, BED-vol. 29, pp. 427-428.

Gray, H., 1995. *Gray's Anatomy: Descriptive and Surgical*. New York: Barnes and Noble, 15th edition, Pick, T.P. and Howden, R., eds.

Gulati, R.J., and Srinivasan, M.A., 1995. "Human Fingerpad under Indentation I: Static and Dynamic Force Response," *ASME Bioengineering Conference*, BED-vol. 29, pp. 261-262.

Guyton, A.C., 1981. *Textbook of Medical Physiology*. Philadelphia: W.B. Saunders.

Han, H.-Y., Shimada, A., and Kawamura, S., 1996. "Analysis of Friction on Human Fingers and Design of Artificial Fingers," *Proceedings of the IEEE International Conference on Robotics and Automation*, pp. 3061-3066.

Haykin, S.S., 1999. *Neural Networks: A Comprehensive Foundation*. Upper Saddle River, NJ: Prentice Hall.

Higgins, J.L. and Fronek, A., 1986. "Photoplethysmographic Evaluation of the Relationship between Skin Reflectance and Skin Blood Volume," *Journal of Biomedical Engineering*, vol. 8, pp. 130-136.

Holmes, M.H., 1986. "Finite Deformation of Soft Tissue: Analysis of a Mixture Model in Uni-Axial Compression," *Journal of Biomechanical Engineering*, vol. 108, pp. 372-381.

Hong, J. and Tan, X., 1989. "Calibrating a DataGlove for Teleoperating the Utah-MIT Hand," *IEEE International Conference on Robotics and Automation*, pp. 1752-1757.

Howe, R.D. and Cutkosky, M.R., 1989. "Sensing Skin Acceleration for Slip and Texture Perception," *IEEE International Conference on Robotics and Automation*, pp. 145-150.

Howe, R.D. and Cutkosky, M.R., 1993. "Dynamic Tactile Sensing: Perception of Fine Surface Features with Stress Rate Sensing," *IEEE Transactions on Robotics and Automation*, vol. 9, no. 2, pp. 140-151.

Jensen, T., Radwin, R., and Webster, J., 1991. "A Conductive Polymer Sensor for Measuring External Finger Forces," *Journal of Biomechanics*, vol. 24, no. 9, pp. 851-858.

Johnson, R.A. and Wichern, D.W., 1988. *Applied Multivariate Statistical Analysis*. Englewood Cliffs, NJ: Prentice Hall, 2nd edition.

Jones, L., 1998. "Perception and Control of Finger Forces," *Proceedings of the ASME Dynamic Systems and Control Division*, vol. 64, pp. 133-137.

Kaestle, S. and Guenther, M., 1998. "Sensor for Performing Medical Measurements, Particularly Pulsoximetry Measurements on the Human Finger," US Patent 5,776,059.

Kalawsky, R.S., 1993. *The Science of Virtual Reality and Virtual Environments*. Addison-Wesley.

Kang, S.B. and Ikeuchi, K., 1994. "Grasp Recognition and Manipulative Motion Characterization from Human Hand Motion Sequences," *Proceedings of the IEEE International Conference on Robotics and Automation*, vol. 2, pp. 1759-1764.

Kao, I., 1994. "Stiffness Control and Calibration of Robotic and Human Hands and Fingers," *Proceedings of the IEEE International Conference on Robotics and Automation*, pp. 399-406.

Karnopp, D.C., Margolis, D.L., and Rosenberg, R.C., 2000. *System Dynamics: Modeling and Simulation of Mechatronic Systems*. New York: John Wiley & Sons, 3rd edition.

Kenaley, G.L. and Cutkosky, M.R., 1989. "Electrorheological Fluid-Based Robotic Fingers with Tactile Sensing," *Proceedings of the IEEE International Conference on Robotics and Automation*, pp. 132-136.

Kim, I. and Inooka, H., 1994. "Determination of Grasp Forces for Robot Hands Based on Human Capabilities," *Control Engineering Practice*, vol. 2, no. 3, pp. 415-420.

Kramer, J. and Leifer, L., 1989. "The Talking Glove: An Expressive and Receptive 'Verbal' Communication Aid for the Deaf, Deaf-Blind, and Non-vocal," tech report, Stanford University, Dept. of Electrical Engineering.

Krstic, R.V., 1991. *Human Microscopic Anatomy: an Atlas for Students of Medicine and Biology*. New York: Springer-Verlag.

Liu, R., Wang, L., and Beebe, D., 1998. "Progress Towards a Smart Skin: Fabrication and Preliminary Testing," *Proceedings of the 20th Annual International Conference of the IEEE Engineering in Medicine and Biology Society*, vol. 20, no. 4, pp. 1841-1844.

Long, C. II, 1981. "Electromyographic Studies of Hand Function," *The Hand*, Tubiana, R.T., ed. Philadelphia: W.B. Saunders, vol. 1, pp. 427-440.

Maeno, T. and Kazumi, K., 1998. "FE Analysis of the Dynamic Characteristics of the Human Finger Pad in Contact with Objects with/without Surface Roughness," *Proceedings of the ASME Dynamic Systems and Control Division*, vol. 64, pp. 279-286.

Malek, R., 1981. "The Grip and its Modalities," *The Hand*, Tubiana, R.T., ed. Philadelphia: W.B. Saunders, vol. 1, pp. 469-476.

Maricq, H.R., 1963. "Capillary Pattern in Familial Schizophrenics: A Study of Nailfold Capillaries," *Circulation*, vol. 27, pp. 406-413.

Mascaro, S. and Asada, H., 1999. "Virtual Switch Human-Machine Interface Using Fingernail Touch Sensors," *Proceedings of the IEEE International Conference on Robotics and Automation*, vol. 4, pp. 2533-2538.

Mascaro, S. and Asada, H., 1998. "Hand-in-Glove Human-Machine Interface and Interactive Control: Task Process Modeling Using Petri Nets," *Proceedings of the IEEE International Conference on Robotics and Automation*, vol. 2, pp. 1289-1295.

McCarragher, B., 1994. "Force Sensing from Human Demonstration Using a Hybrid Dynamical Model and Qualitative Reasoning," *Proceedings of the IEEE International Conference on Robotics and Automation*, vol. 1, pp. 557-563, 1994.

Mendelson, Y. and Ochs, B.D., 1988. "Noninvasive Pulse Oximetry Utilizing Skin Reflectance Photoplethysmography," *IEEE Transactions on Biomedical Engineering*, vol. 35, no. 10, pp. 798-805.

Montagna, W. and Fellis, R., 1961. *Advances in the Biology of Skin*. Elmsford, N.Y.: Pergamon Press.

Moschelle, S.L. and Hurley, H.J., 1985. *Dermatology*. Philadelphia: W.B. Saunders, vol. 1, 2nd edition.

Nagata, K., Oosaki, Y., Kakikura, M., and Tsukune, H., 1998. "Delivery by Hand between Human and Robot Based on Fingertip Force-Torque Information," *Proceedings of the IEEE/RSJ International Conference on Intelligent Robots and Systems*, pp. 750-757.

Nakamura, Y., 1991. *Advanced Robotics: Redundancy and Optimization*. Reading, MA: Addison-Wesley.

Nakazawa, N., Uekita, Y., Inooka, H., and Ikeuri, R., 1996. "Experimental Study on Human's Grasping Force," *Proceedings of the IEEE International Workshop on Robot and Human Communication*, pp. 280-285.

Nelson, T.J., Van Dover, R.B., Jin, S., Hackwood, S., and Beni, G., 1986. "Shear-Sensitive Magnetoresistive Robotic Tactile Sensor," *IEEE Transactions on Magnetics*, vol. 22, no. 5, pp. 394-396.

Nicolelis, M.A.L., Ghazanfar, A.A., Stambaugh, C.H., Oliveira, L.M.O., Laubach, M., Chapin, J.K., Nelson, R., and Kaas, J.H., 1998. "Simultaneous Encoding of Tactile Information by Three Primate Cortical Areas," *Nature Neuroscience*, vol. 1, pp. 621-630.

Nitzan, M., Babchenko, A., Khanokh, B., and Taitelbaum, H., 2000. "Measurement of Oxygen Saturation in Venous Blood by Dynamic Near Infrared Spectroscopy," *Journal of Biomedical Optics*, vol. 5, no. 2, pp. 155-162.

Novak, J.L., 1989. "Initial Design and Analysis of a Capacitive Sensor for Shear and Normal Force Measurement," *Proceedings of the IEEE International Conference on Robotics and Automation*, vol. 1, pp.137-144.

Ogata, K., 1990. *Modern Control Engineering*. Englewood Cliffs, NJ: Prentice Hall, 2nd edition.

Pallardy, G., Chevrot, A., Galmiche, J.M., and Galmiche, B., 1981. "Radiological Examination of the Hand and Wrist," *The Hand*, Tubiana, R.T., ed. Philadelphia: W.B. Saunders, vol. 1, pp. 648-684.

Pao, L. and Speeter, T.H., 1989. "Transformation of Human Hand Positions for Robotic Hand Control," *Proceedings of the IEEE International Conference on Robotics and Automation*, vol. 3, pp. 1758-1763.

Pawluk, D.T.V. and Howe, R.D., 1999. "Dynamic Lumped Element Response of the Human Fingerpad," *Journal of Biomechanical Engineering,* vol. 121, no. 2, pp. 178-183.

Pawluk, D.T.V. and Howe, R.D., 1999. "Dynamic Contact of the Human Fingerpad Against a Flat Surface," *Journal of Biomechanical Engineering*, vol. 121, no. 6, pp. 605-611.

Pawluk, D.T.V. and Howe, R.D., 1997. "Mechanical Impedance and Energy Dissipation in the Human Fingerpad," *ASME Bioengineering Conference*, BED-vol. 35, pp. 591-592.

Peine, W.J. and Howe, R.D., 1997. "Finger Pad Shape in Lump Detection," *ASME Bioengineering Conference*, BED-vol. 35, pp. 593-594.

Rabischong, P., 1981. "Physiology of Sensation," *The Hand*, Tubiana, R.T., ed. Philadelphia: W.B. Saunders, vol. 1, pp. 441-467.

Raju, B.I., 1998. *Encoding and decoding of shape in tactile sensing*, S.M. Thesis. Cambridge, MA: Massachusetts Institute of Technology.

Rawlings, J.O., 1988. *Applied Regression Analysis: A Research Tool.* Pacific Grove, CA: Wadsworth & Brooks/Cole.

Rempel, D., Dennerlein, J., Mote, C.D. Jr., and Armstrong, T., 1994. "A Method of Measuring Fingertip Loading During Keyboard Use," *Journal of Biomechanics*, vol. 27, no. 8, pp. 1101-1104.

Richardson, D., 1982. "Relationship Between Digital Artery and Nailfold Capillary Flow Velocities in Human Skin," *Microcirculation*, vol. 2, no. 3, pp. 283-296.

Rohling, R.N., Hollerbach, J.M., and Jacobsen, S.C., 1993. "Optimized Fingertip Mapping: A General Algorithm for Robotic Hand Teleoperation," *Presence*, vol. 2, no. 3, pp. 203-220.

Rohling, R.N. and Hollerbach, J.M., 1993. "Calibrating the Human Hand for Haptic Interfaces," *Presence*, vol. 2, no. 4, pp. 281-296.

Sato, S., Shimojo, M., Seki, Y., Takahashi, A., and Shimuzu, S., 1996. "Measuring System for Grasping," *Proceedings of the IEEE International Workshop on Robot and Human Communication*, pp. 292-297.

Scher, R.K. and Daniel, C.R. III, eds., 1997. *Nails: Therapy-Diagnosis-Surgery.* Philadelphia: W.B. Saunders, 2nd edition.

Serina, E.R., Mockensturm, E., Mote, C.D. Jr., and Rempel, D., 1998. "A Structural Model of the Forced Compression of the Fingertip Pulp," *Journal of Biomechanics*, vol. 31, no. 7, pp. 639-646.

Serina, E.R., Mote, C.D. Jr., and Rempel, D., 1997. "Force Response of the Fingertip Pulp to Repeated Compression—Effects of Loading Rate, Loading Angle, and Anthropometry," *Journal of Biomechanics*, vol. 30, no. 10, pp. 1035-1040.

Serina, E.R., Mote, C.D. Jr., and Rempel, D.M., 1995. "Mechanical Properties of the Fingertip Pulp under Repeated, Dynamic, Compressive Loading," *ASME Advances in Bioengineering Conference*, BED-vol. 31, pp. 245-246.

Sheridan, T.B., 1992. *Telerobotics, Automation, and Human Supervisory Control.* Cambridge, MA: MIT Press.

Shimizu, S., Shimojo, M., Sato, S., Seki, Y., Takahashi, A., Inukai, Y., and Yoshioka, M., 1996. "The Relation between Human Grip Types and Force Distribution Pattern in Grasping," *Proceedings of the IEEE Workshop on Robot and Human Communication*, pp. 286-291.

Shitzer, A., Bellomo, S., Stroschein, L.A., Gonazalez, R.R., and Pandolf, K.B., 1998. "Simulation of a Cold-Stressed Finger Including the Effects of Wind, Gloves, and Cold-Induced Vasodilation," *Journal of Biomechanical Engineering*, vol. 120, pp. 389-394.

Simmons, B.P. and De La Caffiniere, J.Y., 1981. "Physiology of Flexion of the Fingers," *The Hand*, Tubiana, R.T., ed. Philadelphia: W.B. Saunders, vol. 1, pp. 377-388.

Singh, U. and Fearing, R.S., 1998. "Tactile After-Images from Static Contact," *Proceedings of the ASME Dynamic Systems and Control Division*, vol. 64, pp. 163-170.

Smith, D.O., Chikayoshi, O., Kimura, C., and Toshimori, K., 1991. "Artery Anatomy and Tortuosity in the Distal Finger," *The Journal of Hand Surgery*, vol. 16A, pp. 297-302.

Smith, D.O., Chikayoshi, O., Kimura, C., and Toshimori, K., 1991. "The Distal Venous Anatomy of the Finger," *The Journal of Hand Surgery*, vol. 16A, pp. 303-307.

Speeter, T.H., 1992. "Transforming Human Hand Motion for Telemanipulation," *Presence*, vol. 1, no. 1, pp. 63-79.

Spence, A.P., 1982. *Basic Human Anatomy.* Menlo Park, CA: Benjamin/Cummings.

Srinivasan, M.A., 1989. "Surface Deflection of Primate Fingertip Under Line Load," *Journal of Biomechanics*, vol. 22, no. 4, pp. 343-349.

Steinke, J.M. and Shepherd, A.P., 1986. "Role of Light Scattering in Whole Blood Oximetry," *IEEE Transactions on Biomedical Engineering*, vol. 33, no. 3, pp. 294-301.

Sturman, D.J. and Zeltzer, D., 1994. "A Survey of Glove-Based Input," *IEEE Computer Graphics and Applications*, vol. 14, no. 1, pp. 30-39.

Takatani, S., and Graham, M.D., 1979. "Theoretical Analysis of Diffuse Reflectance from a Two-Layer Tissue Model," *IEEE Transactions on Biomedical Engineering*, vol. 26, no. 12, pp. 656-664.

Thomine, J.-M., 1981. "The Skin of the Hand," *The Hand*, Tubiana, R.T., ed. Philadelphia: W.B. Saunders, vol. 1, pp. 107-115.

Topping, A., Kuperschmidt, V., Gormley, A., 1998. "Method and Apparatus for the Automated Identification of Individuals by the Nail Beds of their Fingernails," US Patent 5,751,835.

Tremper, K.K. and Barker, S.J., 1989. "Pulse Oximetery," *Anesthesiology*, vol. 70, no. 1, pp. 98-108.

Tubiana, R.T., ed., 1981. *The Hand.* Philadelphia: W.B. Saunders, vol. 1.

Tubiana, R.T., 1981. "Architecture and Functions of the Hand," *The Hand*, Tubiana, R.T., ed. Philadelphia: W.B. Saunders, vol. 1, pp. 19-93.

Tung, C.P. and Kak, A.C., 1995. "Automatic Learning of Assembly Tasks using a DataGlove System," *IEEE/RSJ Int. Conference on Intelligent Robots and Systems*, vol. 1, pp. 1-8.

Valentin, P., 1981. "Physiology of Extension of the Fingers," *The Hand*, Tubiana, R.T., ed. Philadelphia: W.B. Saunders, vol. 1, pp. 389-398.

Van Gemert, M.J.C., Jacques, S.L., Sterenborg, H.J.C.M., and Star, W.M., 1989. "Skin Optics," *IEEE Transactions on Biomedical Engineering*, vol. 36, no. 12, pp. 1146-1161.

Voyles, R.M. and Khosla, P.K., 1995. "Tactile Gestures for Human/Robot Interaction," *IEEE/RSJ International Conference on Intelligent Robots and Systems*, vol. 3, pp. 7-13.

Webster, J., ed., 1988. *Tactile Sensors for Robotics and Medicine.* New York: Wiley.

Welch, DeCesare, and Hess, 1990. "Pulse Oximetry: Instrumentation and Clinical Applications," *Respiratory Care*, vol. 35, no. 6, pp. 588.

Wolfram-Gabel, R. and Sick, H., 1995. "Vascular Networks of the Periphery of the Fingernail," *The Journal of Hand Surgery*, vol. 20B, no. 4, pp. 488-492.

Wessberg, J., Stambaugh, C.R., Kralik , J.D., Beck, P.D., Chapin, J.K., Kim, J., Biggs, S.J., Srinivasan, M.A., and Nicolelis, M.A.L., 2000. "Real-Time Prediction of Hand Trajectory by Ensembles of Cortical Neurons in Primates," *Nature*, vol. 408, pp. 361-365.

Westling, G., and Johansson, R.S., 1987. "Responses in Glabrous Skin Mechanoreceptors During Precision Grip in Humans," *Experimental Brain Research*, vol. 66, pp. 128-140.

Yamada, Y. and Cutkosky, M.R., 1994. "Tactile Sensor with 3-Axis Force and Vibration Sensing Functions and its Application to Detect Rotational Slip," *Proceedings of the IEEE International Conference on Robotics and Automation*, pp. 3550-3557.

Yun, H., Cannon, D., Freivalds, A., and Thomas, G., 1997. "An Instrumented Glove for Grasp Specification in Virtual-Reality-Based Point-and-Direct Telerobotics," *IEEE Transactions on Systems, Man, and Cybernetics*, Part B, vol. 27, no. 5, pp. 835-846.

Zee, F., Holweg, E.G.M., Jongkind, W., and Honderd, G., 1997. "Shear Force Measurement using a Rubber Based Tactile Matrix Sensor," *Proceedings of the IEEE International Conference on Advanced Robotics*, pp. 733-738.

Zimmerman, T.G., et al., 1987. "A Hand Gesture Interface Device," *Proceedings of Human Factors in Computer Systems and Graphic Interface*, pp. 189-192.

Zook, E.G., Van Beek, A.L., Russell, R.C., and Beatty, M.E., 1980. "Anatomy and Physiology of the Perionychium: A Review of the Literature and Anatomic Study," *The Journal of Hand Surgery*, vol. 5, no. 6, pp. 528-536.